Luís Gonçalo Lourenço Sorger

Licenciatura em Ciências da Engenharia

Characterization of processed materials by electrical currents: development of equipment and applications

Dissertação para obtenção do Grau de Mestre em
Engenharia Mecânica

Orientadora : Doutora Rosa Maria Mendes Miranda, Profª. Associada com Agregação, Universidade Nova de Lisboa

Co-orientador : Doutor Telmo Jorge Gomes dos Santos, Prof. Auxiliar, Universidade Nova de Lisboa

Júri:

Presidente: Prof. Doutor Jorge Joaquim Pamies Teixeira

Arguente: Profª. Doutora Maria Luísa Coutinho Gomes de Almeida

Vogal: Profª. Doutora Rosa Maria Mendes Miranda

FACULDADE DE CIÊNCIAS E TECNOLOGIA
UNIVERSIDADE NOVA DE LISBOA

Março, 2014

Characterization of processed materials by electrical currents: development of equipment and applications

Copyright © Luís Gonçalo Lourenço Sorger, Faculdade de Ciências e Tecnologia, Universidade Nova de Lisboa

A Faculdade de Ciências e Tecnologia e a Universidade Nova de Lisboa têm o direito, perpétuo e sem limites geográficos, de arquivar e publicar esta dissertação através de exemplares impressos reproduzidos em papel ou de forma digital, ou por qualquer outro meio conhecido ou que venha a ser inventado, e de a divulgar através de repositórios científicos e de admitir a sua cópia e distribuição com objectivos educacionais ou de investigação, não comerciais, desde que seja dado crédito ao autor e editor.

Acknowledgements

This work would not have been possible without the contribution and support of many people. My deepest thanks go to my adviser, Professor Rosa Miranda, for offering me the opportunity to work in such a stimulating and challenging environment and with a group of people from whom I have learned so much. Her guidance, support and encouragement in every step of this work will be forever cherished, along with her friendship.

To my co-adviser, Professor Telmo Santos, whose example I look up to, I thank for the knowledge he shared and for all the help and support he provided. Working alongside him was a privilege that allowed me to learn more than I could ever have expected. His friendship and camaraderie were much appreciated.

To Professor Jorge Pamies Teixeira and Professor Carla Machado, my sincere thanks for their help and advices. Also to Professor Henrique Guedes for the help he provided, but specially for his kind words of encouragement. Thanks to Eng. João Oliveira for is help with the etchants. To Mr. António Campos and Mr. Paulo Magalhães, my sincere thanks for their invaluable help and mostly their good nature and friendship.

I thank the colleagues that accompanied my throughout these years, specially the ones who worked alongside me in the Mechanical Technology laboratory. The help we provided each other has certainly enriched our work and their friendship has enriched my life.

To all my friends who, in one way or another, accompanied throughout this journey a sincere thank you. Particularly to the "*Estafeta de estilos*", for all the laughs and for being the best friends anyone could hope for.

To my mother, whose memory is and will always be an inspiration. To my father for his sacrifices and for always believing in me. To my grandfather José and my grandmother Maria for their unconditional love and support. I am truly blessed for having such a wonderful family that has filled my life with love even in the darkest moments.

To Inês, for having the patience to put up with me and, mostly, for all her love and for being my best friend. Thank you.

Abstract

Structural characterization of welded or processed materials is critical for a correct assessment of their properties. Microstructural analysis by optical microscopy provides information to identify the distinctive zones, their extent and the major transformations induced. For structural analysis, hardness is the simplest property to measure, providing information on the existence of ductile or brittle zones in the material. Furthermore, it can be qualitatively correlated to yield strength. However, these techniques are time consuming and destructive and, therefore, there is need for new, dedicated, preferably non-destructive, characterization methods.

The same changes in properties and structure, due to welding and processing, also alter the electrical conductivity of materials. In fact, studies have demonstrated a relation between microstructure and conductivity of friction stir processed Al alloys, relating decreases in this property to the increase in the barriers to electron mobility due to the refined grain of the dynamically recrystallized zone, while the opposite occurs in heat affected zones were grain growth exists.

The aim of this thesis was to apply eddy currents electrical conductivity characterization techniques to a wider range of materials, and develop equipment for an alternative electrical current evaluation method, namely, four-point probe potential drop measurements. A prototype for an automated four-point probe electrical conductivity characterization equipment was designed, built and successfully tested. Electrical conductivity characterization techniques, by eddy currents, have been applied to different metallic materials (AISI 1020, AISI 304, AZ31, Ti Grade 5, Ti Grade 2, Lead and Copper) processed by solid-state (Friction Stir Processing (FSP)) and fusion (Metal Active Gas (MAG) and Tungsten Inhert Gas (TIG)) to evaluate the effects on their electrical conductivity profiles and compare them with the hardness profiles and the microstructural features.

Results show that the electrical conductivity variations that occur due to welding and processing can be related to the hardness and the microstructure of materials and, depending on the material, this relation can be direct or inverse.

Keywords: materials characterization; electrical conductivity, eddy currents, four-point probe.

Resumo

A caracterização estrutural de materiais processados é crucial para uma correcta avaliação das suas propriedades. Análise por microscopia óptica permite a identificação das zonas distintas, a sua extensão e as transformações mais significativas. Para a análise estrutural, a dureza é a propriedade mais simples de medir, fornecendo informação acerca da existencia de zonas dúcteis ou frágeis no material. Adicionalmente, pode ser qualitativamente relacionada com a tensão de cedência. No entanto, estas técnicas são morosas e destrutivas e, portanto, existe uma necessidade de novos métodos de caracterização, dedicados, de preferência, não-destrutivos.

As mesmas alterações nas propriedades e microstrutura, devidas à soldadura e processamento, também afectam a condutividade eléctrica dos materiais. De facto, estudos demonstraram a existência de uma relação entre a microstrutura e condutividade em ligas de alumínio processadas por fricção linear, relacionando diminuições desta propriedade com um aumento das barreiras à mobilidade electrónica devido ao refinamento de grão na zona dinâmicamente recristalizda, ocorrendo o oposto nas zonas térmicamente afectadas onde existe crescimento do grão.

O objectivo desta tese foi a aplicação de técnicas de caracterização por correntes induzidas a uma vasta gama de materiais e o desenvolvimento de equipamento de inspecção baseado numa técnica alternativa por correntes eléctricas, nomeadamente, ensaios de queda de potêncial por sonda de quatro pontos. Um protótipo de equipamento automatizado para caracterização deconductividade eléctrica por sonda de quatro pontos foi profectado, construido e testado com sucesso. Técnicas de caracterização de condutividade, por correntes induzidas, foram aplicadas a diferentes materiais metálicos (AISI 1020, AISI 304, AZ31, Ti Grau 5, Ti Grau 2, Chumbo e Cobre) processados no estado sólido (Soldadura por Fricção Linear (SFL)) e por fusão (soldadura Tungsten Inhert Gas (TIG) e Metal Active Gas (MAG)) para avaliar os efeitos nos seus perfis de condutividade electrica e comparar com os perfis de dureza e as caracteristicas microstruturais.

Os resultados indicam que as variações de condutividade eléctrica que ocorrem devido à soldadura e processamento podem ser relacionadas com a dureza e a microstrutura dos materiais e, dependendo do material, essa relação pode ser directa ou inversa.

Palavras-chave: caracterização de materiais; condutividade eléctrica; correntes induzidas; sonda de quatro pontos.

Contents

1 Introduction **1**

1.1 Motivation . . . 2

1.2 Objectives . . . 3

1.3 Document structure . . . 3

2 State-of-the-art **5**

2.1 Materials Processing . . . 6

2.1.1 Solid-state processes . . . 6

Friction Stir welding and processing . . . 6

2.1.2 Fusion processes . . . 14

TIG and MAG welding . . . 15

2.2 Effects of processing on electrical conductivity . . . 16

2.2.1 Microstructure and electrical conductivity . . . 17

2.3 Evaluation of electrical conductivity variations . . . 19

2.3.1 Eddy currents testing . . . 21

Fundamentals . . . 21

2.3.2 4-point probe potential drop testing . . . 23

Fundamentals . . . 23

2.4 Conclusions . . . 25

3 Development of laboratory means **27**

3.1 Functional Requirements . . . 28

3.2 Prototype development . . . 30

3.3 System validation trials . . . 36

3.4 Conclusions . . . 38

4 Experimental procedure **39**

4.1 Materials . . . 40

4.2 Welding and processing . . . 41

4.2.1 Friction Stir Processing 42
4.2.2 MAG Welding 43
4.2.3 TIG Welding 44
4.3 Characterization techniques 45
4.3.1 Electrical conductivity measurements 45
4.3.2 Metallographical examination and micro-hardness measurements 47
4.4 Conclusions 47

5 Results and Discussion **49**
5.1 Introduction 50
5.2 AISI 1020 51
5.3 AISI 304 57
5.4 Titanium Grade 5 62
5.5 Titanium Grade 2 67
5.6 AZ31 Magnesium Alloy 69
5.7 Lead 75
5.8 Copper 79
5.9 Conclusions 82

6 Final conclusions **85**
6.1 Future work suggestions 87

List of Figures

2.1 Schematic representation of Friction Stir Processing. 6
2.2 Macrograph showing the different zones occurring in FSP materials. . . . 7
2.3 Tensile test results of base metal and multi-pass FSP samples for different directions. 8
2.4 Crack length vs. number of cycles, cast + T6 vs. FSP + T6. 8
2.5 Specimens of two FSP 7075Al alloys, with different grain sizes, tested at 500 and 480 °C at various strain rates. 9
2.6 Ligth micrograph of AZ31 before and after FSP 9
2.7 Appearance of AZ91 BM and FSP specimens after tensile test at elevated strain rate with a temperature of 573 K. 10
2.8 SFSP being performed. 10
2.9 Schematic drawing of the FSP with rapid heat sink apparatus conceived by Chang *et al.*. 11
2.10 Grain size distribution chart and Microhardness profile for Friction Stir Processing (FSP) AZ31 alloy. 11
2.11 Microhardness profile and appearence of tensile specimen for FSW commercially pure copper under various welding conditions. 12
2.12 Hardness profiles in cross-sections of the FSW Cu joints at various parameters and variation of yield strenght of FSW Cu joints with the lowest hardness values of HAZ 13
2.13 Relationship between precipitate distribution and hardness profile. 13
2.14 Evolution of the hardness, across the retreating side of a FSW 2024 T351, with the volume fraction of precipitates. 14
2.15 Microhardness profile of AMX602 Mg alloys joints. 14
2.16 Microstructure of welded joints. Comparison of TIG and FSW 16
2.17 Transversal macrograph, electrical conductivity and Vickers hardness profiles of hot FSW bead on plate on AA 7075-T6 10 mm thick plate. 20
2.18 Eddy Currents 22

2.19 Two-point and four-point resistivity measurement methods 24
2.20 Representation of a typical four-point probe. 24

3.1 Four-point probe. 30
3.2 Prototype design details. 32
3.3 XYZ table prototype. 33
3.4 XYZ table GUI. 33
3.5 Schematics of the different inspection modes. 34
3.6 Variation of conductivity with potential drop and current, according to equation 2.9. 35
3.7 Variation of potential drop with conductivity for a probe with $d = 1$ mm and a current of $I = 0.05$ mA. 35
3.8 Variation of potential drop with conductivity, between 0 and 140 %IACS for a probe with $d = 1$ mm and a current of $I = 0.05$ mA. 36
3.9 Setup of the equipment validation trials. 36
3.10 Screenshot of the inspection of the PIM material, sample 4. 37
3.11 Four-point probe electrical conductivity measurements on samples 1, 2 and 4 of a PIM material. 37
3.12 Eddy current inspection sample 4 of a PIM material sample for validation of four-point probe trials. 38

4.1 Friction Stir Welding being performed. 42
4.2 Temperature variation during FSP of Ti grade 5. 43
4.3 MAG welding setup 44
4.4 TIG welding setup 44
4.5 Schematic representation of sample marking for the extraction of specimens. 45
4.6 Eddy currents equipment. 46
4.7 Eddy currents calibration. 46
4.8 Setup of equipment used for conductivity testing. 47
4.9 Schematic representation of the depth at which microhardness measurements were performed. 47

5.1 Variation of depth of penetration (δ) with frequency for the materials under study. 50
5.2 Macrograph of the AISI 1020 Sample-A. The dashed lines indicate the depths at which the conductivity measurements were performed (from top to bottom: $Z = 0$ mm; $Z = -1$ mm; $Z = -2$ mm). 51
5.3 Electrical conductivity measurements performed at $Z = 0$ mm on AISI 1020 welded by MAG 52
5.4 Electrical conductivity measurements performed at $Z = -1$ mm on AISI 1020 welded by MAG 52

5.5 Electrical conductivity measurements performed at $Z = -2$ mm on AISI 1020 welded by MAG 52
5.6 Detail of segregation bands present in AISI 1020. 53
5.7 Electrical conductivity profile, performed at $Z = 0$ mm,and sub-surface hardness profile superposed with macrograph of AISI 1020 Sample-A. The hardness and conductivity show a good agreement, with an inverse relation. Welding parameters: Passes = 4; V = 17.6 V; I = 113 V; v = 166 mm/min; H = 0.72 kJ. 53
5.8 Macrograph and micrographs of AISI 1020, Sample-A 54
5.9 Macrograph of the AISI 1020 Sample-B. The dashed lines indicate the depths at which the conductivity measurements were performed (from top to bottom: $Z = 0$ mm; $Z = -1$ mm; $Z = -2$ mm). 54
5.10 Electrical conductivity measurements performed at $Z = 0$ mm on AISI 1020 welded by MAG 55
5.11 Electrical conductivity measurements performed at $Z = -1$ mm on AISI 1020 welded by MAG 55
5.12 Electrical conductivity measurements performed at $Z = -2$ mm on AISI 1020 welded by MAG 55
5.13 Electrical conductivity profile, performed at $Z = 0$ mm,and sub-surface hardness profile superposed with macrograph of AISI 1020 Sample-B. The hardness and conductivity show a good agreement, with an inverse relation. Welding parameters: Passes = 2; V = 19.5 V; I = 135 V; v = 120 mm/min; H = 1.32 kJ. 56
5.14 Macrograph and micrographs of AISI 1020, Sample-B 56
5.15 Macrograph of the 304 SS Sample-D. The dashed lines indicate the depths at which the conductivity measurements were performed (from top to bottom: $Z = 0$ mm; $Z = -1$ mm; $Z = -2$ mm). 57
5.16 Electrical conductivity measurements performed at $Z = 0$ mm on AISI 304, Sample-D, welded by TIG. Welding parameters: V = 15 V; I = 80 V; v = 225 mm/min; H = 0.28 kJ. 57
5.17 Electrical conductivity measurements performed at $Z = -1$ mm on AISI 304, Sample-D, welded by TIG. Welding parameters: V = 15 V; I = 80 V; v = 225 mm/min; H = 0.28 kJ. 58
5.18 Electrical conductivity measurements performed at $Z = -2$ mm on AISI 304, Sample-D, welded by TIG. Welding parameters: V = 15 V; I = 80 V; v = 225 mm/min; H = 0.28 kJ. 58
5.19 Electrical conductivity profile, performed at $Z = 0$ mm,and sub-surface hardness profile superposed with macrograph of AISI 304, Sample-D. The hardness and conductivity profiles display a direct relation. Welding parameters: V = 15 V; I = 80 V; v = 225 mm/min; H = 0.28 kJ. 59

5.20 a) Macrograph of AISI 304, Sample-D. b) Micrograph of the base material with the typical microstructure of an austenitic stainless steel. c) Solidification structure in the fusion zone with the formation of δ-ferrite. d) Some grain growth in the Heat Affected Zone (HAZ). 59
5.21 Macrograph of the 304 SS Sample-D. The dashed lines indicate the depths at which the conductivity measurements were performed (from top to bottom: $Z = 0$ mm; $Z = -1$ mm; $Z = -2$ mm). 59
5.22 Electrical conductivity measurements performed at $Z = 0$ mm on AISI 304, Sample-E, welded by TIG. Welding parameters: V = 15 V; I = 80 V; v = 138 mm/min; H = 0.84 kJ. 60
5.23 Electrical conductivity measurements performed at $Z = -1$ mm on AISI 304, Sample-E, welded by TIG. Welding parameters: V = 15 V; I = 80 V; v = 138 mm/min; H = 0.84 kJ. 60
5.24 Electrical conductivity measurements performed at $Z = -2$ mm on AISI 304, Sample-E, welded by TIG. Welding parameters: V = 15 V; I = 80 V; v = 138 mm/min; H = 0.84 kJ. 60
5.25 Electrical conductivity profile, performed at $Z = 0$ mm,and sub-surface hardness profile superposed with macrograph of AISI 304, Sample-E. The hardness and conductivity profiles display a direct relation. Welding parameters: V = 15 V; I = 80 V; v = 225 mm/min; H = 0.84 kJ. 61
5.26 Electrical conductivity profile, performed at $Z = -1$ mm,and sub-surface hardness profile superposed with macrograph of AISI 304, Sample-E. The hardness and conductivity profiles display a direct relation. Welding parameters: V = 15 V; I = 80 V; v = 225 mm/min; H = 0.84 kJ. 61
5.27 a) Macrograph of AISI 304, Sample-D. b) Micrograph of the base material with the typical microstructure of an austenitic stainless steel. c) Solidification structure in the fusion zone with the formation of δ-ferrite. d) Some grain coalescence in the HAZ. 62
5.28 Macrograph of the FSP Ti Grade 5, Sample-O. The dashed lines indicate the depths at which the conductivity measurements were performed (from top to bottom: $Z = 0$ mm; $Z = -1$ mm; $Z = -2$ mm). 62
5.29 Electrical conductivity measurements performed at $Z = 0$ mm on FSP Ti Grade 5, Sample-O. Processing parameters: $\omega = 1120$ rpm; $v = 71$ mm/min; $\omega/v = 15.8$. 63
5.30 Electrical conductivity measurements performed at $Z = -1$ mm on FSP Ti Grade 5, Sample-O. Processing parameters: $\omega = 1120$ rpm; $v = 71$ mm/min; $\omega/v = 15.8$. 63
5.31 Electrical conductivity measurements performed at $Z = -2$ mm on FSP Ti Grade 5, Sample-O. Processing parameters: $\omega = 1120$ rpm; $v = 71$ mm/min; $\omega/v = 15.8$. 63

5.32 Electrical conductivity and hardness profiles, performed at $Z = 0$ mm, superposed with macrograph of sample FSP Ti Grade 5, Sample-O. 64

5.33 a) Macrograph of FSP Ti Grade 5, Sample-O. b) Micrograph of the base material. c) Processed zone with destruction of the original microstructure of the base material. d) Some grain growth in the HAZ. 64

5.34 Macrograph of the Ti Grade 5 Sample-P. The dashed lines indicate the depths at which the conductivity measurements were performed (from top to bottom: $Z = 0$ mm; $Z = -1$ mm; $Z = -2$ mm). 64

5.35 Electrical conductivity measurements performed at $Z = 0$ mm on Ti Grade 5, Sample-P, welded by TIG. H = 0.32 kJ. 65

5.36 Electrical conductivity measurements performed at $Z = -1$ mm on Ti Grade 5, Sample-P, welded by TIG. H = 0.32 kJ. 65

5.37 Electrical conductivity measurements performed at $Z = -2$ mm on Ti Grade 5, Sample-P, welded by TIG. H = 0.32 kJ. 65

5.38 Electrical conductivity profile, performed at $Z = 0$ mm,and sub-surface hardness profile superposed with macrograph of Ti Grade 5, Sample-P, welded by TIG. The hardness and conductivity profiles display a direct. . 66

5.39 Electrical conductivity profile, performed at $Z = -1$ mm,and sub-surface hardness profile superposed with macrograph of Ti Grade 5, Sample-P, welded by TIG. The hardness and conductivity profiles display a direct. . 66

5.40 a) Macrograph of Ti Grade 5, Sample-P, welded by TIG. b) Micrograph of the base material. c) Microstructure of the fusion zone with an $\alpha + \beta$ solidification structure since cooling was to fast to allow the formation of martensite-like structures. d) Some grain growth and precipitate coalescence in the HAZ. 67

5.41 Macrograph of the TIG welded Ti Grade 2, Sample-R. The dashed lines indicate the depths at which the conductivity measurements were performed (from top to bottom: $Z = 0$ mm; $Z = -1$ mm; $Z = -2$ mm). 67

5.42 Electrical conductivity measurements performed on TIG welded Ti Grade 2, Sample-R at $Z = 0$ mm. 68

5.43 Electrical conductivity measurements performed on TIG welded Ti Grade 2, Sample-R at $Z = -1$ mm. 68

5.44 Electrical conductivity measurements performed on TIG welded Ti Grade 2, Sample-R at $Z = -2$ mm. 68

5.45 Electrical conductivity and hardness profiles, performed at $Z = 0$ mm, superposed with macrograph of sample TIG welded Ti Grade 2, Sample-R. . 69

5.46 a) Macrograph of Ti Grade 2 (Sample-R). b) Detail of the frontier between the base material and the fusion zone. c) Micrograph of the fusion zone. d) Micrograph of the base material. 69

5.47 Macrograph of the AZ31 Sample-J. The dashed lines indicate the depths at which the conductivity measurements were performed (from top to bottom: $Z = 0$ mm; $Z = -1$ mm; $Z = -2$ mm). 70
5.48 Electrical conductivity measurements performed on AZ31, Sample-J, processed in the cold condition at $Z = 0$ mm. 70
5.49 Electrical conductivity measurements performed on AZ31, Sample-J, processed in the cold condition at $Z = -1$ mm. 70
5.50 Electrical conductivity measurements performed on AZ31, Sample-J, processed in the cold condition at $Z = -2$ mm. 70
5.51 Electrical conductivity and hardness profiles, performed at $Z = 0$ mm, superposed with macrograph of the FSP AZ31 processed in the cold condition, Sample-J. 71
5.52 a) Macrograph of AZ31 processed in the cold condition, Sample-J. b) Detail of the difference between the microstructures of the base material and the stirred zone. c) Fine-grained stirred zone. d) Base material with a typical solidification structure of a cast AZ31. 71
5.53 Macrograph of the AZ31 processed in the hot condition Sample-K. The dashed lines indicate the depths at which the conductivity measurements were performed (from top to bottom: $Z = 0$ mm; $Z = -1$ mm; $Z = -2$ mm). 72
5.54 Electrical conductivity measurements performed on AZ31, Sample-K, processed in the hot condition at $Z = 0$ mm. 72
5.55 Electrical conductivity measurements performed on AZ31, Sample-K, processed in the hot condition at $Z = -1$ mm. 73
5.56 Electrical conductivity measurements performed on AZ31, Sample-K, processed in the hot condition at $Z = -2$ mm. 73
5.57 Electrical conductivity and hardness profiles, performed at $Z = 0$ mm, superposed with macrograph of the FSP AZ31 processed in the hot condition, Sample-K. 74
5.58 Electrical conductivity and hardness profiles, performed at $Z = -1$ mm, superposed with macrograph of the FSP AZ31 processed in the hot condition, Sample-K. 74
5.59 a) Macrograph of AZ31 processed in the hot condition, Sample-K. b) Detail of the difference between the microstructures of the base material and the stirred zone. c) Fine-grained stirred zone. d) Base material with a typical solidification structure of a cast AZ31. 74
5.60 Macrograph of the FSP lead, Sample-L, processed in the hot condition. The dashed lines indicate the depths at which the conductivity measurements were performed (from top to bottom: $Z = 0$ mm; $Z = -1$ mm; $Z = -2$ mm). 75
5.61 Electrical conductivity measurements performed on FSP lead, Sample-L, processed in the hot condition at $Z = 0$ mm. 75

5.62 Electrical conductivity measurements performed on FSP lead, Sample-L, processed in the hot condition at $Z = -1$ mm. 76
5.63 Electrical conductivity measurements performed on FSP lead, Sample-L, processed in the hot condition at $Z = -2$ mm. 76
5.64 Electrical conductivity and hardness profiles, performed at $Z = -1$ mm, superposed with macrograph of FSP lead, Sample-L, processed in the hot condition. 76
5.65 a) Macrograph of FSP lead, Sample-L, processed in the hot condition. b) Micrograph of the base material. c) Micrograpah of the stirred zone where an accumulation of impurities can be seen. d) Detail of the accumulation of impurities in the stirred zone. 77
5.66 Macrograph of the AZ31 Sample-N. The dashed lines indicate the depths at which the conductivity measurements were performed (from top to bottom: $Z = 0$ mm; $Z = -1$ mm; $Z = -2$ mm). 77
5.67 Electrical conductivity measurements performed on FSP lead processed in the cold condition, Sample-N, at $Z = 0$ mm. 77
5.68 Electrical conductivity measurements performed on FSP lead processed in the cold condition, Sample-N, at $Z = -1$ mm. 78
5.69 Electrical conductivity measurements performed on FSP lead processed in the cold condition, Sample-N, at $Z = -2$ mm. 78
5.70 Electrical conductivity and hardness profiles, performed at $Z = -1$ mm, superposed with macrograph of sample FSP lead, processed in the cold condition, Sample-N. 79
5.71 a) Macrograph of FSP lead, Sample-N, processed in the cold condition. b) Micrograph of the base material. c) Micrograpah of the stirred with no significant changes in microstructure. d) Detail of the transition between the base material and stirred zone, near the surface of the sample. 79
5.72 Macrograph of the FSP copper Sample-H. The dashed lines indicate the depths at which the conductivity measurements were performed (from top to bottom: $Z = 0$ mm; $Z = -1$ mm; $Z = -2$ mm). 80
5.73 Electrical conductivity measurements performed on FSP copper, Sample-H, at $Z = 0$ mm. 80
5.74 Electrical conductivity measurements performed on FSP copper, Sample-H, at $Z = -1$ mm. 80
5.75 Electrical conductivity measurements performed on FSP copper, Sample-H, at $Z = -2$ mm. 81
5.76 Electrical conductivity and hardness profiles, performed at $Z = 0$ mm, superposed with macrograph of sample Sample-H. 81
5.77 a) Macrograph of FSP copper, Sample-H. b) Micrograph of the base material. c) Detail of the difference between the stirred zone and the base material. d) Microstructure of the fine-grained stirred zone. 81

5.78 Comparison of the variation of electrical conductivity with distance to the weld and processed beads for the materials under study. 82
5.79 Comparison of the percentual variation of the electrical conductivity with the distance to the weld and processed beads for the materials under study. 83

List of Tables

1.1 Materials and respective processing 3

3.1 Functional requirements for the four-point probe 28
3.2 Functional requirements for the positioning device 29
3.3 Functional requirements for the positioning device 30

4.1 Chemical composition of AISI 1020 (wt.%) [70] 40
4.2 Chemical composition of AISI 304 (wt.%) [71] 40
4.3 Chemical composition of Ti Grade 5 titanium alloy (wt.%) [72] 40
4.4 Chemical composition of Ti Grade 2 titanium alloy (wt.%) [73] 40
4.5 Chemical composition of AZ31 Mg alooy (wt.%) [74] 41
4.6 Electrical resistivity of the base materials and relative magnetic permeability (μ_0) at 20.0 °C [70, 71, 74, 72, 73, 75, 76] 41
4.7 Sample geometry 41
4.8 FSP tools dimensions. 42
4.9 Friction Stir Processing parameters 43
4.10 MAG processing parameters 43
4.11 TIG processing parameters 45

Acronyms

FSW	Friction Stir Welding
TWI	The Welding Institute
FSP	Friction Stir Processing
TIG	Tungsten Inhert Gas
MAG	Metal Active Gas
SFSP	Submerged Friction Stir Processing
TMAZ	Thermomechanically Affected Zone
HAZ	Heat Affected Zone
NDT	Non-Destructive Testing
EC	Eddy currents
%IACS	International Annealed Copper Standard
DEMI	Mechanical and Industrial Engineering Department
AC	alternating current
DC	direct current
GUI	graphic user interface
TMAZ	Thermo-mechanically Affected Zone
δ	depth of penetration
σ	electrical conductivity
f	frequency
μ_0	relative magnetic permeability



Introduction

This chapter presents the motivation and the objectives of this thesis and outlines the structure adopted.

1.1 Motivation

Comprehensive knowledge on the correlation between the chemical and physical properties of materials and their structural characteristics is of crucial importance to the development of new products and technologies and the optimization of existing ones. Material characterization is, therefore, critical in the various stages of product development, from design, to production, to maintenance. Several techniques, based on different phenomena, are required in order to, adequately, characterize processed materials and to determine their properties. In the metalworking industry, some characterization techniques, like hardness or metallographic testing, are laborious and time consuming, and may render the material unfit for use. Thus, there is a need for new, dedicated, preferably non-destructive, characterization methods.

Solid-state and fusion joining and processing involve phenomena that lead to the modification of the physical and chemical properties of metals. It is based on that premise that some material enhancement technologies like Friction Stir Processing (FSP) have recently been developed. Other processes inevitably alter materials, although that is not their main purpose. Such is the case of friction stir welding and other, conventional, welding techniques like Tungsten Inhert Gas (TIG) and Metal Active Gas (MAG).

One of the properties that can be altered as a consequence of processing is the electrical conductivity. However, this phenomenon has not been fully exploited from a technological point of view. In fact, work on the correlation between changes in electrical conductivity and physical and metallurgical alterations, inherent to material processing. is limited. This knowledge can prove useful to predict processes, improving production and component performance.

Electrical conductivity testing is commonly applied as a non-destructive technique, in particular by eddy currents and potential drop testing, to detect small size superficial and sub-superficial defects. It can also be applied to the characterization of processed materials and welded joints complementing, or even substituting, techniques such as hardness measurements and metallographic analysis. Additionally, information related to the electrical conductivity field is crucial when Non-Destructive Testing (NDT) based on eddy currents is to be applied. Since defects are detected based on a local change of the electrical conductivity in the material, knowledge on the electrical conductivity field variation due to processing is required in order to distinguish background material from defects.

The existing facilities and knowledge at the NDT group was the driving force for the study performed.

1.2 Objectives

The main objectives of this thesis were:

- to investigate the relationship between electrical conductivity and microstructure studying the effects of solid-state and fusion processing on the electrical conductivity profiles of several materials;
- to increase the technical capabilities of the NDT laboratory of the University's Mechanical and Industrial Engineering Department (DEMI) by developing the technical means necessary for the implementation of the 4-point probe potential drop testing method for material characterization.

The effects of processing - specifically Friction Stir Processing and TIG and MAG welding - on the microstructure and electrical conductivity of materials were investigated by processing or welding specimens of several materials and subsequent characterization with eddy currents, metallographic examination and microhardness testing.

The materials under test were:

Table 1.1 Materials and respective processing

	Material	Process	
		Solid-state	Fusion
Ferrous	AISI 1020	-	MAG
	AISI 304	-	TIG
Non-ferrous	Ti Grade 5	FSP	TIG
	Ti Grade 2	-	TIG
	Mg AZ31	FSP	-
	Lead, Pb	FSP	-
	Copper, Cu	FSP	-

The Non-Destructive Testing laboratory was already well equipped for eddy current inspection and characterization of materials. However, the technical means for an alternative, or complementary, electrical current based characterization method did not exist. To suppress this need and endow the laboratory with additional equipment that could expand its electrical current inspection capabilities, a dedicated 4-point probe potential drop testing equipment was designed, manufactured and tested.

1.3 Document structure

This document is divided into six chapters.

In chapter 2 the state-of-the-art on the subjects relevant to this thesis is discussed, with an emphasis on the effects of solid-state and fusion processing and welding on the

microstructure and mechanical properties of materials, their effects on electrical conductivity and the methods used to assess those effects. This constitutes the theoretical background for the discussion of results.

Chapter 3 describes the development of the new laboratory equipment for four-point probe electrical conductivity characterization.

The experimental procedure is presented in chapter 4. Materials are described along with the welding, processing and characterization methods used.

The results of the investigation are reported in chapter 5 which is divided into seven sections, one for each material. The effects of welding or processing on the electrical conductivity and hardness are discussed.

Finally, chapter 6 presents the main conclusions of this research and suggests future work.

2

State-of-the-art

This chapter provides a revision of the existing knowledge on the subjects relevant to this thesis. Fundamental concepts are introduced and the results of the most significant studies are analyzed. Friction Stir Processing (FSP) is presented and its effects on material microstructure are discussed. Fusion welding is briefly addressed, specifically Tungsten Inhert Gas (TIG) and Metal Active Gas (MAG) welding. The effects of processing on electrical conductivity and eddy currents and four-point potential drop electrical conductivity testing techniques are described.

2.1 Materials Processing

Industrial processes aim at transforming materials in order to produce components and add or create value. In the case of metalworking industries one of the most important processes is welding, a process which enables the fabrication of components of complex geometry that might otherwise be difficult or even impossible to manufacture. Materials processing was performed using solid state and fusion based processes. In the former cathegory are considered Friction Stir Welding (FSW) and FSP while in the last group TIG and MAG welding were used.

2.1.1 Solid-state processes

In materials processing, solid-state processing is a term that can be applied to any material transformation process where fusion does not occur. This definition encompasses a wide range of processes but in this thesis only FSP and FSW will be addressed.

Friction Stir welding and processing

Developed by Wayne Thomas at The Welding Institute (TWI) [1], FSW is a solid-state process that represents, perhaps, the most significant breakthrough in the field of metal joining in recent years. The fusionless nature of the process allows the welding of alloys that are difficult to join by conventional fusion methods. In addition, friction stir welded joints display enhanced mechanical properties when compared to the base material [2]. This phenomenon lead to the development of Friction Stir Processing, a surface modification technology based on FSW [3].

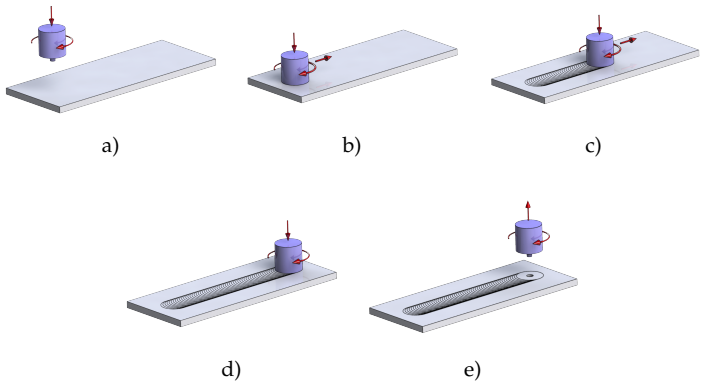

Figure 2.1 Schematic representation of Friction Stir Processing. a) - A rotating tool plunges into the workpiece; b) - Once the material is sufficiently softened the tool begins to travel; c) - Traveling combined with rotation forces the flow of material from the front to the back of the probe; d) - The pressure exerted by the shoulder forges the material; e) - The tool is removed leaving behind a characteristic hole.

The concept behind Friction Stir Processing (figure 2.1) is quite simple. A non- consumable rotating tool, comprised of a cylindrical base (typically referred to as shoulder) and a probe, is plunged into a plate until the shoulder presses the plate. The resulting friction and plastic deformation heat up the material, promoting a viscoplastic state that is fundamental to the process. Once the material reaches this state, the tool can start to travel. This traveling motion combined with tool rotation, forces the material to flow around the probe, from its front to its back. The pressure exerted by the shoulder forges the material, consolidating the bead [4].

FSP alters the microstructure of materials, typically, originating three distinct zones, in regard to the differences in their microstructural features, that can be identified in a macrograph like that of figure 2.2:

- the nugget, or dynamically recrystalized zone, produced due to the intense plastic deformation, at elevated temperature, which causes dynamic recrystallization and generates fine equiaxed grains;
- the Thermo-mechanically Affected Zone (TMAZ), a region where the grain structure is severely deformed at elevated temperatures, but in which the strain deformation is insufficient to cause full recrystallization. Here, some new grain nucleation can occur but the grains remain elongated and deformed due to the material flow around the nugget and precipitate dissolution caused by temperature exposure;
- and the Heat Affected Zone (HAZ), a region of unaltered grain structure that undergoes thermal exposure, exerting a significant effect on precipitate structure. Here, precipitate coarsening and the increase of precipitate-free zone can be observed [4].

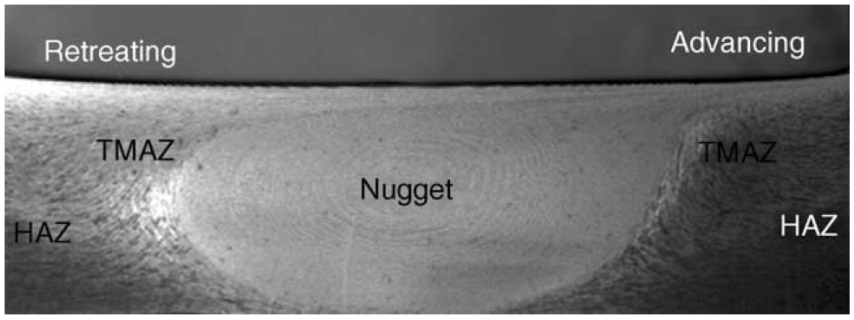

Figure 2.2 Macrograph showing the different zones occurring in FSP materials [4].

The process causes intense plastic deformation, material mixing, and thermal exposure, resulting in significant microstructural refinement, densification, and homogeneity of the processed zone. Therefore, it can be used to provide localized modification and control of microstructures in near-surface layers of processed metallic components [5].

FSP has proven to enhance mechanical properties of some metallic alloys [6–8]. Significant increases in the ductility of ternary aluminum alloys (Al-10%Ti-2%Cu and Al-10%Ti-2%Ni), produced by powder metallurgy, were achieved by friction stir processing [9] and improvements of tensile strength and elongation of a die cast ADC12 Al alloy processed by multi-pass FSP were reported (figure 2.3) [10]. Increases in the fatigue life - attributed to the elimination of casting porosities by FSP - of an investment cast Al-7Si-0.6Mg alloy were obtained (figure 2.4) [11], as well significant increases in the formability of AA7022-T6 and AA5083-O samples processed by in-volume and surface FSP, due the increase in ductility resulting from the refinement of the grain size of the materials [12].

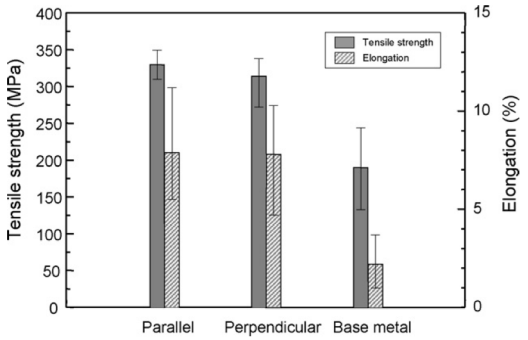

Figure 2.3 Tensile test results of base metal and multi-pass FSP samples for different directions [10].

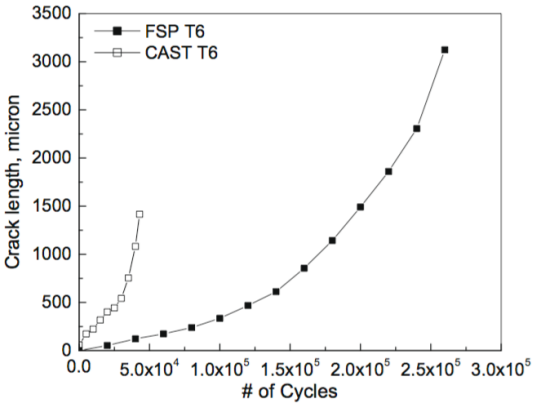

Figure 2.4 Crack length vs. number of cycles, cast + T6 vs. FSP + T6 [11].

Commercial AA7075 rolled plates subjeted to FSP with different parameters have resulted in fine-grained alloys with grain sizes of 3.8 and 7.5 µm. A 1250 % increase in elongation at 480 ºC over a strain rate range of 3×10^{-3} and 3×10^{-2} s^{-1} and 1142% at $500\,°C$ and $3 \times 10^{-3}\,s^{-1}$, for the 3.8 and 7.5 µm specimens respectively, was reported and the importance of the decrease in grain size for significantly enhanced superplastic ductility was noted (figure 2.5) [13].

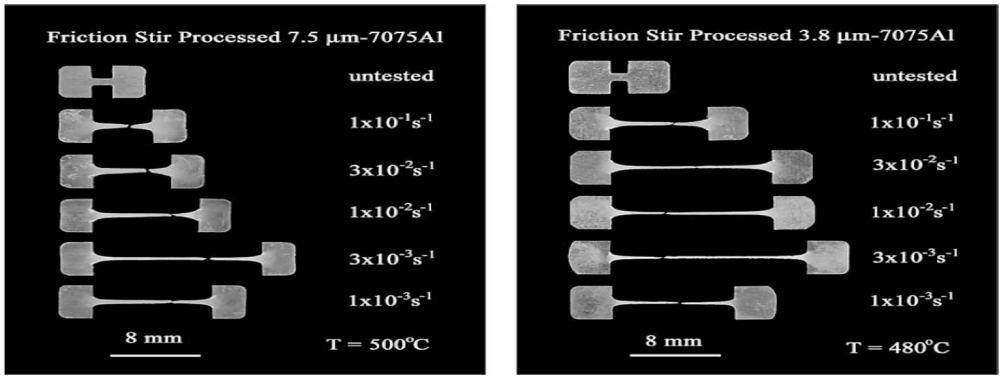

Figure 2.5 Specimens of two FSP 7075Al alloys tested at 500 and 480 °C at various strain rates [13].

The superplasticity of fine-grained FSP Mg-Zn-Y-Zr (4.5 µm grains) and ZK90 (2.9 µm grains) Mg alloys was investigated [14, 15] with the results showing maximum elongations of 1110% at 450 °C and a high strain rate of $1 \times 10^{-2}\,\mathrm{s}^{-1}$, and 1390% at 300 °C and a strain rate of $3 \times 10^{-4}\,\mathrm{s}^{-1}$, respectively.

Studies were conducted to explore the superplastic tensile behavior of a fine-grained AZ91 magnesium alloy prepared by FSP (figure 2.6) [16]. It was found that the FSP AZ91 alloy exhibits excellent superplasticity, and a maximum elongation of 1604% was achieved at 573 K with a strain rate of $1 \times 10^{-4}\,\mathrm{s}^{-1}$ (figure 2.7)).

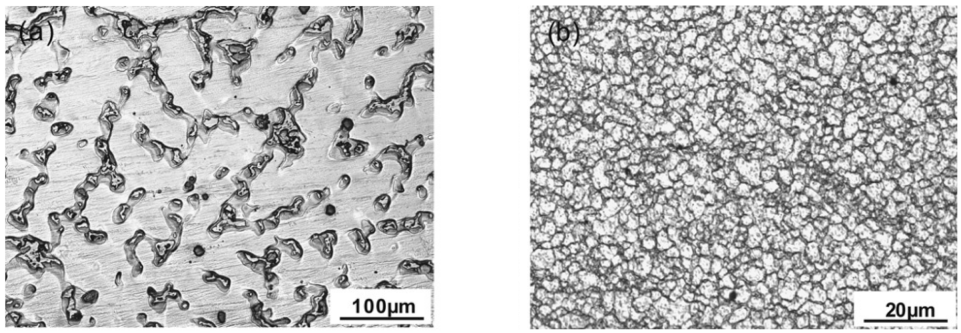

a) Base material b) Material after FSP

Figure 2.6 Ligth micrograph of AZ31 before and after FSP evidencing the difference in grain sizes [16].

Due to the intimate relation between microstructure and mechanical properties, microstructural features of friction stir welded [17–21] and friction stir processed materials [22, 23] have been an important focus of investigation.

One study of the evolution of the fine-grained structure of FSP aluminum used a rotating tool plunge and extract technique and extreme cooling to freeze the initial microstructures of the material [24]. Metallographical examination revealed initial sizes of

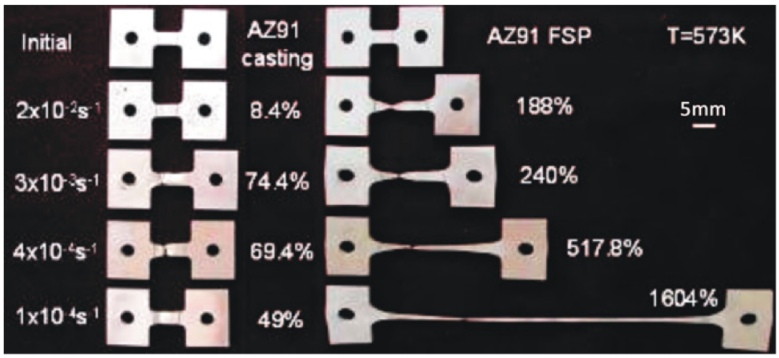

Figure 2.7 Appearance of AZ91 base material and FSP specimens after tensile test at elevated strain rate with a temperature of 573 K. The different microstructures of base material and FSP material lead to different mechanical properties [16].

dynamically recrystallized grains in the processed zone on the order of 25 - 100 nm . After heating for 1 to 4 min at 350 to 450 °C the grains then grew to a size, equivalent to that found in friction-stir processed aluminum, of 2 to 5 µm.

In an effort to create ultra-fine-grained bulk materials Submerged Friction Stir Processing (SFSP) - a variant of FSP in which processing is done underwater (figure 2.8a) - was proposed [25]. The research suggested that SFSP is an improved method for the creation of ultra-fine-grained bulk materials. Water lowers the amount of conductive heat flow, typically, generated by multiple passes of FSP in air. Results indicated that the grain sizes achieved through SFSP could be reduced below 200 nm, even in aluminum alloys, where fast recrystallization kinetics generally prevents ultra refined grain sizes from being obtained (figure 2.8b).

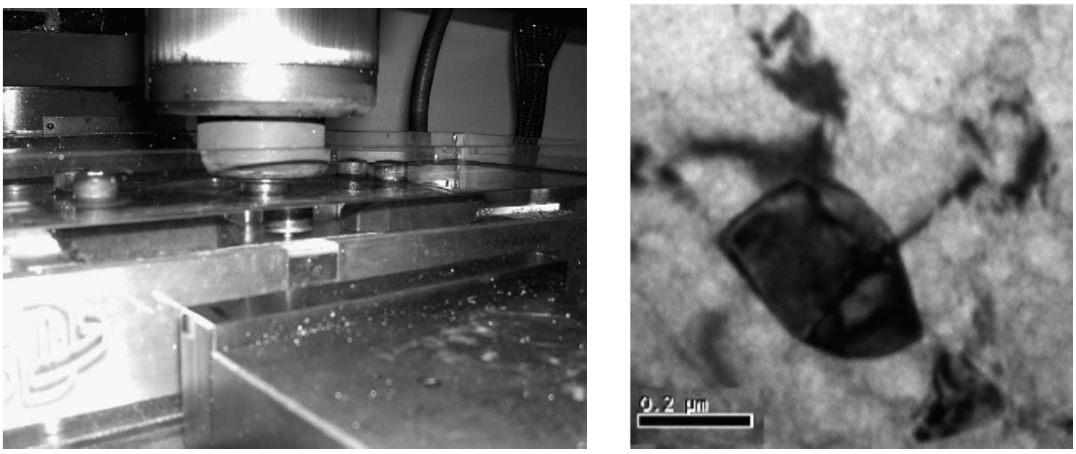

a) b)

Figure 2.8 a) SFSP apparatus and 200 nm grain. b) and micrograph of single pass SFSP in Al-6061–T6 showing 200 and 100 nm size grains [25].

Ultra-fine grain microstructures were achieved in a solution-hardened AZ31 Mg–Al–Zn alloy prepared by friction stir processing equipped with a rapid heat sink (figure 2.9) [26].

The grain boundaries were well defined and the mean grain size was refined from the initial 75 µm to an average grain size between 100 - 300 nm (figure 2.10a) by a single FSP pass. The ultra-fine-grained structure was shown to drastically increase the microhardness from initial 50 up to 120 HV (figure2.11b), demonstrating that with proper control of the working temperature cycles, an ultra-fine and uniform grained structure can be achieved.

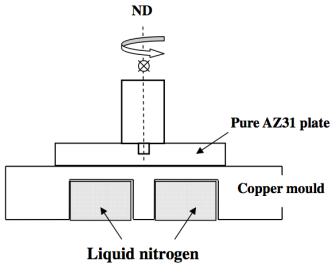

Figure 2.9 Schematic drawing of the FSP with rapid heat sink apparatus conceived by Chang *et al.* [26].

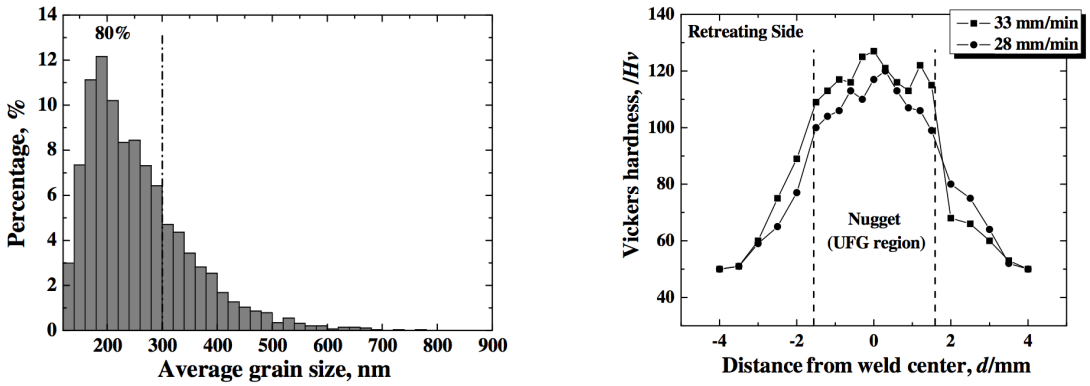

a) b)

Figure 2.10 a) Grain size distribution chart and b) Microhardness profile for FSP AZ31 alloy [26].

A similar study [27] on AZ31 alloy produced nanograined structures with an average grain size of 85 nm. The mean hardness of the processed region reached 1.5 GPa (or 150 HV), about three times that of the matrix. This reinforced the importance of the thermal cycle on the final microstructure, including grain size, grain boundary structure and dislocation density.

The relation between microstructure and hardness

Hardness of an FSP material depends on its microstructural features which in turn depend on processing parameters: tool geometry; rotation and travel speeds; and applied load. All these parameters have an important role in the final properties of the processed material [3, 4, 28–32].

An investigation of the welding parameter dependent microstructure and mechanical properties of friction stir welded pure copper was conducted by Sun *et al.* [29]. After obtaining the window of processing parameters - which included a welding speeds ranging from 200 to 800 mm min^{-1}, rotation speeds between 400 and 1200 rpm and applied loads of 1000 to 1500 kg - the authors concluded that the mechanical properties of the joints could be improved by increasing the applied load, rather than only decreasing the rotation speed at lower applied load. In the stirred zone, a refined microstructure with average grain size of 3.8 µm was obtained by increasing the applied load to 1500 kg (base material grain size was 16.2 µm). The samples welded under 1000 kg (with grain size ranging from 24.1 to 15.4 µm) showed lower hardness in the stirred zone than 100 HV of the base metal and therefore fractured in the stir zone during tensile tests. However, the increase of the applied load to 1500 kg resulted in a hardness increase to about 105 HV and the samples finally fractured in the base metal during tensile tests (figure 2.11).

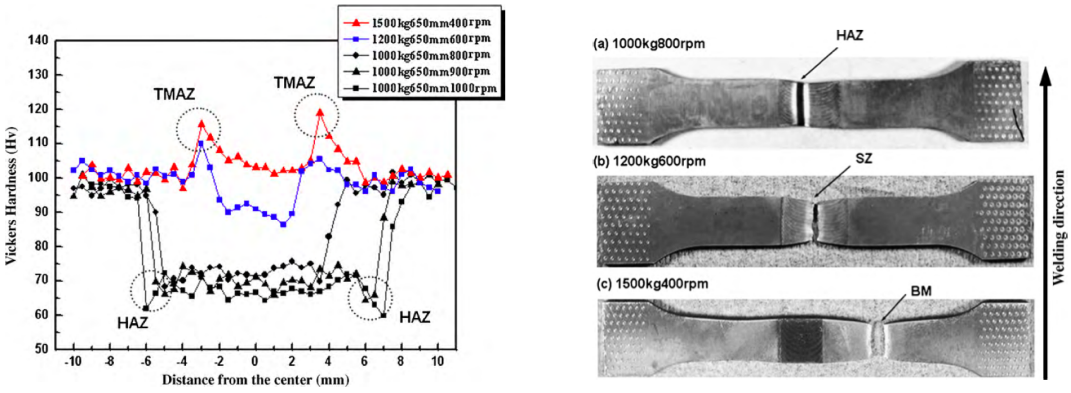

a) b)

Figure 2.11 a) Microhardness profile for FSW commercially pure copper under various welding conditions; b) Appearence of tensile specimen after tests [29].

Using FSW pure copper joints with nearly equal strength to the parent metal were achieved via additional rapid cooling with flowing water [33]. The significantly reduced heat input, resulted in the retainment of the original high dislocation density of the parent metal (2.12a). The yield strength of the FSW Cu joints exhibited a strong linear correlation with the lowest hardness values in the HAZ (2.12b), which was determined by the heat input.

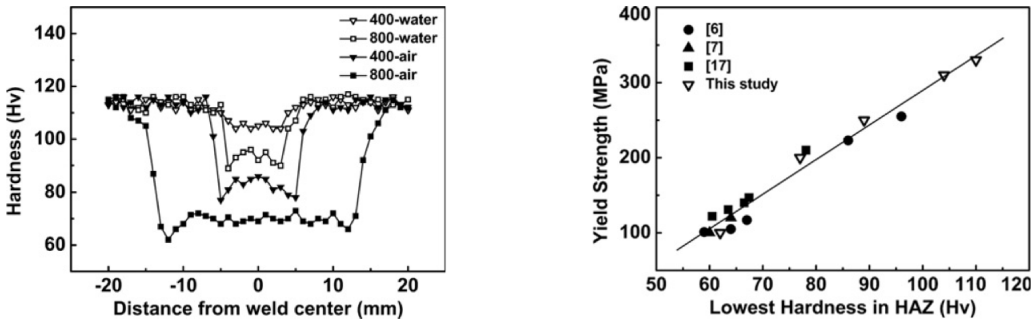

a) b)

Figure 2.12 a) Hardness profiles in crossections of the FSW Cu joints at various parameters; b) Variation of yield strenght of FSW Cu joints with the lowest hardness values of HAZ [33].

A characterization of the microstructural distribution associated with a hardness profile [34] in a friction stir welded , age-hardenable, AA6063 revealed that FSW produced a softened region in the stirred zone. The hardness profile greatly depended on precipitate distribution and only slightly on the grain size (2.13). This relation, between precipitate dissolution and hardness (figure 2.14), was also noted on an investigation on the coupling between precipitation and plastic deformation in relation with friction stir welding of AA2024 T3 [35].

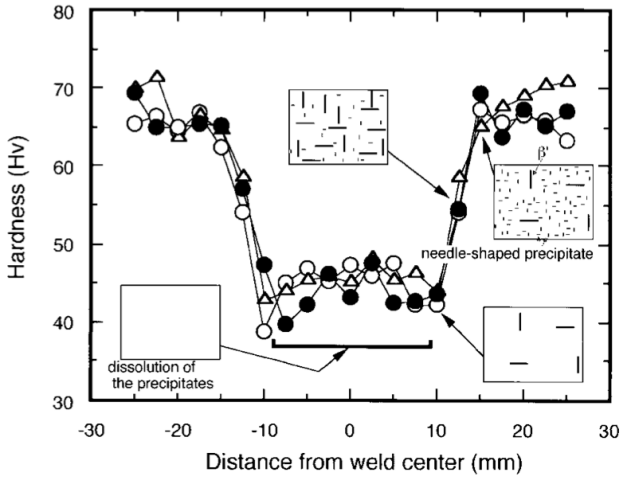

Figure 2.13 Relationship between precipitate distribution and hardness profile [34].

Chen *et al.* [36] studied the effect of grain size on the microstructure and mechanical properties of friction stir welded non-combustive magnesium alloys. Two fine-grained and coarse-grained non-combustive AMX602 (Mg–6%Al–0.5%Mn–2%Ca) magnesium plates with average grain sizes of 1.06 and $6.14\,\mu m$, respectively, were subjected to friction stir welding and the microstructure and mechanical properties of their joints were studied.

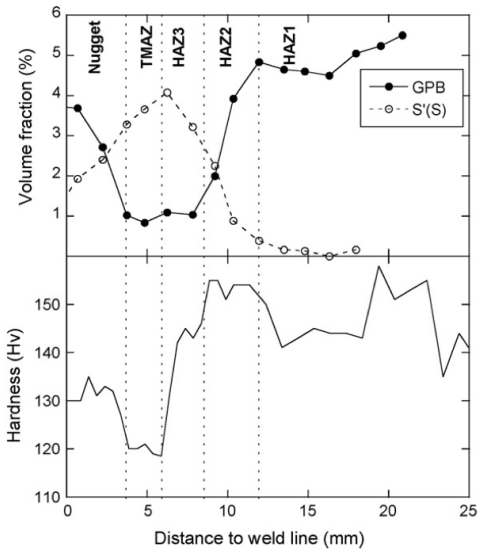

Figure 2.14 Evolution of the hardness, across the retreating side of a FSW 2024 T351, with the volume fraction of precipitates [35].

The authors noted that for the fine-grained AMX602 magnesium alloy, the grains grew in the stir zone, whereas they became smaller in the stir zone of the coarse-grained alloy. This also had an effect on the variation of hardness. The microhardness of all the fine-grained AMX602 magnesium alloy joints was lower than the base material, whereas it became higher in the coarse-grained one (figure 2.15).

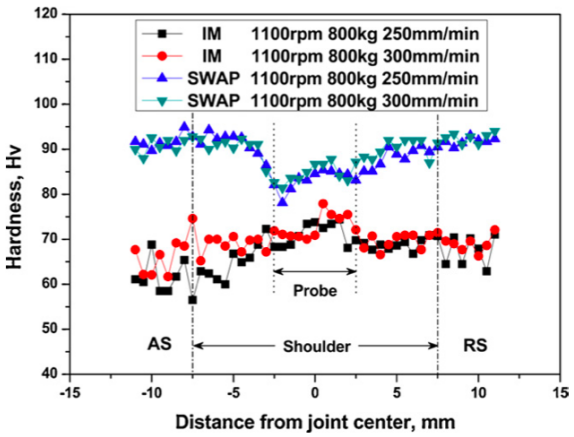

Figure 2.15 Microhardness profile of the fine-grained (SWAP) and coarse-grained (IM) friction stir welded AMX602 Mg alloys joints [36].

2.1.2 Fusion processes

Fusion processes are those in which melting occurs. The most relevant of these are casting and fusion welding. Fusion welding is a generic term used for welding processes that rely on melting to join materials. Due to the high-temperatures reached, liquid-solid phase transformations occur, unlike in the solid/state processes described in section 2.1.1.

In fusion welding, parts are joined by melting and subsequent solidification of the two adjacent surfaces. The microstructure development in the fusion zone depends on the solidification behavior of the weld pool. The principles of solidification control the size and shape of the grains, segregation, distribution of inclusions and porosity. During welding the molten pool is moved through the material, causing a considerable temperature variation across the weld, which will affect the microstructural evolution of the solidified material and reduces residual stresses.

TIG and MAG welding

TIG and MAG are two fusion welding processes that are widely used in industry. TIG is an electrical arc welding process in which the arc is established between a non-consumable tungsten electrode and the plate, under an inert gas (Argon or Helium) protective atmosphere. MAG welding is also an electrical arc welding process. A continuously fed consumable electrode wire establishes the arc, under a protective active gas atmosphere which flows through the torch. This process allows high current densities due to the small electrode wire diameter, which also enables high material deposition rates.

Effects of fusion welding on microstructure and mechanical properties

In a study of the microstructure and mechanical properties of Mg-Li alloy after TIG welding carried out on plates with a thickness of 2 mm (I = 80 A, welding speed v = 30 mm min^{-1} and argon gas flow = 13 l/min), a refined grain microstructure in the fusion zone was reported whereas in the heat-affected zone grain size increased [37].

Yang *et al.* [38] compared microstructure and mechanical properties of Al–Mg–Mn–Er alloy joined by TIG and laser beam. In the case of TIG, 1.7 mm sheets were welded applying a 85 A current, a speed of 30 mm min^{-1} and an argon gas protective atmosphere flow of 15 l/min. Conclusions included a pronounced grain coarsening in the fusion zone of TIG joint, with grain size of about 90 µm.

In a comparison of FSW and TIG welded joints in Al-Mg-Mn-Sc-Zr alloy plates, performed on two conditions of this alloy, namely hot rolled plate and cold rolled-annealed plate, the authors reported that, for each condition, the tensile strength, elongation and welding coefficient of FSW welded joints were higher than those of TIG welded joints. Compared with base metal, the strengths of FSW and TIG welded joints both decreased. For the TIG welding process, the properties of cold rolled-annealed plate were better than those of hot-rolled plate. The FSW welding process yielded better mechanical properties [39]. Also, the stirred zone of FSW and the molten zone of TIG were the weakest zones of the welded joints. For the FSW welded joint, the main reasons presented for the decrease in strength were the loss of substructure strengthening related to recrystallization and loss of precipitation strength of Al_3(Sc, Zr). As for the softening of TIG welded joint,

owing to the melting, the strain hardening disappears entirely and most precipitation strengthening of the second Al_3(Sc, Zr) disappears (figure 2.16).

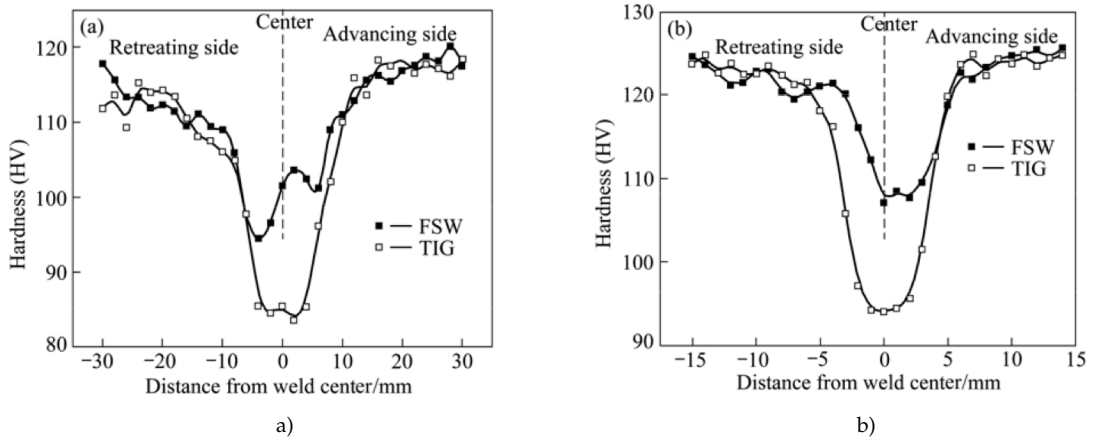

a) b)

Figure 2.16 Microhardness of welded joints. Comparison of TIG and FSW: a) Hot rolled plate; b) Cold rolled-annealed plate [39]

2.2 Effects of processing on electrical conductivity

Macro and microstructure of metals and alloys determine the material behavior. Typical structure-property relationships that have been established using optical metallography include [40]:

- Hall-Petch law relates yield strength and mean grain size. A general increase in yield strength and hardness can be observed when grain size decreases;
- A general tendency for a decreased ductility with increasing inclusion content;
- Correlations of weld penetration, heat-affected zone (HAZ) size, and weld-defect density with the nature and character of the welding;
- Evaluation of such surface treatments as carburizing and induction hardening by determinations of the depth and microstructural characteristics of the hardened region;
- Correlations of fatigue crack growth rates and fracture-toughness parameters with such structural variables as inclusion content and distribution;
- Association of failure initiation sites with microstructural inhomogeneities, such as second-phase particles;
- Correlations of anisotropic mechanical behavior with elongated grains and/or preferred grain orientations.

Processing inevitably alters materials. The knowledge of how and to what extent the material has been altered is, therefore, critical in the design and development of new

materials and to predict and optimize processing parameters that enable better overall performance of components.

In the case of materials that are processed by the techniques described in section 2.1 - FSW, FSP, TIG, MAG - the principal means of microstructural characterization has, usually, been metallographical examination and microhardness measurements. However, there is still a need for dedicated, preferably non-destructive characterization methods.

2.2.1 Microstructure and electrical conductivity

One property that can be affected as a consequence of processing is the electrical conductivity. However, this fact has not been fully exploited from a technological point of view. In fact, there is limited work on the characterization of electrical conductivity variation in processed materials and its correlation with inherent physical and metallurgical phenomena [41]. Little knowledge exists on the variation of electrical conductivity fields and the material behavior that influences the former [42–44].

The electrical conductivity of a material is dependent on its microstructure and could, theoretically, be used to characterize processed materials and welded joints complementing, or even substituting, other existing techniques like hardness measurements and metallographic analysis. This information is also crucial when non-destructive testing based on electrical methods is to be applied [45], as in eddy currents. Defect detection based on a local change of the electrical conductivity in the material requires a previous knowledge of the electrical conductivity field variation due to processing, in order to distinguish background material from eventual discontinuities [46].

The electrical conductivity, σ, of a material is a measure of its ability to conduct an electric current. At a microscopic level, it is related to the movement of electrons through the material. In the case of metals, it is usually expressed in International Annealed Copper Standard (%IACS), which corresponds to the percentage of a standard conductivity of pure copper at 25 °C. An electrical conductivity of 100 %IACS is equivalent to 5.8×10^7 $\mathrm{S\,m^{-1}}$.

In some cases it is useful to express the conductivity in terms of its reciprocal: electrical resistivity, ρ (where $\rho = 1/\sigma$), which can be described as a measure of materials resistance to electron mobility.

Resistivity varies with temperature according to the equation [47]:

$$\rho = \rho_0 + \alpha T \tag{2.1}$$

where ρ_0 is the intrinsic resistivity, which depends not on temperature but on the electron scattering caused by the crystal structure of the material. The temperature dependent term, αT, is the contribution of the electron scattering caused by phonons in the material.

The term ρ_0 can also be divided into contributions due to the crystal lattice ρ_l, impurities and defects ρ_i, and stress and strain ρ_σ. According to Matthiessen's rule (eqn. 2.2):

$$\rho_0 = \rho_l + \rho_i + \rho_\sigma \tag{2.2}$$

This means that the resistivity of a metal alloy also varies with its composition, since both ρ_l and ρ_i vary with the composition.

If resistivity increases with temperature then, its reciprocal, conductivity, σ, will decrease according to

$$\frac{1}{\sigma} = \frac{1}{\sigma_0} + \alpha T \tag{2.3}$$

or, solving for σ,

$$\sigma = \frac{\sigma_0}{1 + \alpha\sigma_0 T} \tag{2.4}$$

where σ_0 is the intrinsic conductivity, analogous to ρ_0.

For a given temperature, the electrical conductivity of a material is, therefore, dependent on its microstructure and composition. This is an important fact because it means that data relative to the conductivity of a material contains information about its structure and composition. Then, by measuring the electrical conductivity of a material that information can be accessed.

Parameters that affect conductivity

Santos *et al.* [44] used eddy currents to study the modification of electrical conductivity by friction stir processing of aluminum alloys in order to identify the major factors governing this property. FSP was applied to AA1100, AA6061-T6, and AA5083-H111 alloys using different parameters. Electrical conductivity profiles were measured at different depths and compared with hardness profiles and microstructures. The authors found that solid-state friction stir processing of aluminum alloys lead to electrical conductivity changes of about 4 %IACS.

It was postulated that, since electrical conductivity, σ, depends on the electrons mobility, it is affected by both mechanical and thermal effects. These include:

- Mechanical - stress (S), strain (ϵ) and the presence of preexisting or induced macro defects (D);
- Thermal - and grain size (G) and precipitate dispersion and morphology (P).

So,

$$\sigma = f(S, \epsilon, D, G, P). \tag{2.5}$$

The individual contribution of each factor was then experimentally assessed and it was determined that the mechanical factors do not significantly affect electrical conductivity, thus allowing the simplification of Eq. 2.5 according to:

$$\sigma \approx f(G, P) \tag{2.6}$$

that is, electrical conductivity mostly depends on the grain size and existence of precipitates. In fact, the authors concluded that grain size is the major responsible factor for the electrical conductivity level since grain boundaries constitute an inevitable obstacle to electron mobility. Thus, an increase of electrical conductivity reflects a grain coalescence phenomena, or alternatively, a decrease of electrical conductivity is observed in grain-refined processed zones. Precipitates were found to mostly affect hardness but not the electrical conductivity, since electrons can easily find alternative flowing paths in a highly conductive aluminum matrix. Finally, the authors showed that, for some FSP applications, electrical conductivity may be a more useful characterization method than hardness to assess material condition, since it identifies different zones like the base material, HAZ, and nugget, more precisely.

2.3 Evaluation of electrical conductivity variations

There is a wide variety of Non-Destructive Testing techniques [45], each of which based on the evaluation of the interaction between the material and one or more of the following forms of energy [47]:

- mechanical;
- acoustic;
- thermal;
- optical (electromagnetic);
- electrical;
- magnetic;
- radiative.

Latest developments have, mostly, focused on variations and incremental improvements of the existing methods [48, 49], automation and intelligent signal processing [50–55], simulation and modulation [56–58].

Despite its common application as a Non-Destructive Testing (NDT) technique in the detection of defects, the potential of conductivity electrical methods as a characterization has not been fully explored. This presents an opportunity for the development of research that has been exploited by the NDT group [42, 44, 59].

For exemple, Santos *et al.* [43] used electrical conductivity testing by eddy currents to perform microstructural mapping of friction stir welded AA 7075-T6 and AlMgSc alloys. The authors performed FSW beads on both alloys with different parameters. Electrical conductivity measurements were carried out using an absolute helicoidal shielded eddy current probe from Olympus (Nortec p/100–500 kHz/ 90.5/6) and a permanent lift-off of 50 mm thin polymer was used. A good correlation between electrical conductivity field, microstructure and hardness of different zones in FSW beads was observed (figure 2.17).

The authors concluded that:

- Electrical conductivity testing can be complementary to hardness to map and characterize the different zones observed on friction stir welded aluminum alloys. The two techniques are complementary in terms of basic phenomena and area of observation;
- For a highly conductive matrix, as aluminum, the precipitates have no relevant effect on the electrical conductivity, which is rather controlled by the grain since observed in the different zones of the weld;
- A good correlation is observed between electrical conductivity and hardness for heat treatable AA7075-T6 but this trend was not identified for the AlMgSc alloy;
- Solid state welding and processing produced significant changes in the electrical conductivity (6% IACS) in heat treatable alloys as AA7075-T6. Those changes were particularly noticeable for the high ratio between the rotating and travel speeds ω/V;
- For the AlMgSc alloy, the variation of electrical conductivity was not relevant (1% IACS) even in hot FSW conditions, since it is a non-heat treatable alloy. As the initial grain size is small, there is no significant grain refining due to processing, so the variation of electrical conductivity is not perceivable.

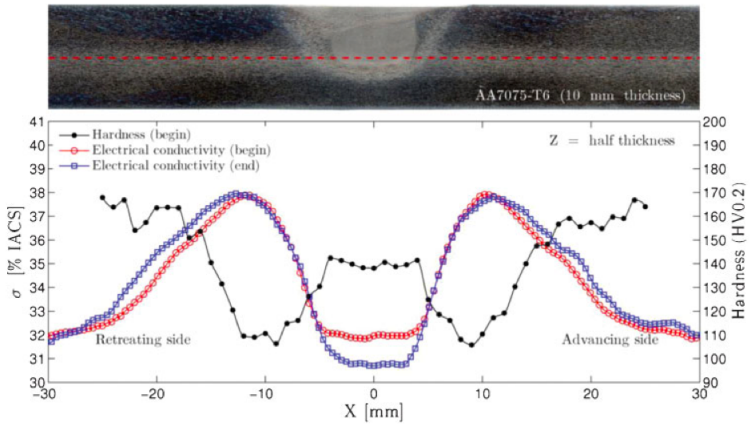

Figure 2.17 Transversal macrograph, electrical conductivity and Vickers hardness profiles of hot FSW bead on plate on AA 7075- T6 10 mm thick plate [43].

The two major electrical conductivity measuring methods are the ones based on eddy currents and those based on potential drop measurements, specifically four-point potential drop techniques.

2.3.1 Eddy currents testing

Eddy current inspection is based on the principles of electromagnetic induction and is used to identify or differentiate among a variety of physical, structural, and metallurgical conditions in electrically conductive ferromagnetic and nonferromagnetic metals and metal parts [46, 60–66]. Its range of applications includes (but is not limited to):

- Thickness measuring of thin metal plates or coatings;
- The detection of defects or surface or sub-surface discontinuities;
- The identification of metal alloys.

Because eddy currents are created by electromagnetic induction, the inspection method does not require direct electrical contact with the part being inspected. The eddy current method is adaptable to high-speed inspection and, because it is non-destructive, can, in some situations, be used to inspect an entire production output if desired. The method is based on indirect measurement, and the correlation between the instrument readings and the structural characteristics of the parts being inspected must be carefully and repeatedly established [45].

Fundamentals

When a coil, excited by an alternating current, approaches a conductive material, the impedance at its terminals varies. The primary magnetic field, associated with the current passing through the coil (figure 2.18a) generates eddy currents in the conductive material (figure 2.18b). These currents then generate a secondary magnetic field (figure 2.18c) which opposes the primary field, according to Lenz's law. This causes an imbalance in the flow of current in the coil, which is the cause for the impedance variation.

This technique is very sensitive to surface defects or discontinuities, but has very little sensitivity at great depths [59]. This is due to the tendency of the eddy currents to concentrate near the surface, a phenomenon known as "skin effect". The eddy currents depth of penetration, δ, defined as the depth at which eddy currents density is reduced to $e^{-1} \approx 36.78\%$ of the surface density, is given by

$$\delta = \frac{1}{\sqrt{\pi f \sigma \mu}} \tag{2.7}$$

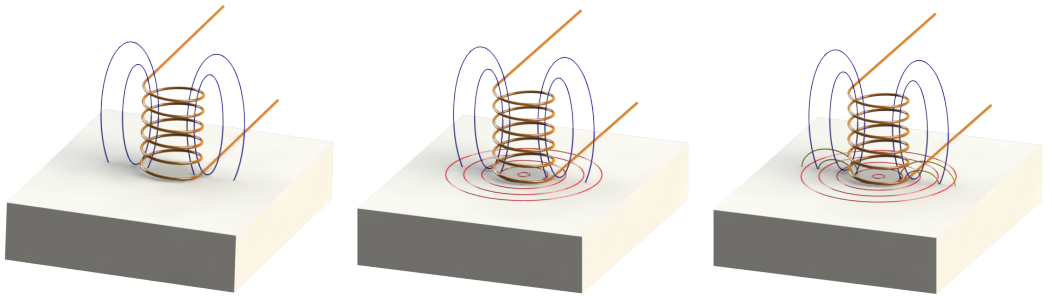

a) Primary magnetic field (blue) b) Eddy currents (red) c) Secondary magnetic field (yellow)

Figure 2.18 Eddy currents: A current passing along a coil generates a primary magnetic field a). The primary magnetic field induces eddy currents in the test material b). In turn these eddy currents generate a secondary magnetic field c).

where f is the frequency of the current in the exciting coil, σ is the conductivity of the material and μ is its magnetic permeability. The conductivity and permeability of a material, as well as its geometry, will, therefore, be the properties that affect penetration of the eddy currents at a given testing frequency. As equation 2.7 shows, by controlling the excitation frequency of the coil, it is possible to control, to some extent, the depth of penetration of the currents.

Usually, only conductive materials can be tested, although thickness measurements of isolating coatings on conductive materials can be performed by measuring the lift-off effect (i.e. the distance between the coil and the surface of the test subject) [47, 45].

The magnetic permeability of the material has a significant impact on the signal. For ferromagnetic materials, the effects of thermal or mechanical processing - which affect magnetic permeability and other properties – can be detected. Yet, some magnetic anomalies due to handling, welding, amongst other causes, can interfere with the interpretation of the material properties. For this reason, ferromagnetic materials are, some times, magnetically saturated prior to inspection, so that they behave as non-ferromagnetic [47].

Advantages and Limitations of Eddy Current Inspection

Eddy current inspection is extremely versatile. It can be applied to many inspection problems, provided the physical requirements of the material are compatible with the inspection method. In many applications, however, the sensitivity of the method can be a disadvantage; some properties or characteristics which are not important in terms of material or part use may cause instrument signals that mask critical variables or are mistakenly interpreted to be caused by critical variables.

Advantages of the method include [67]:

- Portability of the necessary equipment;

- Non-destructive nature of the method;
- Results are instantaneous;
- Safety (non-hazardous method).

Limitations include:

- Limited depth of inspection;
- Some difficulties associated with the inspection of ferromagnetic materials;
- Requires calibration;
- Test material must be conductive (except when measuring the thickness of non-conductive coatings on conductive materials).

2.3.2 4-point probe potential drop testing

Another method used to evaluate the electrical conductivity of materials is the four-point potential drop testing technique, which is well established in various fields: in geophysics they are used to measure soil resistivity in order to reconstruct profiles of soil composition as a function of depth below the surface; in the semiconductor industry they are applied to the characterization of the surface resistivity of semiconductors; and in the context of metal characterization they may be used for accurate conductivity measurements with application to metal and alloy identification and the establishment of damage due to heat exposure thermal cycles.

Four-point measurements of electrical conductivity were developed to overcome the limitations of the two-point technique. In the latter, current and voltage are measured in the same wire (figure 2.19a) and, so, the measured voltage is added to the potential difference in the wires. For materials with high resistivity this method can be used because contact resistance is negligible. For low resistivity materials this method may not be accurate because contact resistance will be very close to sample resistance, increasing the measurement error. The four-point method surpasses this limitation by separating the current and voltage electrodes (figure 2.19b), eliminating the impedance contribution of the wiring and contact resistances.

Fundamentals

In the four-point potential drop method a current source forces an electrical current, I [A], through the external pair of needles and into the test material. Simultaneously, a voltmeter measures the potential drop, V [V], between the inner needles.

Measurements can be performed using either alternating current (AC) or direct current (DC) current. There are differences betweeen the two. AC testing is more complex (both in relation to the phenomena involved and the equipment necessary) but can provide more information, like sample thickness and linear magnetic permeability (μ) [68].

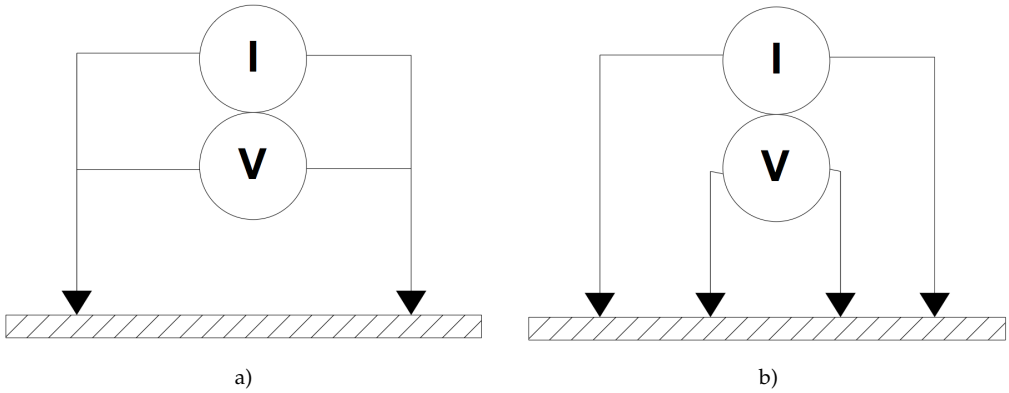

Figure 2.19 Schematic representation of the two-point (a) and the four-point (b) resistivity measurement methods.

The geometry of the sample also has an influence on the measurements. The literature distinguishes between thin plate – where the thickness, t, of the sample is much smaller than the distance, d, between the needles ($t << d$) – and thick plate regimes. Considering that in the experimental work performed in the framework of this thesis, all samples had $t > d$, only the thick plate regime will be discussed.

Probe geometry is also a factor. The way the needles are arranged will determine the potential drop measured. Usually, probe configuration is either rectangular (which will not be addressed in this thesis) or linear. In a linear four-point probe, all four points are placed on the same straight line. Typically, the pickup points are placed symmetrically with respect to the current input/output points.

The simple case of the DC four-point potential drop testing using linearly arranged, equally spaced, probes is represented in figure 2.20.

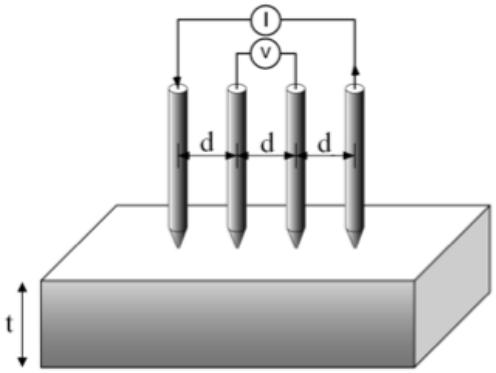

Figure 2.20 Representation of a typical four-point probe.

For linearly arranged, equally-spaced (d), contact points the potential drop in a bulk

material (semi-infinite in lateral dimension and with $t > d$) is a function of the conductivity and is given by [69]:

$$V = -\frac{I}{2\pi\sigma d}. \tag{2.8}$$

Solving equation 2.8 gives:

$$\sigma = -\frac{I}{2\pi V d}. \tag{2.9}$$

Thus, by measuring the potential drop, V, occurring, due to the flow of a known electrical current, d, between two pickup points separated by a known distance, d, the electrical conductivity, σ, can be found.

Advantages and limitations of Four-point probe potential drop characterization

The conductivity of the materials that can be evaluated using four-point potential drop testing can vary several orders of magnitude (σ_{copper} =5.88^{07} S/m, $\sigma_{silicon}$ =1.00^{04} S/m and $\sigma_{alumina}$ =1.00^{-14} S/m), making it a very versatile technique.

Advantages of the four-point probe technique include:

- Linearity - measurement along a specific direction, allow the evaluation of material anisotropy;
- Non-destructive nature of the method - although the needle points can produce indentations on soft materials;
- Can be used to test both conducting and insulating materials (with the proper instrumentation);
- Does not require calibration;
- High resolution (depending on needle spacing).

Its greatest limitation is the dependency on the capabilities of the instrumentation - for highly conductive materials, and very small needle spacing, it requires an equipment capable of measuring micro or nanoVolt in order to detect conductivity variations;

2.4 Conclusions

FSW and FSP produces changes in the microstructure of materials, particularly, in grain size and precipitate distribution, which have an impact on the mechanical properties. Typically, the grain size in the stirred zone decreases due to the intense dynamic recrystallization while, for the TMAZ, the plastic deformation is insufficient to cause recrystallization but grains are deformed and precipitate dissolution can occur. In the HAZ, contrarily to the stirred zone, grain growth can exist along with precipitate coarsening

and the increase of the precipitate-free zone can be observed. The hardness of the different zones reflects these changes, varying with both grain size and precipitates, two factors that can have concurring effects.

As in solid-state processes, fusion processes change the microstructure of materials, altering grain size and precipitates, with consequences to the mechanical properties.

The same microstructural changes that affect the mechanical properties of processed or welded materials, like precipitates and, mostly, grain size, can have an effect on the electrical conductivity. In fact, an increase of electrical conductivity reflects a grain coalescence phenomenon, or, alternatively, a decrease in conductivity is observed in the fine-grain processed zones. Thus, by measuring the variation of this property, information about the microstructure can be inferred.

Although electrical conductivity is commonly applied as a NDT technique in the detection of defects, its potential as a materials characterization technique has not been fully explored. This represents an opportunity for the development of research that has been exploited by the NDT group, namely, in the use of electrical conductivity to characterize the microstructure of FSW and FSP aluminum alloys. To this end eddy current methods and four-point probe potential drop testing, which has the advantage of being able to detect the anisotropy in the materials, can be applied.

3

Development of laboratory means

One of the objectives of this thesis was to develop equipment capable of performing four-point potential drop inspections. This chapter describes the development of this equipment.

The range of materials that could be accurately characterized with the available equipment was limited to those with electrical conductivities between 1 and 100 % International Annealed Copper Standard (%IACS). Some metallic alloys (and also some other relevant non-metallic materials) have conductivity values outside this range and, so, in order to expand the electrical current based inspection capabilities of the laboratory, there was a need for a complementary technique. The four-point probe potential drop method was chosen since, with the appropriate equipment, it can be used to characterize a wide range of materials, including both conductors and insulators.

No four-point probe potential drop testing capabilities existed in the Non-Destructive Testing (NDT) laboratory and therefore they had to be developed. Essentially, these consist of an integrated system comprising: a four-point probe; an automated positioning system; and a measurement system.

3.1 Functional Requirements

In a very first stage, a careful analysis with the goal of determining the necessary functional requirements was done. These requirements, which served as guidelines for the design and development of the equipment, concern the probe, positioning system and measurement system.

Probe requirements

Probe specifications have an impact on the capabilities of the measurements. The choice of the probe has to comply with the requirements detailed in table 3.1.

Table 3.1 Functional requirements for the four-point probe

Requirement	Comments
Spacing between needles	Smaller spacing offers increased resolution. However, it will also have an impact on the magnitude of the measured potential difference and, consequently, on the necessary resolution of the measuring equipment. This should be taken into account when choosing the probe. The spacing between needles should be smaller than the diameter of the eddy current probes available at the NDT laboratory, so that there is a gain in resolution. This means that the spacing should be smaller than 3 mm.
Arrangement	The four points should be linearly arranged. This can, theoretically, allow the evaluation of the anisotropy of the samples. Also, the electronics for the case of the linearly arranged four-point probe method is the simplest.
Size	A small/compact probe is preferred.

Positioning system requirements

Four-point probe potential drop characterization requires a level a precision in positioning that cannot be achieved manually and, thus, an automated system that complies to the functional requirements described in table 3.2 is necessary.

Table 3.2 Functional requirements for the positioning device

Requirement	Comments/Details
Robustness	The device is intended to be a laboratory equipment and, therefore, portability is not required. In fact, it should be robust and have good stability.
Area of inspection	The equipment should be able to inspect samples with up to 100 x 100 mm.
3-Dimensional positioning	The device should be capable of positioning along the X, Y, and Z axes.
Moving base	Movement of the probe implies movement of the cables which can disturb the measurements. To minimize this effect in the new positioning device, the probe movement during testing should be minimized and it should be the base that moves to position the samples.
Non-intrusive base	The base on which the samples are placed should non-intrusive, regarding its electrical and magnetic properties.
Precision or Speed	There should be the possibility of moving the base in two modes, one that favors precision and the other that favors speed.
Automation	As mentioned above, four-point probe characterization requires precision positioning that cannot be achieved manually and, so, the device should be automated.
Modularity	Given that the above mentioned requirements can apply to other methods of inspection it was decided that the positioning device should be a modular, equipment capable of being adapted for other methods of inspection.
4-point probe specific module	Unlike with eddy current probes, dragging the probe could scratch the surface of the sample and damage the contact needles. Therefore, the four-point probe must be lifted and lowered at each inspection point.
Graphic user interface	The device should be controlled using a computer with an appropriate graphic user interface.

Measurement and acquisition equipment requirements

The role of the measurement equipment is crucial to the four point probe potential drop method. This equipment should comply with the requirements presented in table 3.3.

Table 3.3 Functional requirements for the positioning device

Requirement	Comments/Details
Compatibility	The measurement equipment should compatible with the selected probe and, if possible should be compatible with LabView.
Capabilities	The four point probe method relies on measuring a potential drop in order to obtain the electrical conductivity of a materia according to: $$\sigma = -\frac{I}{2\pi V d}$$ Since d is a characteristic of the probe, and I, although it may be defined by the user, is, ultimately, also limited by the probe, the measurement equipment will depend on the probe that is used. Also, the conductivity of the material has a significant effect on the measurements and, so, it also will affect the choice of this equipment.

3.2 Prototype development

Four-point probe

A commercial four-point probe that met the requirements was acquired from Jandel Engineering Limited (figure 3.1). The probe head has four, linearly arranged, tungsten carbide, needles that are equally spaced, with a 1 mm spacing. Each needle is mounted on a spring so that the contact with the test sample is cushioned, in order not to damage both the probe and the sample. The probe has cylindrical body with a diameter of 25 mm.

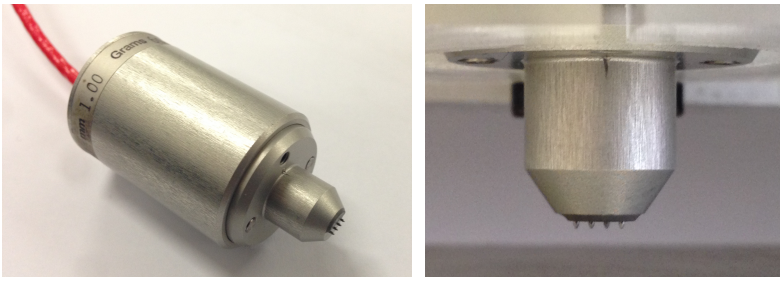

a) Cylindrical four-point probe b) Detail of probe head

Figure 3.1 Four-point probe.

Positioning System - XYZ Table

Since there was no commercially available positioning system that could perform according to the necessary specifications, it was decided that a prototype would be designed and built in-house.

The prototype consisted of an XYZ table developed according to the requirements presented in table 3.2. Dimensions of the moving base (figure 3.2a) were 350×350 mm, with a 150×150 mm area of inspection, attached to two linear guides, mounted on a chassis made of 40×40 mm Bosch Rexroth aluminum strut profiles. This robust chassis ensures the stability of the equipment.

The movement of the base (along the X axis) is provided by either a bipolar stepper motor that drives a threaded rod - for a more precise positioning - or a unipolar stepper motor that drives a timing belt - for a faster positioning (figure 3.2b). Both of these motors are fixed to the chassis. A housing for a threaded bushing connects the threaded rod and/or the timing belt to the movable base. The belt is permanently fixed to the housing whereas the threaded rod is engaged manually, by fastening a headless screw that connects this component to the rod via a threaded bushing.

The chassis also has a vertical pillar that supports an horizontal beam. Mounted on this beam is the Y positioning module. Movement along the Y axis is provided by a bipolar stepper motor that drives a threaded rod which, in turn, is connected to a housing for a threaded bushing mounted on a linear guide (figure 3.2c). The four-point probe module (figure 3.2d) is attached to this housing. This module provides the vertical movement of the probe which, together with the movement on the X or Y axis, enables the operation of the system according to the requirement - lowering the probe, acquiring the data, and lifting the probe at each inspection point, then traveling (along the X or Y axis) before repeating the process at another position (figure 3.2f). Vertical positioning of this module is provided by a bipolar stepper motor which drives a threaded rod. The rod is connected to a gapped stopper with an end-switch, traveling on a linear guide, that supports the probe holder. The gap has sufficient slack for the probe holder to stand, simply supported, under its own weight, once the probe connects to the sample.

Power is supplied to the unipolar and the three bipolar stepper motors by a L293D and three ULN2803AG transistors, respectively. These, mounted on a prototyping circuit board, are controlled using a NI USB-6501 DAQ that interfaces with the computer (figure 3.2e).

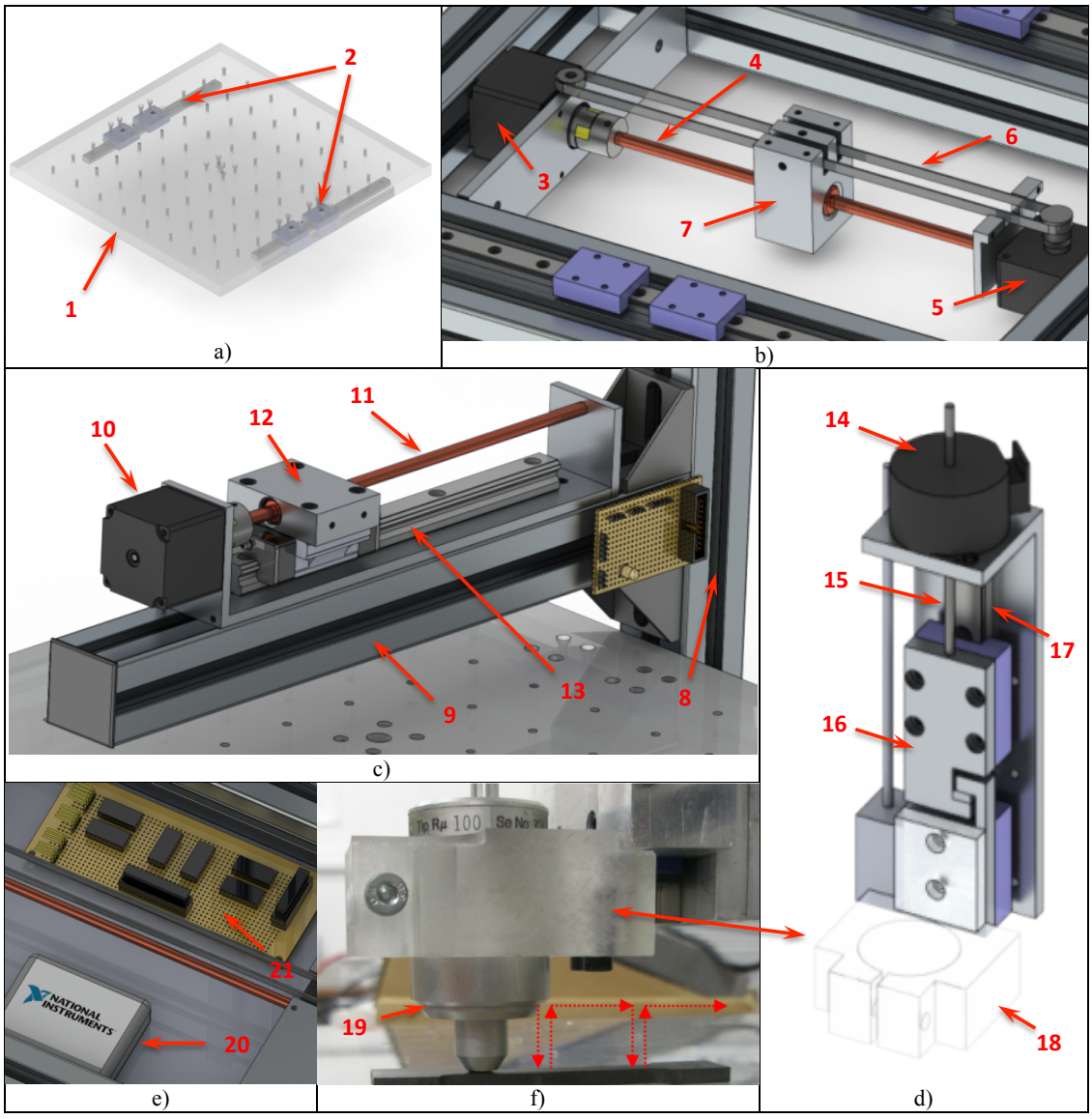

Figure 3.2 Prototype design details (modeled in SolidWorks). a) 1 - Acrylic base; 2 - Linear guides. b) 3 - Bipolar stepper motor; 4 - Threaded rod; 5 - Unipolar stepper motor; 6 - Timing belt; 7 - X axis belt-rod-base connector housing. c) 8 - Vertical pillar; 9 - Horizontal beam; 10 - Bipolar stepper motor; 11 - Threaded rod; 12 - Y axis rod-connector housing; 13 - Linear guide. d) 14 - Bipolar stepper motor; 15 - Threaded rod; 16 - Gapped stopper with end-switch; 17 - Linear guide; 18 - Probe support. f) 19 Four-point probe (photo); 20 - NI USB-6501 DAQ; 21 - Circuit board.

The XYZ table, presented in figure 3.3, is capable of precise positioning. The stepper motors, with 7.5° steps, driving the threaded rods, with a 1 mm revolution pitch, ensure maximum resolution of 0.01 mm in half-step or 0.02 mm in full-step mode.

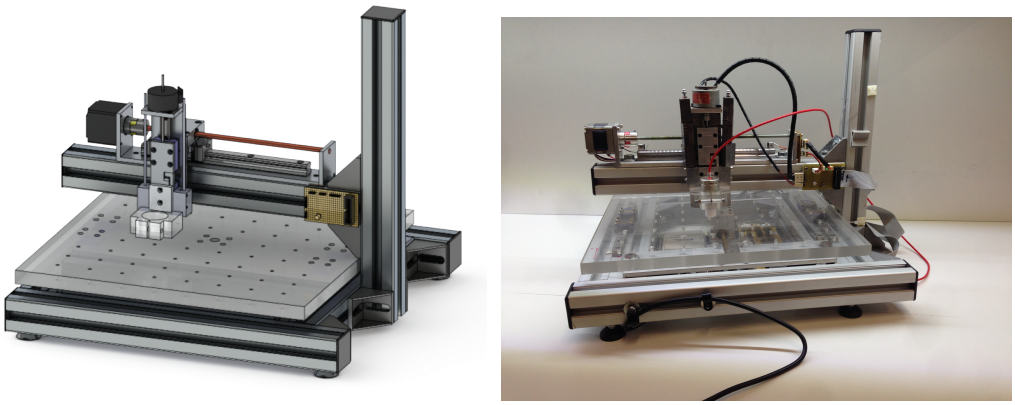

a) XYZ table 3D-model b) Completed prototype

Figure 3.3 XYZ table prototype. a) Rendering of the prototype (modeled in SolidWorks). b) Photo of the finished prototype.

A computer program that enables the control of the equipment through a graphic user interface (GUI) was developed using the LabVIEW software. This program features a Manual Control Mode (Figure 3.4a) - where the user can manually control the probe positioning along the three axes - and an *Inspection Mode* (Figure 3.4b) - where the inspection parameters are defined and the inspection controlled.

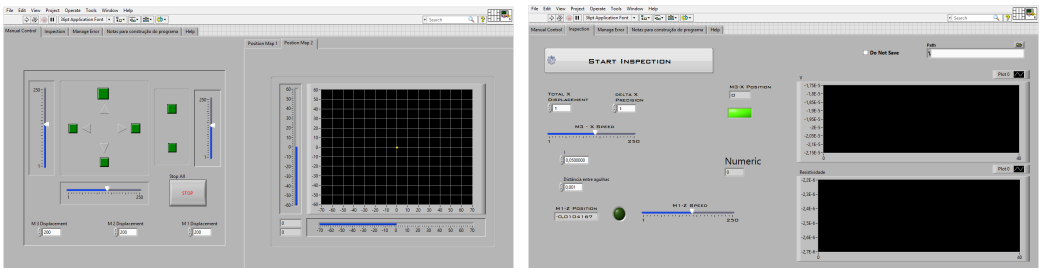

a) Manual control mode GUI b) Inspection mode GUI

Figure 3.4 XYZ table GUI. a) Manual control mode GUI. b) Inspection mode GUI.

Three different inspection modes were developed:

- *I*-Inspection mode - A single-line, single-direction, inspection performed along the X-direction (Figure 3.5a);
- *E*-Inspection mode - A multi-line, single-direction, inspection performed on the XY-plane (Figure 3.5b);
- *S*-Inspection mode - A multi-line, bi-directional, inspection performed along (Figure 3.5c);

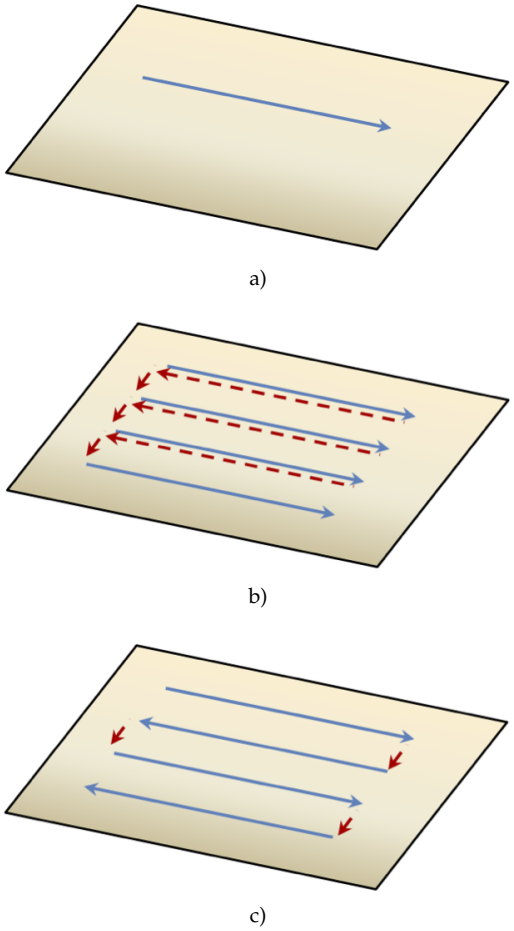

Figure 3.5 Schematics of the different inspection modes. The blue, solid, lines represent the inspection while the red, dashed, lines represent travel. a) I-Inspection mode. b) E-Inspection mode. c) S-Inspection mode.

Measurement and acquisition equipment

The four point probe chosen has a needle spacing, d, of 1 mm, and can handle a maximum current, I of 0.1 A. The conductivity of the materials that can be tested (which include good conductors, like copper and aluminium, other, less conductive metals, like stainless steel or titanium, and also electrical insulators like alumina (Al203) and other ceramic materials, or even some polymers, amongst other materials) can vary several orders of magnitude (Figures 3.6 and 3.7). For example, the conductivity of copper is 5.88^{7} S/m whereas that of silicon is 1.00^{4} S/m and that of alumina is 1.00^{-14} S/m. This must be taken into account when choosing the measurement system.

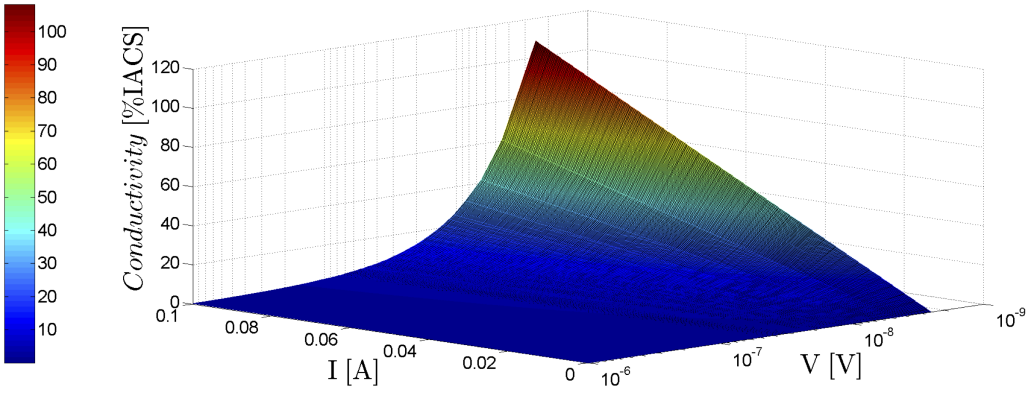

Figure 3.6 Variation of conductivity with potential drop and current, according to equation 2.9.

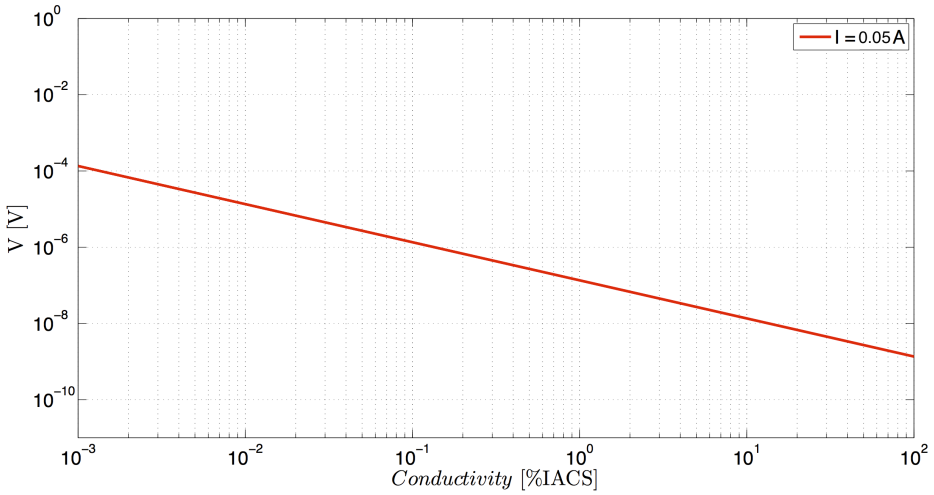

Figure 3.7 Variation of potential drop with conductivity for a probe with $d = 1$ mm and a current of $I = 0.05$ mA.

To measure the conductivity of such a wide range of materials with the selected probe the precision of the measurement equipment is paramount. Assuming an input current of $I = 0.05$ mA, in order to measure conductivities of materials ranging from 1 to 100 %IACS, the equipment must be able to measure potential differences between 10^{-6} to 10^{-9} V (Figure 3.8).

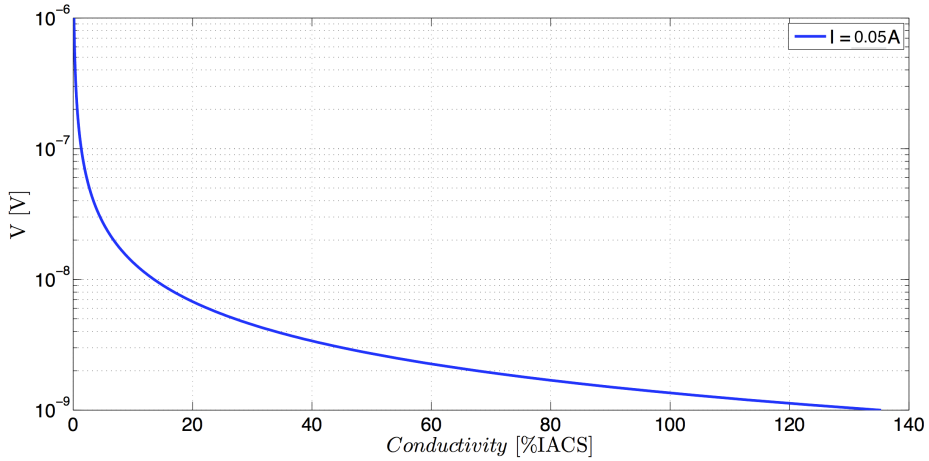

Figure 3.8 Variation of potential drop with conductivity, between 0 and 140 %IACS for a probe with $d = 1$ mm and a current of $I = 0.05$ mA.

A nanovoltmeter that met the criteria defined, the Keithley model 2182A nanovoltmeter which is capable of measuring voltages between 10 nV and 100 V, was identified, however, this equipment was not available in time to be used in this thesis. Nevertheless, validation trials were performed on a material produced by powder injection moulding (PIM), which had a much lower conductivity, and consequently originated a higher potential drop that could be measured using a NI myDAQ data acquisition module that was available at the NDT laboratory.

3.3 System validation trials

For these trials a current source was connected to a digital multimeter, to monitor the input current intensity, before passing through the outer needles of the probe which force the current into the material. The NI myDAQ module is connected to the inner needles and acquires the potential drop measurements data. The setup used can be seen on figure 3.9.



Figure 3.9 Setup of the equipment validation trials.

The samples tested presented inhomogeneities in its microstructure that were detected by the probe as changes in conductivity (Figure 3.11). The inspection is monitored on-line through GUI in the inspection mode (Figure 3.10). The values for the potential drop are presented along with the corresponding values for the resistivity (Figure 3.10) and a data file containing these values is generated so that data can be exported and treated in Matlab. Inspections were performed on several samples of the material.

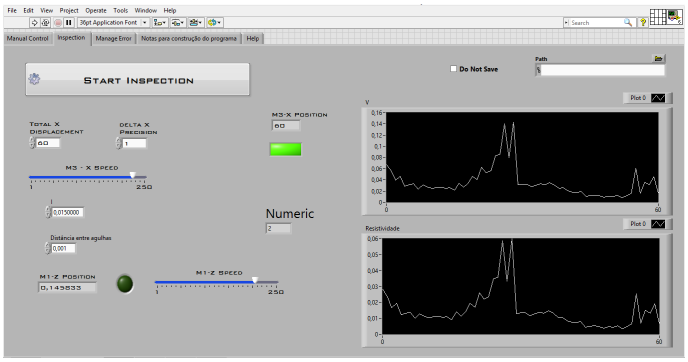

Figure 3.10 Screenshot of the inspection of the PIM material, sample 4.

Eddy current measurements were also done and the results of both trials were compared (Figure 3.12). The measurements of both the four-point inspections and the eddy current inspections show a good agreement with each other and with the macrograph of the samples. The inhomogeneities in the material were identified with the two methods thus validating the method.

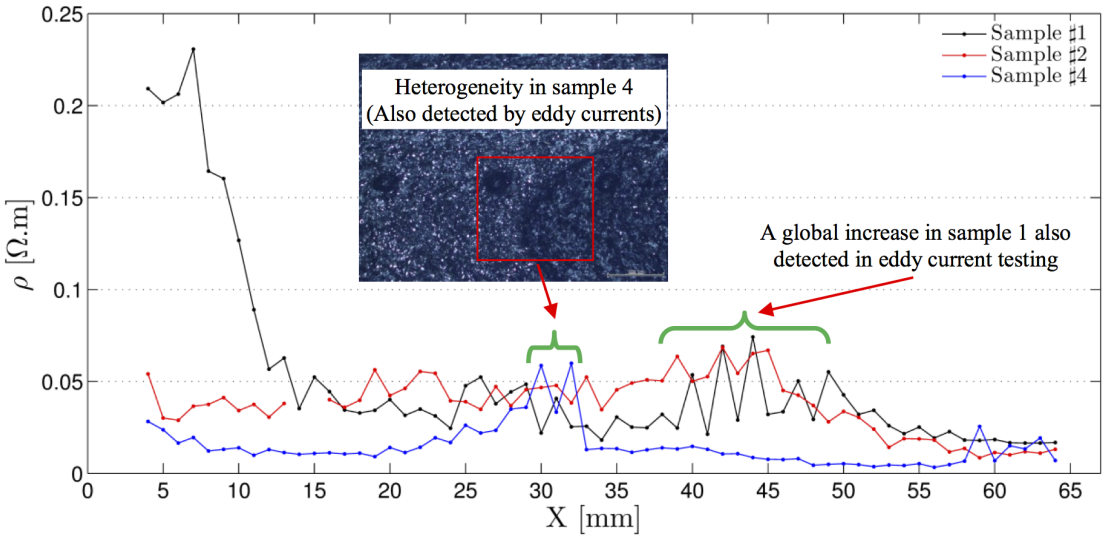

Figure 3.11 Four-point probe electrical conductivity measurements on samples 1, 2 and 4 of a PIM material.

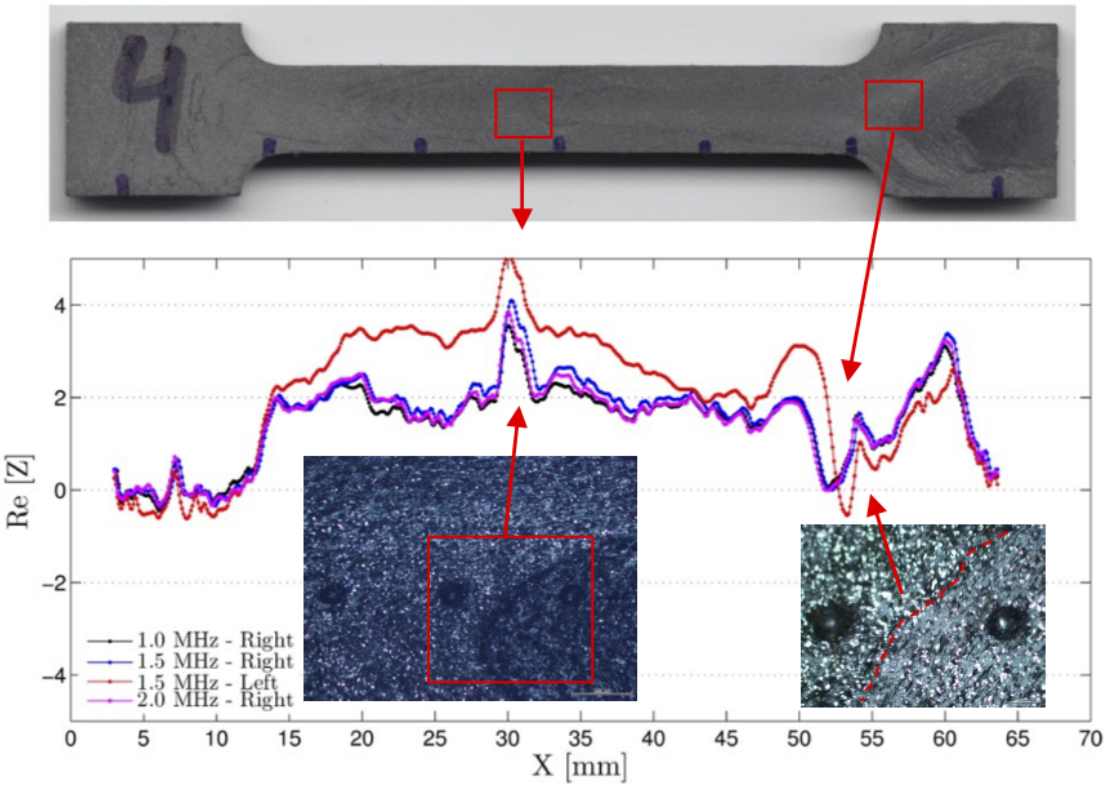

Figure 3.12 Eddy current inspection sample 4 of a PIM material sample for validation of four-point probe trials.

3.4 Conclusions

A prototype for a four-point probe potential drop testing equipment that met the specified requirements was designed, built and tested. Essentially, the prototype consisted of an integrated system comprising: a four-point probe; an automated positioning system; and a measurement system.

The specifications for an appropriate four-point probe were determined and a probe was procured. The necessary automated probe locomotion and positioning system (XYZ Table), including both its mechanical elements, electronics and control elements and the GUI computer software, was designed and built. The specifications for the measurement system were established and an adequate equipment was identified.

Though the equipment could not be tested on metallic materials, due the unavailability of the selected measurement system, validation trials were successfully performed on a PIM material, using an alternative measurement equipment.

4

Experimental procedure

This chapter presents the experimental set-up and test planning. The test materials are briefly described and sample preparation is explained. Finally, testing procedures and parameters are presented.

4.1 Materials

Both ferrous and non-ferrous metals were studied. The investigated materials were selected for their industrial relevance and their physical properties.

The materials used in this research were:

- Ferrous metals:
  - AISI 1020;
  - AISI 304;
- Non-ferrous metals:
  - Titanium Ti Grade 5 alloy;
  - Titanium Ti Grade 2 alloy;
  - AZ31 magnesium alloy;
  - Lead, Pb;
  - Commercially pure copper, Cu.

The following tables present the chemical composition of the materials under study.

Table 4.1 Chemical composition of AISI 1020 (wt.%) [70]

C	Fe	Mn	P	S
0.17 - 0.23	99.08 - 99.53	0.30 - 0.60	0.040	0.050

Table 4.2 Chemical composition of AISI 304 (wt.%) [71]

C	Cr	Fe	Mn	Ni	P	Si	S
0.08	18 - 20	66.35 - 74	2	8.0 - 10.5	0.045	1.0	0.03

Table 4.3 Chemical composition of Ti Grade 5 titanium alloy (wt.%) [72]

Ti	Al	C	H	Fe	N	O	Other	V
87.725 - 91	5.50 - 6.75	0.080	0.015	0.40	0.030	0.2	0.30	3.5 - 4.5

Table 4.4 Chemical composition of Ti Grade 2 titanium alloy (wt.%) [73]

Ti	C	H	Fe	N	O	Other
Balance	0.10	0.15	0.30	0.30	0.25	0.30

Table 4.5 Chemical composition of AZ31 Mg alooy (wt.%) [74]

Mg	Al	Ca	Cu	Fe	Mn	Ni	Si	Zn
Balance	2.5 - 3.5	0.040	0.050	0.005	0.20	0.005	0.10	0.6 - 1.4

The copper was a standard electrolytic Cu and lead was a typical Pb with some impurities.

Table 4.6 presents data on the electrical and magnetic properties of each tested material according to existing information.

Table 4.6 Electrical resistivity of the base materials and μ_0 at 20.0 °C [70, 71, 74, 72, 73, 75, 76]

Material	Resistivity [Ω m]	Conductivity [S m]	Conductivity [%IACS]	Relative Magnetic Permeability
AISI 1020	1.59×10^{-7}	6.29×10^{6}	10.81	≈ 200
AISI 304	7.20×10^{-7}	1.39×10^{6}	2.39	≈ 1
Ti Grade 5	1.78×10^{-7}	5.62×10^{5}	0.96	≈ 1
Ti Grade 2	5.20×10^{-7}	1.92×10^{6}	3.30	≈ 1
Mg AZ31	9.20×10^{-8}	1.09×10^{7}	18.70	≈ 1
Lead	2.06×10^{-7}	4.85×10^{6}	8.35	≈ 1
Copper	1.70×10^{-8}	5.88×10^{7}	101.18	≈ 1

Table 4.7 presents the sample geometries for the different materials.

Table 4.7 Sample geometry

Material	Lenght [mm]	Width [mm]	Thickness [mm]
AISI 1020	200	150	4
AISI 304	120	95	2.5
Ti Grade 5 (FSP)	200	100	4
Ti Grade 5 (TIG)	100	95	4
Ti Grade 2	100	95	4
AZ31	200	90	4
Lead	200	75	3.5
Copper	200	75	10

4.2 Welding and processing

Different materials were either friction stir processed, Metal Active Gas (MAG) welded or Tungsten Inhert Gas (TIG) welding, according to table 1.1.

4.2.1 Friction Stir Processing

Friction stir processing beads were produced using two tools with the same geometry - concave shoulder and fluted, threaded, probe - but different shoulder and probe diameters (table 4.8).

Table 4.8 FSP tools dimensions.

Tool	Tool dimensions	3D Model
A	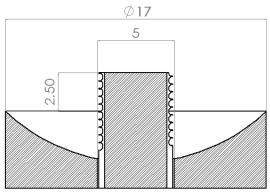	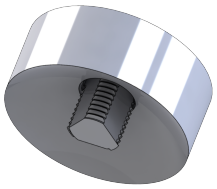
B	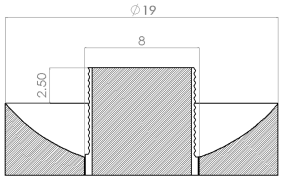	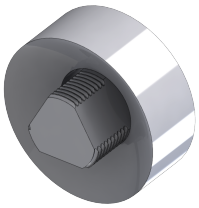

The beads were performed using a conventional milling machine adapted for Friction Stir Processing (FSP) (figure 4.1). The temperature was recorded at 15, 25, 35 and 45 mm from the bead center using K-type thermocouples, a NI 9211 DAQ. An example of the recorded temperature evolution is depicted in figure 4.2.

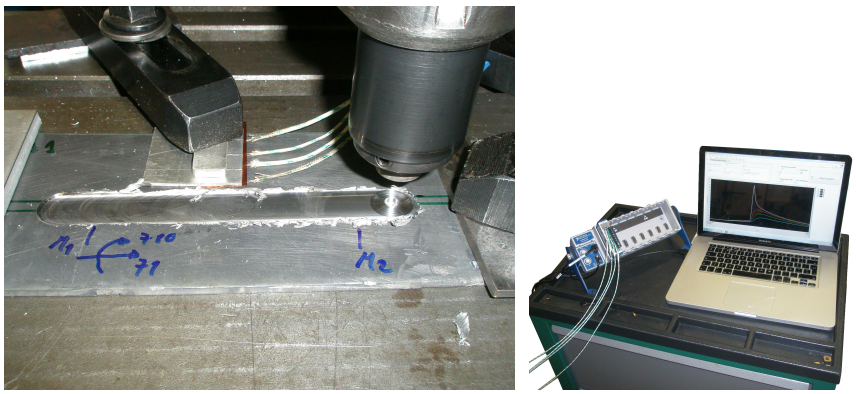

Figure 4.1 Conventional milling machine adapted for friction stir welding and computer set-up for temperature acquisition.

Processing of the AZ31 and the lead was done in the hot and cold conditions, while for copper and titanium alloy only the hot condition processing was performed. The respective processing parameters are presented in table 4.9. The tool tilt angle used for all samples was $1.5°$.

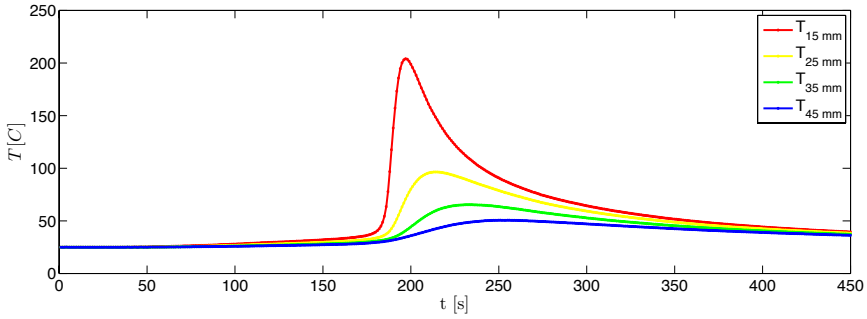

Figure 4.2 Temperature variation during FSP of Ti grade 5.

Table 4.9 Friction Stir Processing parameters

Material	Sample	ω [rpm]	v [mm/min]	ω/v	Tool	T_{max} [°C]
Ti Grade 5	#1	1120	71	15.8	B	204.1
Mg AZ31	#1	560	112	5	A	164.1
	#2	355	355	1	A	n.a.
	#3	710	71	10	A	304.4
Lead, Pb	#1	710	71	10	A	89.2
	#2	560	112	5	A	77.7
	#3	355	355	1	A	52.2
Copper, Cu	#1	1120	71	15.8	B	284

4.2.2 MAG Welding

AISI 1020 steel samples were butt welded (with a 30° V-shaped groove) by MAG. To minimize distortions, caused by the residual stresses created during the process, a customized jig was used to hold the samples in place while welding and until they had cooled down to room temperature (figure 4.3). Temperature was recorded at 15, 25, 35 and 45 mm from the bead using the same equipment as in FSP. However, the data files were corrupted and, so, information on the temperature evolution during MAG was not obtained.

Different parameters - number of passes, current intensity and welding speed - were used (table 4.10) in order to compare the effects at different thermal inputs (H).

Table 4.10 MAG processing parameters

Material	Sample nr.	Passes	V [V]	I [A]	v [mm/min]	H [kJ] (per pass)
AISI 1020	#1	4	17.6	113	166	0.72
	#2	2	19.5	135	120	1.32

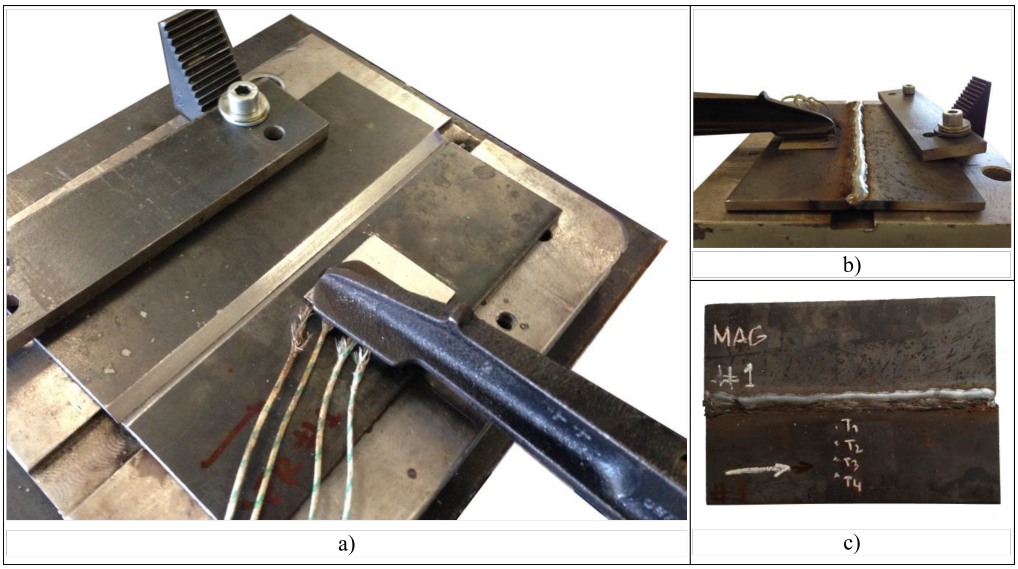

Figure 4.3 a) Jig and thermocouples setup, ready for MAG welding. b) Sample cooling down on jig after welding. c) Welded AISI 1020 sample.

4.2.3 TIG Welding

TIG welding, in a bead on plate configuration, was performed on samples of AISI 304 and Ti Grade 2 titanium alloy. The customized jig mentioned in 4.2.2 was adapted for the geometry of these samples (figure 4.4). Temperature was also recorded at 15, 25, 35 and 45 mm from the bead using K-type thermocouples and a NI 9211 DAQ.

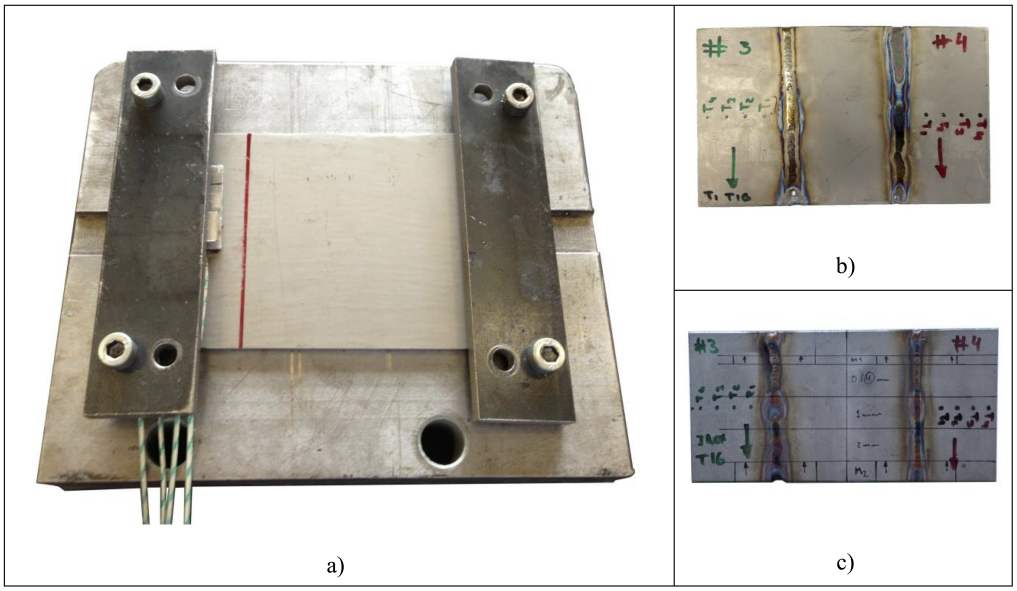

Figure 4.4 a) Jig adapted for MAG welding. b) Welded Ti Grade 5 sample. c) Welded AISI 304 sample.

Beads were performed with different current intensities and welding speeds (table 4.11)

in order to compare the effects at different energy inputs (H). The shielding gas used was Argon.

Table 4.11 TIG processing parameters

Material	Sample nr.	V [V]	I [A]	v [mm/min]	H [kJ]	T_{max} [°C]
AISI 304	#1	15	80	225	0.28	174
	#2	14	60	135	0.20	131
	#3	15	80	138	0.84	297
	#4	14	60	133	0.36	200
Ti Grade 5	#1	15	80	257	0.32	112.3
	#2	14	60	248	0.37	63.6
Ti Grade 2	#1	14	60	60	0.52	264
	#2	15.5	100	257	0.38	226

4.3 Characterization techniques

After processing, all samples were marked for the extraction of specimens for metallographical examination, microhardness measurements and electrical conductivity characterization (figure 4.5).

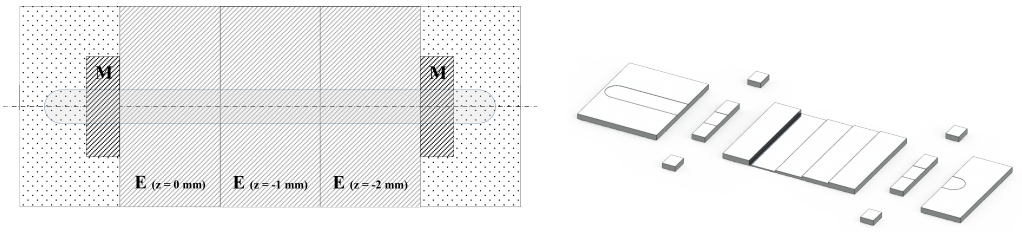

a) b)

Figure 4.5 Schematic representation of sample marking for the extraction of specimens for metallographical examination, microhardness measurements and electrical conductivity characterization (a); Model of specimens extracted from a sample (b).

4.3.1 Electrical conductivity measurements

The specimens for electrical conductivity characterization were machined in steps of 0 (surface), -1 and -2 mm, to perform measurements at those depths.

Electrical conductivity measurements were performed using an Olympus Nortec 500C equipment and two commercial helicoidal, shielded, Eddy currents (EC) probes (Nortec



a) b)

Figure 4.6 Commercial probes (a); Nortec 500C (b).

p/100–500 kHz/90.5/6 and MTF905-60B). Frequencies of 100, 250, 400, 1000 and 2000 kHz were tested.

The Nortec 500C equipment measures the real and imaginary components of the electrical impedance of the probe. Calibration tests for each frequency were done using a certified conductivity standard AL1100F-T0 (Figure 4.7a) and the phase angle was adjusted so that the electrical conductivity variations are given by the real component of the impedance only (Figures 4.7b and 4.7c).

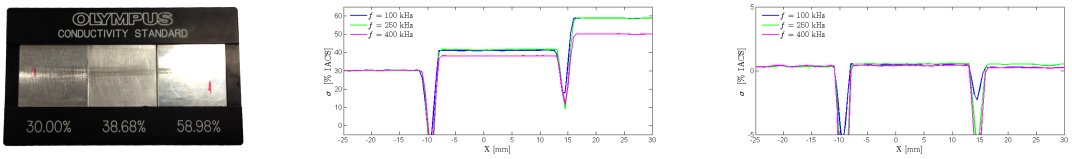

a) b) c)

Figure 4.7 a) Standard conductivity coupons. b) Variation of RE impedance with conductivity. c) No variation of IM impedance with conductivity.

With the above mentioned equipment, 60 mm testing sweeps, with signal acquisition every 0.1 mm, were performed on each of the machined depths of every specimen. An automated scanning device, controlled by computer software, developed in the framework of a previous work was used to ensure the correct positioning and probe movement. The setup of the equipment used in these tests is presented in figure 4.8.

A commercial EC testing instrument was also used to assess the absolute electrical conductivity in the distinct zones. The instrument used was an Olympus Nortec 500 with a SPO-887L conductivity probe. The testing frequency was 60 kHz and calibration was done using a certified conductivity standard AL1100F-T0. Measurements were performed on all machined steps, however, the conductivity of some samples was bellow the limits of the testing instrument and the electrical conductivity could not be measured.

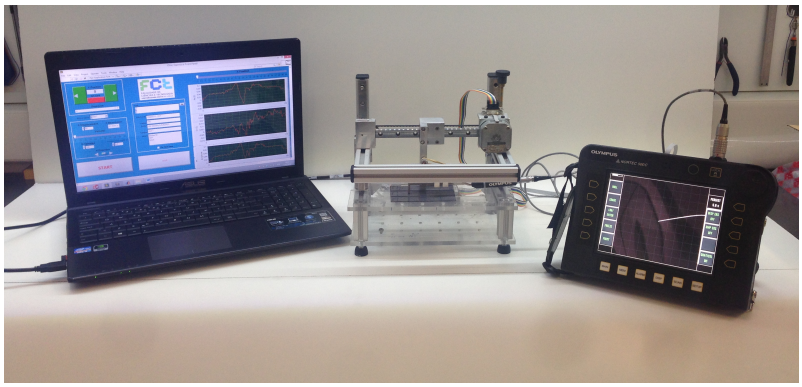

Figure 4.8 Setup of equipment used for conductivity testing.

4.3.2 Metallographical examination and micro-hardness measurements

The specimens from the beginning and the end of the beads were extracted for metallographical examination and microhardness measurements. These were cut, polished and chemically etched with the appropriate reagents to reveal the metallurgical structure of the different zones zones observed under optical microscopy.

Micrographs pictures were taken with an Olympus CX40RF200 optical microscope. Vickers micro-hardness measurements were performed on a Mitutoyo HM-112 hardness testing machine, along the length of the specimens, with 1 mm intervals for in the base material and 0.5 mm in the other zones. These measurements were taken at two depths, sub-surface ($z = 0.250$ µm) and at the mid-height of the weld bead as depicted in figure 4.9). In order for their number and intervals to be approximately the same for each material, the size of the indentations had to be similar for every specimen (considering the large differences in the hardness the materials). For this reason, different loads were used.

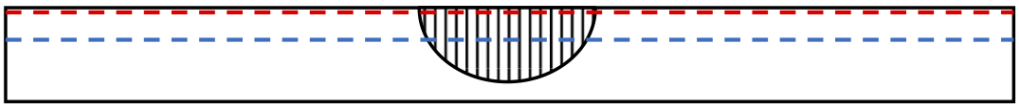

Figure 4.9 Schematic representation of the depth at which microhardness measurements were performed.

4.4 Conclusions

The materials under study were subjected to either FSP, TIG or MAG welding, according to table 1.1. Subsequently, electrical conductivity and microhardness profiles were performed, at different depths, and micrographic examination techniques were applied to determine the conductivity, hardness and microstructure variation, respectively, with the distance to the processing and weld beads and with depth.

5

Results and Discussion

This chapter presents the results of the characterization tests for each material. The effects of processing and welding on the electrical conductivity, hardness and microstructure of the different materials are analyzed and the relation between them is discussed.

5.1 Introduction

Eddy currents (EC) electrical conductivity measurements were performed at 0, -1 and -2 mm from the surface of the specimens. However, since depth of penetration (δ) varies with, both, electrical conductivity (σ), relative magnetic permeability (μ_0) and frequency (f) the actual depth of inspection depends on these parameters and must be considered when analyzing the results. Figure 5.1 shows the variation of δ with the test frequency for the materials under study.

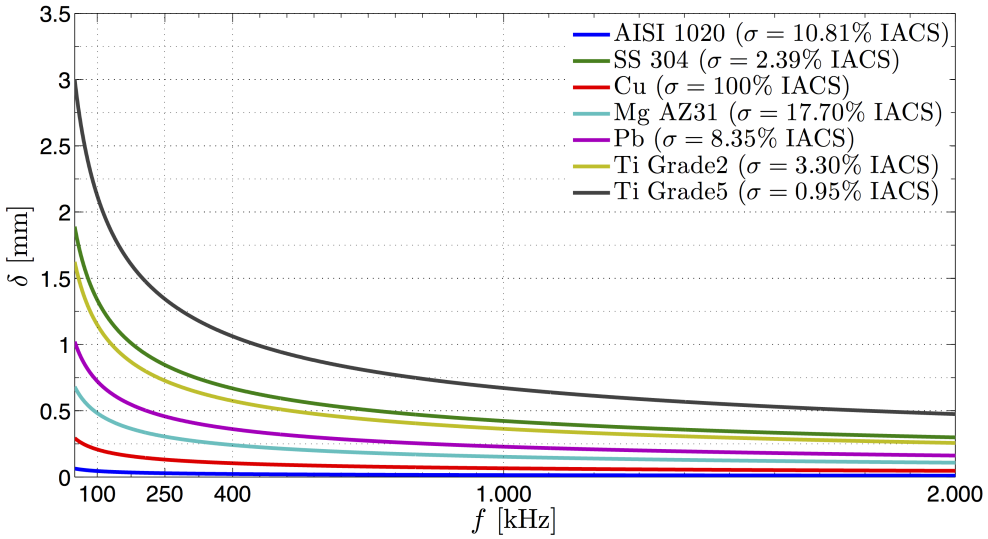

Figure 5.1 Variation of δ with frequency for the materials under study.

As can be seen, the influence of frequency varies greatly with the material. In fact, for the AISI 1020 the μ_0 is much higher than in the other materials and its effect on δ is significant. Because of this, the AISI 1020 shows very little sensitivity to the variation of frequency and the eddy currents tend to concentrate very close (0.1 mm) to its surface, regardless of f. All other materials under study have a relative magnetic permeability of approximately 1. For these cases, the governing property that determines the eddy currents depth of penetration, and its sensitivity to frequency variation, is their electrical conductivity. Consequently, δ for the most conductive material, copper, is the second least sensitive to frequency while for the least conductive one, Ti Grade 5, it can vary from almost 2.5 mm (at $f = 100$ kHz) to 0.5 mm (at $f = 2000$ kHz).

5.2 AISI 1020

The electrical conductivity measurements along the X-axis (perpendicular to the weld bead) of AISI 1020 welded by Metal Active Gas (MAG) show the conductivity variation with the distance to the weld bead at depths of 0 (Figure 5.3), -1 (Figure 5.4) and -2 mm (Figure 5.5) for the tested frequencies: 100, 250, 400, 1000 and 2000 kHz. The detection of the variation of σ at the three depths is consistent with the macrograph of the sample (Figure 5.2).

For the $Z = 0$ mm depth, a good agreement between the conductivity profiles and the macrograph of the sample (Figure 5.2) can be observed. The curves for each frequency display a similar behavior, which indicates that the variations are not random but, in fact, reflect variations in the microstructure of the material. Slight increases in conductivity (that cannot be accurately quantified because the values of the curves do not all match) and a decrease, until about 10 International Annealed Copper Standard (%IACS), occur between $X = -4$ mm and $X = 10$ mm, which closely match the positions and the widths of the heat affected zones and the weld bead, respectively, at this depth.

Measurements performed at $Z = -1$ mm (Figure 5.4) with different frequencies also follow each other closely and display a good agreement with the features observed in the macrograph (Figure 5.2). The presence and extension of the heat affected zones is indicated by an increases in conductivity at between about $X = -4$ mm and $X = -1$ mm and between $X = 6$ mm and $X = 10$ mm, as is the weld bead, between $X = -1$ mm and $X = 6$ mm, by a decrease and stabilization around 10 %IACS.

At $Z = -2$ mm (Figure 5.5) the heat affected zones are not evident in the conductivity profiles. Although the curves for the 1000 and 2000 kHz frequencies display a slight increase in conductivity at the positions corresponding to these zones and clearly identify the weld bead, with a drop in conductivity between $X = -1$ mm and $X = 6$ mm, the same does not seem to occur with the other frequencies tested. For these, the curves exhibit a periodic oscillation which does not seem to have any relation with the structural features observed in the macrograph (Figure 5.2). However, a closer look at the sample reveals segregation bands (Figure 5.6) close to the $Z = -2$ mm depth which are probably the cause of this oscillation.



Figure 5.2 Macrograph of the AISI 1020 Sample-A. The dashed lines indicate the depths at which the conductivity measurements were performed (from top to bottom: $Z = 0$ mm; $Z = -1$ mm; $Z = -2$ mm).

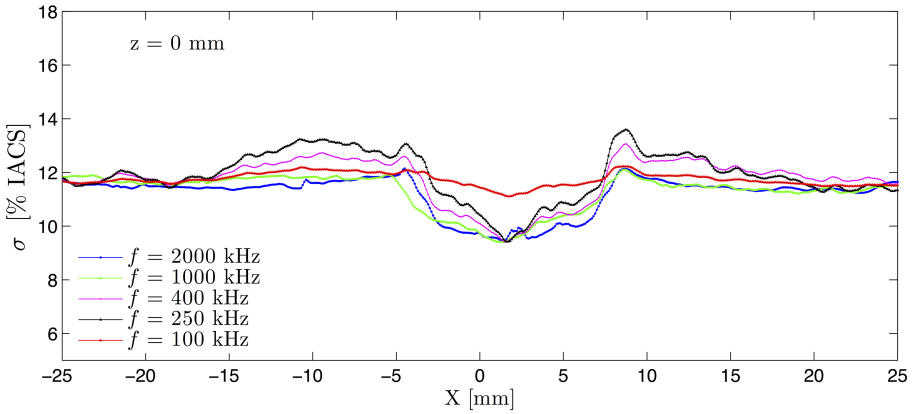

Figure 5.3 Electrical conductivity measurements performed at $Z = 0$ mm on AISI 1020 welded by MAG. Welding parameters: Passes = 4; V = 17.6 V; I = 113 V; v = 166 mm/min; H = 0.72 kJ.

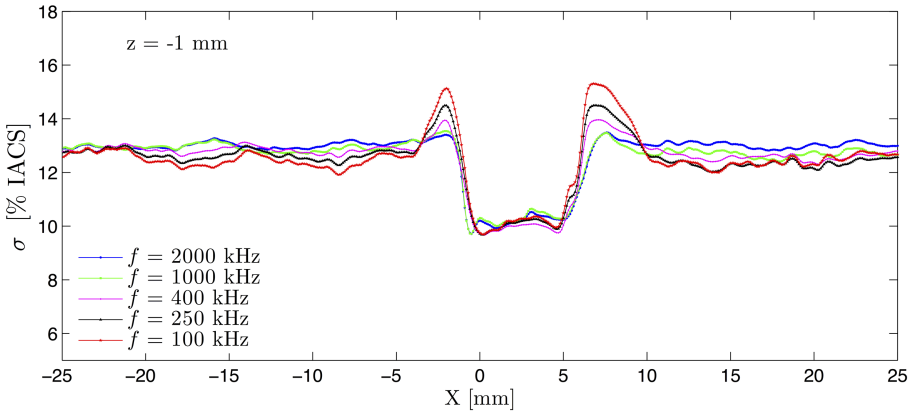

Figure 5.4 Electrical conductivity measurements performed at $Z = -1$ mm on AISI 1020 welded by MAG. Welding parameters: Passes = 4; V = 17.6 V; I = 113 V; v = 166 mm/min; H = 0.72 kJ.

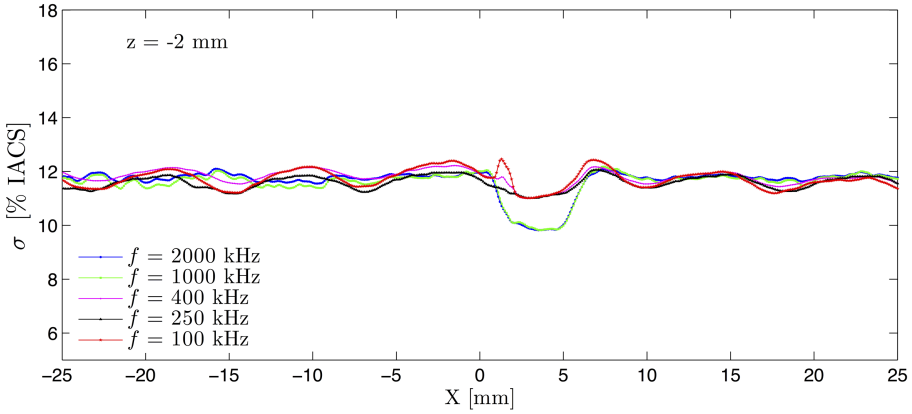

Figure 5.5 Electrical conductivity measurements performed at $Z = -2$ mm on AISI 1020 welded by MAG. Welding parameters: Passes = 4; V = 17.6 V; I = 113 V; v = 166 mm/min; H = 0.72 kJ.

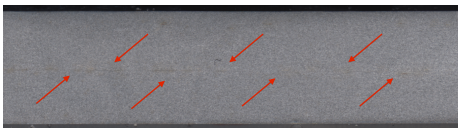

Figure 5.6 Detail of segregation bands present in AISI 1020.

The tests were continued at frequencies of 1000 and 2000 kHz which represent the microstructural features of the weld more accurately, for this material.

Figure 5.7 depicts the variation of electrical conductivity and hardness superposed, with the macrograph, for a depth of 0 mm. The hardness profile exhibits a variation of about 20 HV0.5 in the base material and a sharp increase in the Heat Affected Zone (HAZ) corresponding to perlitic+bainitic existing phases. The hardness decreases in the fusion zone due to the coarse grain solidification structure (Figure 5.8c). The electrical conductivity profile is more consistent in the base material, with almost no fluctuations, which is in agreement with the microstructure of a cold rolled steel plate with ferrite and perlite (Figure 5.8b) The slight increase in the HAZ followed by the drop in the fusion zone is in agreement with the behavior found by Santos *et al* [42, 43] for Al alloys in which the authors concluded that the grain size is the most responsible factor for the electrical conductivity variation. In fact, the hardness and conductivity profiles have an inverse variation similar to that of an object and its mirror image, though the electrical conductivity is less sensitive to very small features, like precipitates, than hardness is.

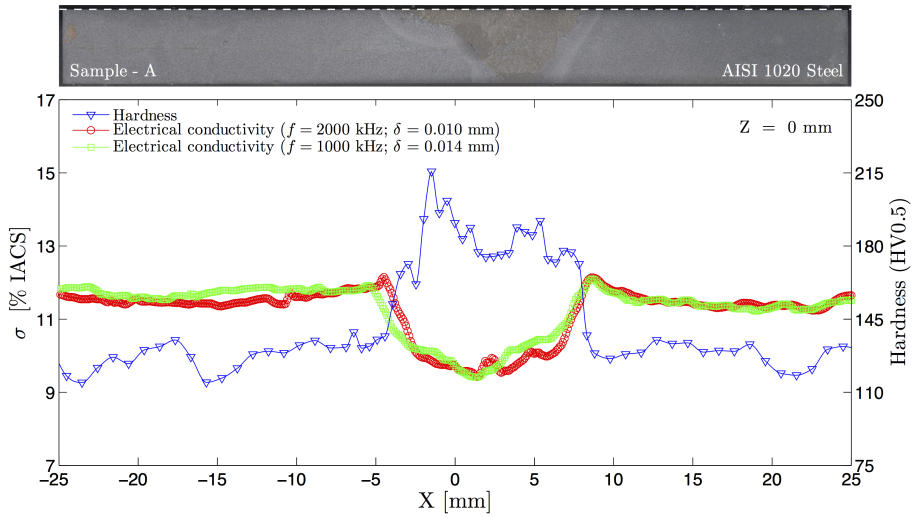

Figure 5.7 Electrical conductivity profile, performed at $Z = 0$ mm,and sub-surface hardness profile superposed with macrograph of AISI 1020 Sample-A. The hardness and conductivity show a good agreement, with an inverse relation. Welding parameters: Passes = 4; V = 17.6 V; I = 113 V; v = 166 mm/min; H = 0.72 kJ.

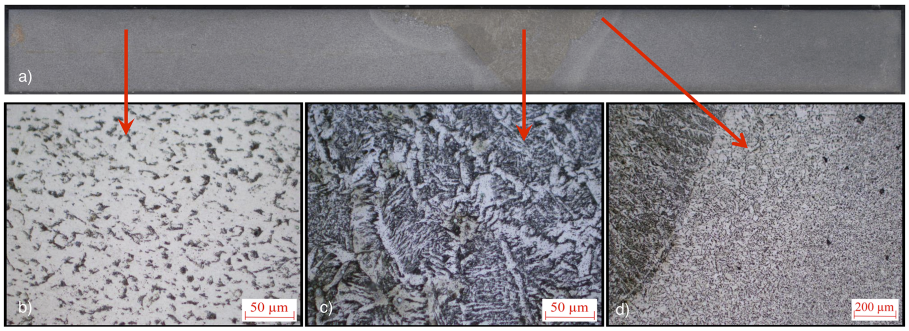

Figure 5.8 a) Macrograph of AISI 1020 welded by MAG, Sample-A. b) The base material exhibits the ferrite-perlite microstructure, characteristic of a cold rolled mild steel. c) A coarse grained solidification structure of pro-eutectoide Widmanstatten-like ferrite and perlite. d) The HAZ has a fine bainitic+perlitic since the steel has a poor hardenability. The fully austenitized zone has a coarse grain size due to its close distance to the fusion zone.

Increasing the heat input (per pass), the electrical conductivity measurements performed on the AISI 1020 show a variation with the distance to the weld bead, at all depths and frequencies tested, that is representative of the changes in microstructure cause by the welding process.

For the $Z = 0$ mm depth the different test frequency curves follow each other closely which, again, suggests that they accurately depict the microstructure of the sample. The frequencies of 1000 and 2000kHz, specifically, practically overlap, which is a good indicator of the repeatability of the method. All curves present a sharp decrease in conductivity, to about 9 %IACS, between around $X = -2$ mm and $X = 10$ mm positions, in agreement with the width of the bead, as is can be confirmed in figure 5.9.

Conductivity measurements at $Z = -1$ mm (Figure 5.11) display a similar behavior to that of figure 5.10, with a decrease in conductivity denouncing the presence of the weld bead. The same is true in the case of the measurements at $Z = -2$ mm. Comparing with the width and position of the weld bead at the respective depths (Figure 5.9), the conductivity curves at 0, -1, and -2 mm represent the change in microstructure due to the welding process quite accurately. Due to the increased heat input the electrical conductivity variation is more pronounced at $Z = -2$ mm in this sample than in the previous one.



Figure 5.9 Macrograph of the AISI 1020 Sample-B. The dashed lines indicate the depths at which the conductivity measurements were performed (from top to bottom: $Z = 0$ mm; $Z = -1$ mm; $Z = -2$ mm).

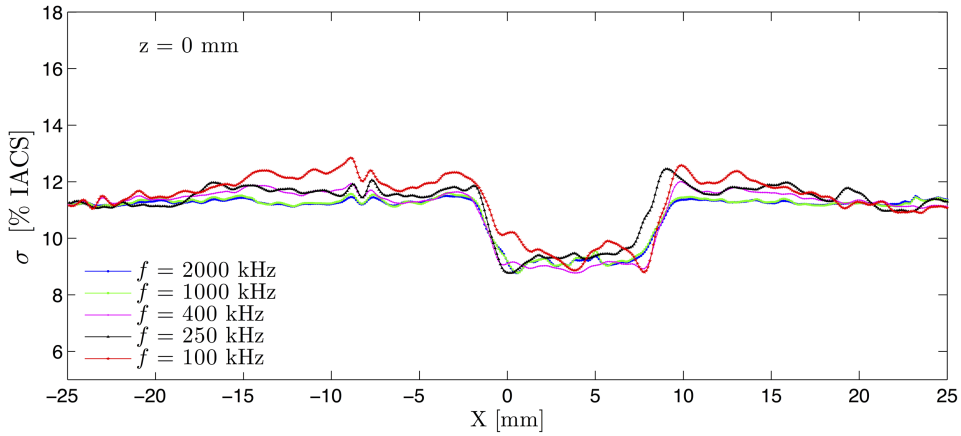

Figure 5.10 Electrical conductivity measurements performed at $Z = 0$ mm on AISI 1020 welded by MAG. Welding parameters: Passes = 2; V = 19.5 V; I = 135 V; v = 120 mm/min; H = 1.32 kJ.

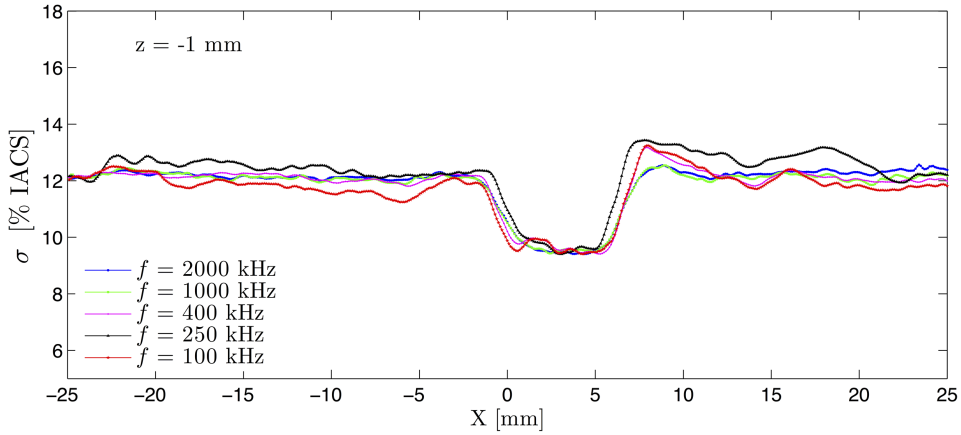

Figure 5.11 Electrical conductivity measurements performed at $Z = -1$ mm on AISI 1020 welded by MAG. Welding parameters: Passes = 2; V = 19.5 V; I = 135 V; v = 120 mm/min; H = 1.32 kJ.

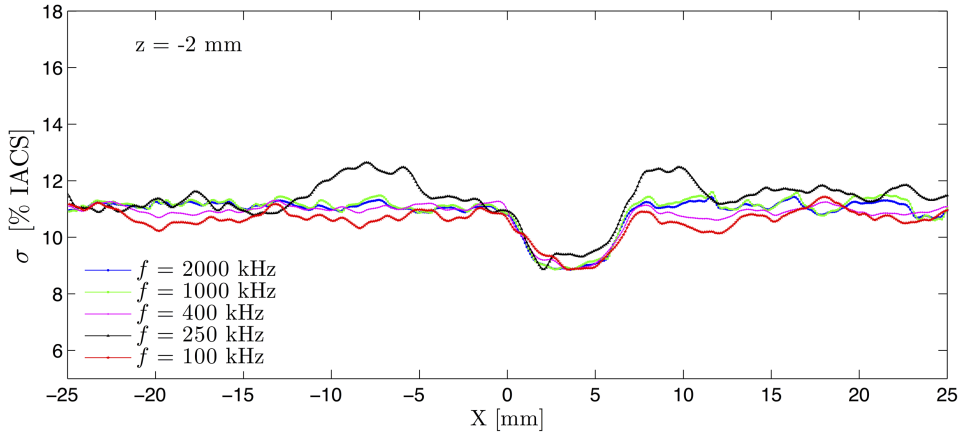

Figure 5.12 Electrical conductivity measurements performed at $Z = -2$ mm on AISI 1020 welded by MAG. Welding parameters: Passes = 2; V = 19.5 V; I = 135 V; v = 120 mm/min; H = 1.32 kJ.

As with the sample welded with a lower heat input, 1000 and 2000 kHz were the frequencies that best represent the microstructural features of the weld and, therefore, the ones used in the following tests.

The hardness and electrical conductivity profiles and the superposed macrograph in figure 5.13 shows that although the operating conditions were different from the previous sample, their microstructures are very similar as well as the σ and hardness profiles.

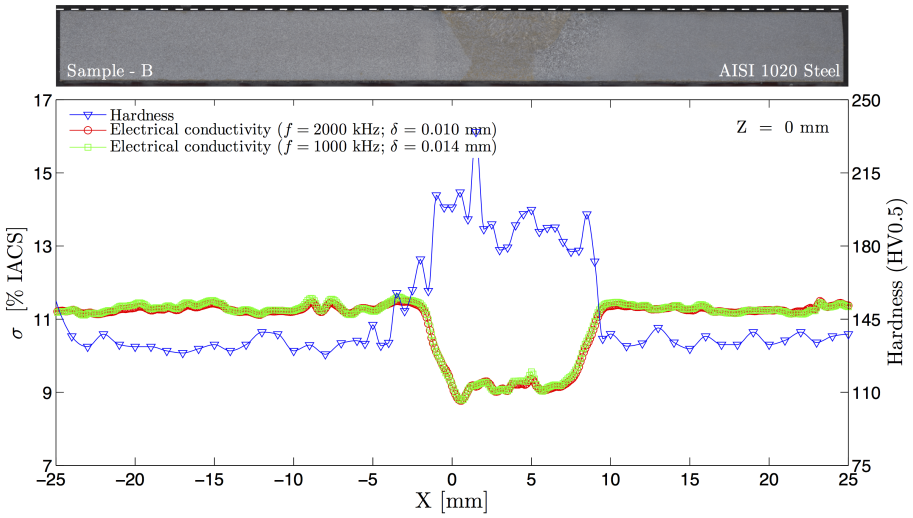

Figure 5.13 Electrical conductivity profile, performed at $Z = 0$ mm,and sub-surface hardness profile superposed with macrograph of AISI 1020 Sample-B. The hardness and conductivity show a good agreement, with an inverse relation. Welding parameters: Passes = 2; V = 19.5 V; I = 135 V; v = 120 mm/min; H = 1.32 kJ.

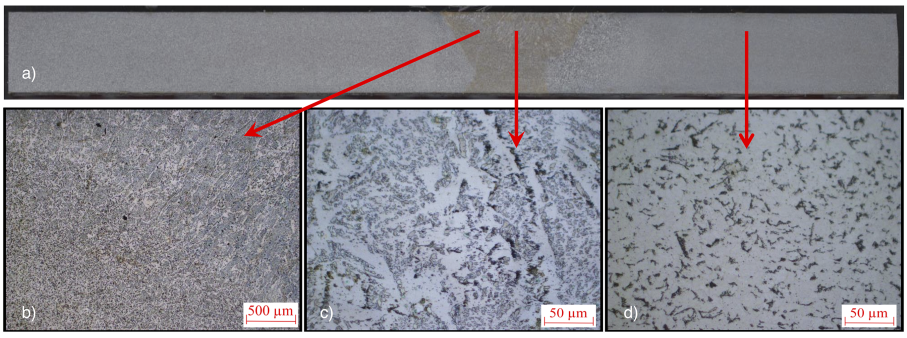

Figure 5.14 a) Macrograph of AISI 1020 welded by MAG with a higher heat input, Sample-B. b) The HAZ has a fine bainitic+perlitic since the steel has a poor hardenability. The fully austenitized zone has a coarse grain size due to its close distance to the fusion zone. c) A coarse grained solidification structure of pro-eutectoide Widmanstatten-like ferrite and perlite. d) The base material exhibits the ferrite-perlite microstructure, characteristic of a cold rolled mild steel.

5.3 AISI 304

Comparing the macrograph of AISI 304, Sample-D, (figure 5.15) and the electrical conductivity measurements at the three different depths (figures 5.16, 5.17 and 5.18) it can be seen that the weld bead is accurately characterized by the conductivity profiles. The curves corresponding to the different frequencies tested match each other very closely, indicating an accurate representation of the microstructure of the material.

At $Z = 0$ mm (figure 5.16), a sharp decrease in conductivity, from 2.3 to 1 %IACS, is observed between about $X = -2.5$ mm and $X = 2.5$ mm. The width and position of this decrease matches those of the weld bead, as can be seen by comparing with figure 5.15.

The conductivity measurements at $Z = -1$ mm (figure 5.17) shows only a small decrease between $X = -2$ mm and $X = 2$ mm. Observing the macrograph it can be seen that this depth corresponds to the bottom limit of the weld bead, thus the decrease in conductivity is so small, compared to that measured at $Z = 0$ mm. The measurements taken at $Z = -2$ mm (figure 5.18) show no significant variation in conductivity since they do not cross the weld bead, as depicted on figure 5.15.

Since this material has a low conductivity, eddy currents can penetrate deep into it. In fact, for frequencies of 100 kHz the currents can penetrate more than half of the thickness of this sample, as can be seen in figure 5.1. For this reason, an to obtain a more accurate representation of the conductivity at the measured depths, the higher frequencies, 1000 and 2000 kHz were used in the subsequent tests.



Figure 5.15 Macrograph of the 304 SS Sample-D. The dashed lines indicate the depths at which the conductivity measurements were performed (from top to bottom: $Z = 0$ mm; $Z = -1$ mm; $Z = -2$ mm).

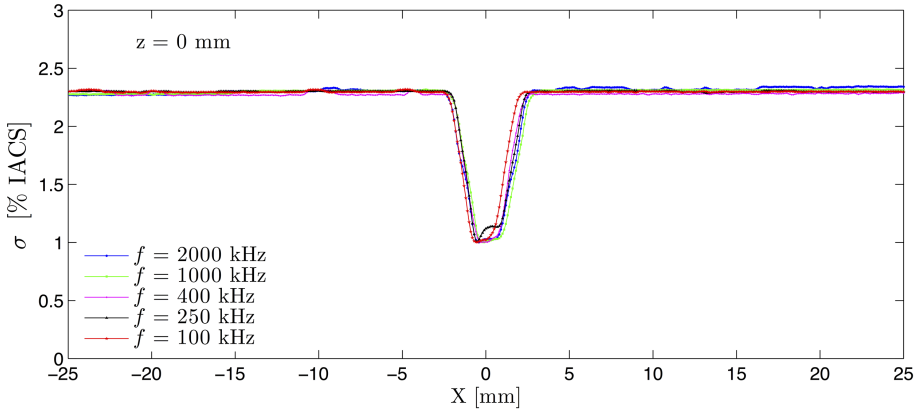

Figure 5.16 Electrical conductivity measurements performed at $Z = 0$ mm on AISI 304, Sample-D, welded by TIG. Welding parameters: V = 15 V; I = 80 V; v = 225 mm/min; H = 0.28 kJ.

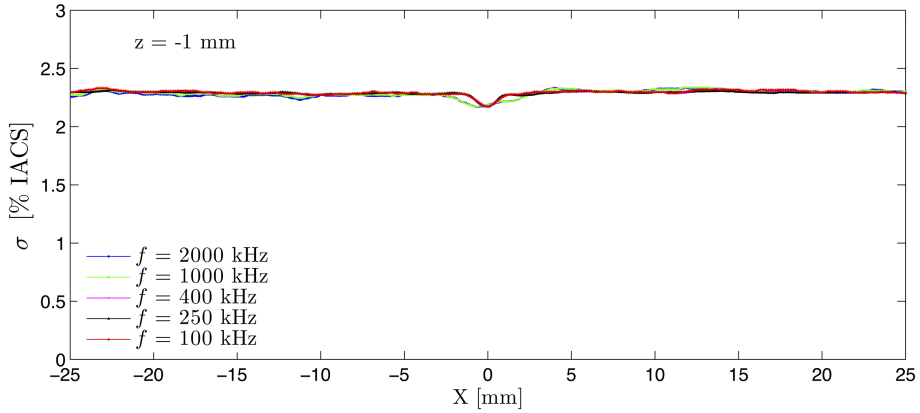

Figure 5.17 Electrical conductivity measurements performed at $Z = -1$ mm on AISI 304, Sample-D, welded by TIG. Welding parameters: V = 15 V; I = 80 V; v = 225 mm/min; H = 0.28 kJ.

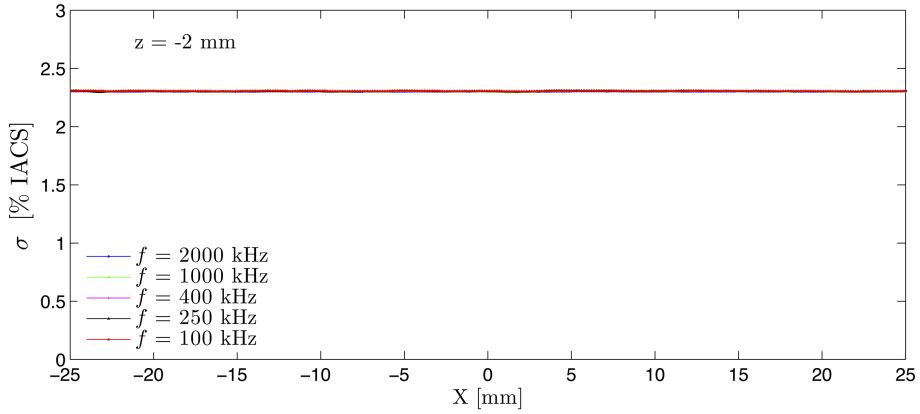

Figure 5.18 Electrical conductivity measurements performed at $Z = -2$ mm on AISI 304, Sample-D, welded by TIG. Welding parameters: V = 15 V; I = 80 V; v = 225 mm/min; H = 0.28 kJ.

For this material the hardness and conductivity profiles, presented in figure 5.19, follow the same evolution, unlike the AISI 1020. In fact, during solidification of the fusion zone in austenitic stainless steel, there is δ-ferrite formation in dendritic arms of austenite (Figure 5.20c). So, if it can be considered that the grain size is larger than in the base material (Figure 5.20b), that a dendritic structure with austenite, δ-ferrite and, eventually, sigma-phase, exists, a drop in electrical conductivity can be justified. However, the presence of these phases usually increases the hardness. If they are present in low contents, their hardening effect may not be perceived since austenite is a ductile, soft, phase. This should be investigated by advanced materials characterization techniques to explain such behavior.

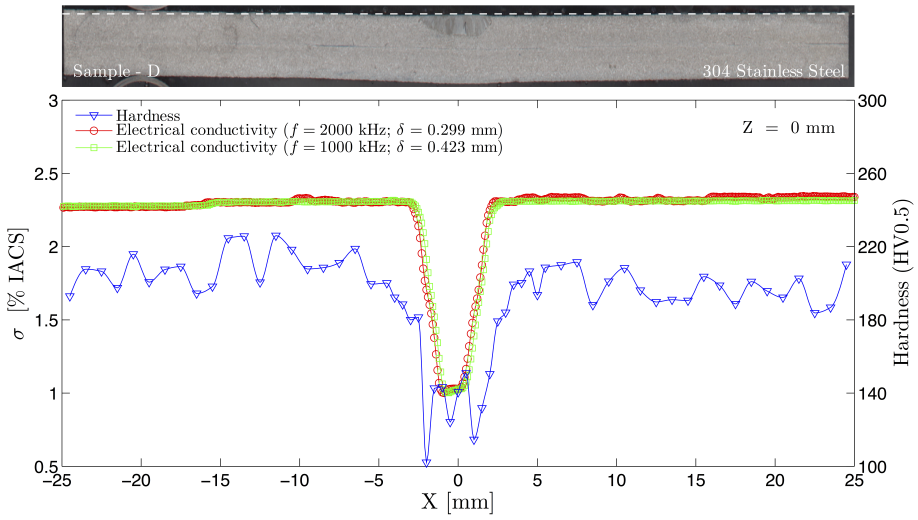

Figure 5.19 Electrical conductivity profile, performed at $Z = 0$ mm,and sub-surface hardness profile superposed with macrograph of AISI 304, Sample-D. The hardness and conductivity profiles display a direct relation. Welding parameters: V = 15 V; I = 80 V; v = 225 mm/min; H = 0.28 kJ.

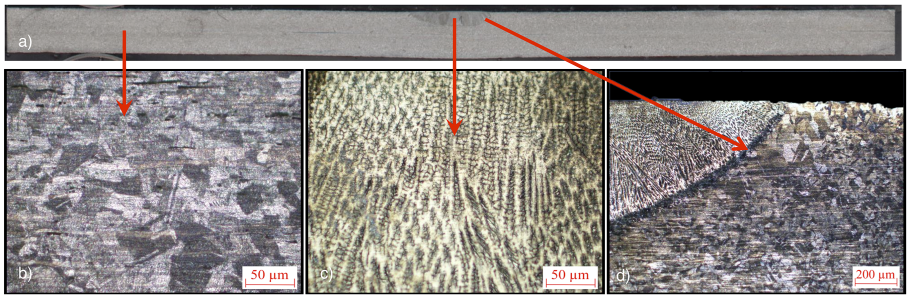

Figure 5.20 a) Macrograph of AISI 304, Sample-D. b) Micrograph of the base material with the typical microstructure of an austenitic stainless steel. c) Solidification structure in the fusion zone with the formation of δ-ferrite. d) Some grain growth in the HAZ.

For AISI 304 Sample-E, which received a higher heat input, the electrical conductivity measurements also represent the weld bead quite accurately at the different depths. As can be seen in the macrograph of the sample represented in figure 5.21, the measurement sweeps at $Z = 0$ mm and $Z = -1$ mm intercept the bead, whereas that at $Z = -2$ mm does not. This is reflected in figures 5.23, 5.23 and 5.18, where in the first two, the conductivity decreases to about 1 %IACS in the position and with the widths corresponding to the bead at those depths, while for $Z = -2$ mm no variation occurs since the root of the weld bead is not that deep into the material.



Figure 5.21 Macrograph of the 304 SS Sample-D. The dashed lines indicate the depths at which the conductivity measurements were performed (from top to bottom: $Z = 0$ mm; $Z = -1$ mm; $Z = -2$ mm).

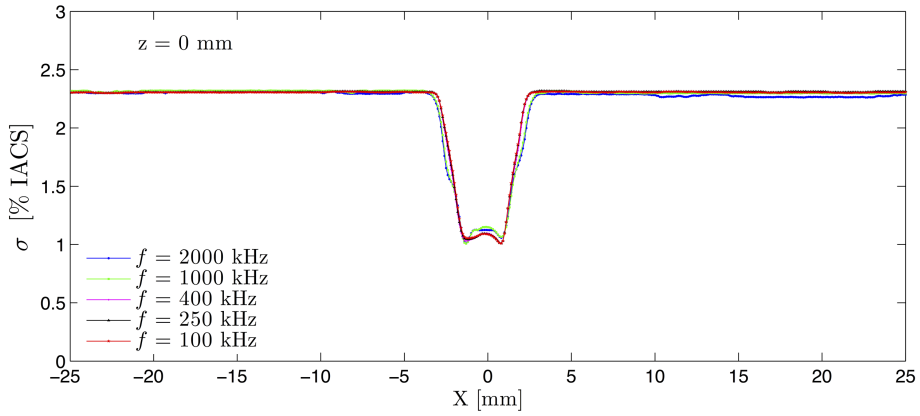

Figure 5.22 Electrical conductivity measurements performed at $Z = 0$ mm on AISI 304, Sample-E, welded by TIG. Welding parameters: V = 15 V; I = 80 V; v = 138 mm/min; H = 0.84 kJ.

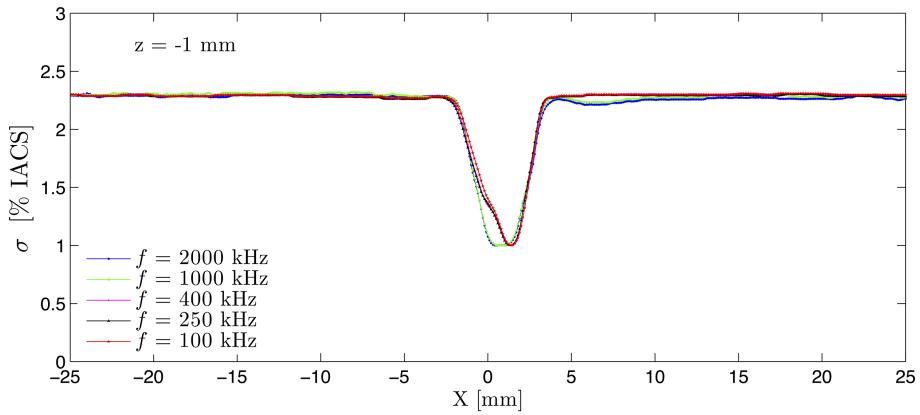

Figure 5.23 Electrical conductivity measurements performed at $Z = -1$ mm on AISI 304, Sample-E, welded by TIG. Welding parameters: V = 15 V; I = 80 V; v = 138 mm/min; H = 0.84 kJ.

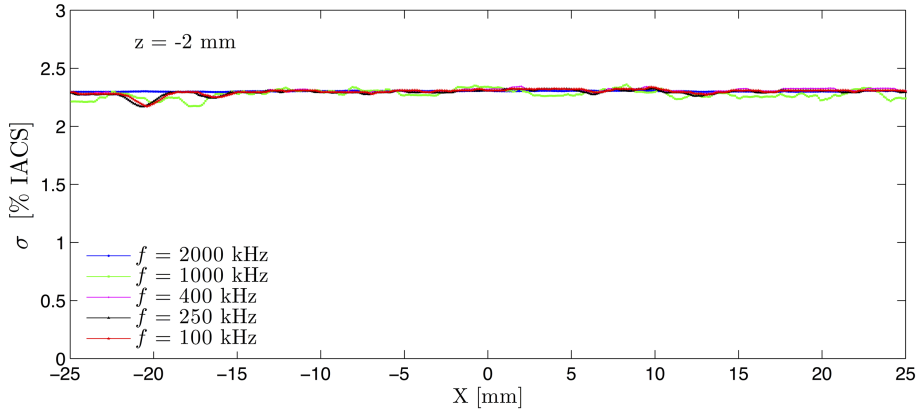

Figure 5.24 Electrical conductivity measurements performed at $Z = -2$ mm on AISI 304, Sample-E, welded by TIG. Welding parameters: V = 15 V; I = 80 V; v = 138 mm/min; H = 0.84 kJ.

As in the case of the previous, the hardness and conductivity profiles follow the same evolution. In figure 5.25 it can be seen that the hardness drops form about 200 HV0.5, in the base material, to 140 HV0.5 in the limits of the weld bead as a consequence of the larger grain size in the fusion zone (figure 5.20c). Inside the fusion zone, hardness increases from 140 HV0.5 to 180 HV0.5, possibly due to the increase in δ-ferrite content, which can also be the cause for the drop in conductivity, despite the increase in grain size present. A similar behavior can be observed in figure 5.26. However, as mentioned for the previous sample, the considerations mentioned should be confirmed by further investigation with advanced material characterization techniques.

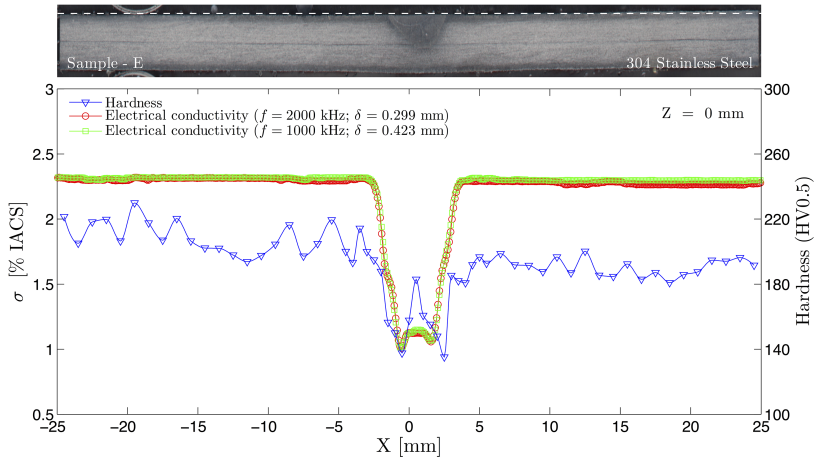

Figure 5.25 Electrical conductivity profile, performed at $Z = 0$ mm,and sub-surface hardness profile superposed with macrograph of AISI 304, Sample-E. The hardness and conductivity profiles display a direct relation. Welding parameters: V = 15 V; I = 80 V; v = 225 mm/min; H = 0.84 kJ.

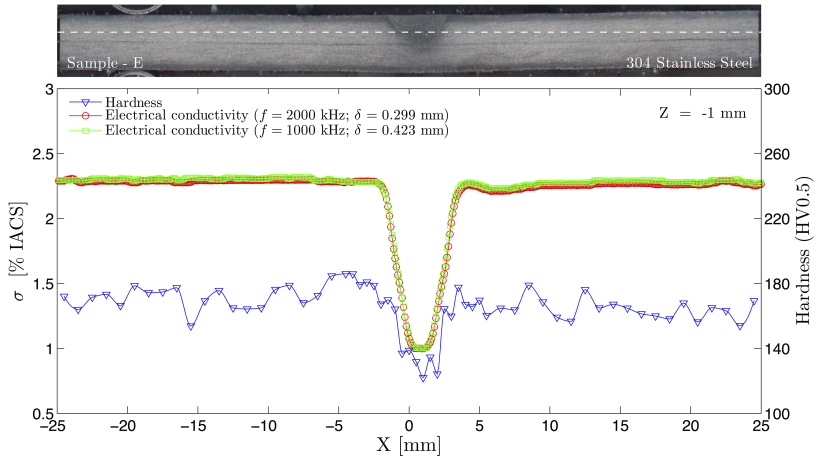

Figure 5.26 Electrical conductivity profile, performed at $Z = -1$ mm,and sub-surface hardness profile superposed with macrograph of AISI 304, Sample-E. The hardness and conductivity profiles display a direct relation. Welding parameters: V = 15 V; I = 80 V; v = 225 mm/min; H = 0.84 kJ.

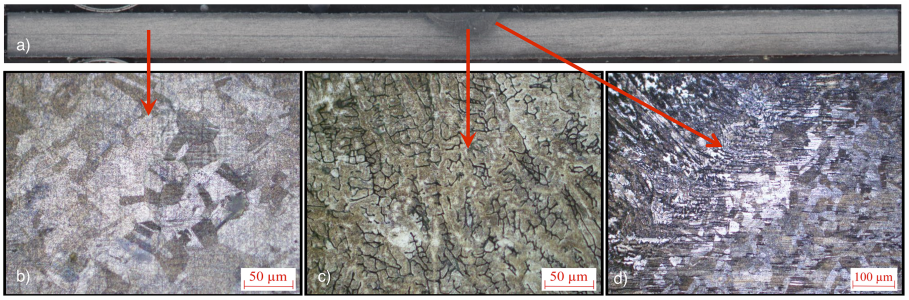

Figure 5.27 a) Macrograph of AISI 304, Sample-D. b) Micrograph of the base material with the typical microstructure of an austenitic stainless steel. c) Solidification structure in the fusion zone with the formation of δ-ferrite. d) Some grain coalescence in the HAZ.

5.4 Titanium Grade 5

For Ti Grade 5 samples the variation in electrical conductivity was seen only for the frequencies of 1000 and 2000 kHz. For this material, the currents at lower frequencies penetrate deeper into the material, beyond the depth of the bead, which can explain the lack of variation in conductivity.

The electrical conductivity profiles of the Friction Stir Processing (FSP) sample (Sample-O) performed at $Z = 0$ mm at 1000 and 2000 kHz, display a small, but relevant variation between $X = -10$ mm and $X = 10$ mm, in agreement to the processed bead (Figure 5.28), whereas for the other frequencies no variation exists. At $Z = -1$ mm (Figure 5.30) the curves for frequencies of 1000 and 2000 kHz display some variation in the position corresponding to that of the bead, however, they were not clear enough to be conclusive. For the other frequencies, no changes in conductivity were observed. As for the measurements performed at $Z = -2$ mm, a slight increase in conductivity was observed (Figure 5.31), which might be caused by the heat affected zone around the bead.

Figure 5.32 depicts the hardness and conductivity profiles superposed with the macrograph. Hardness in the base material is around 310 HV1 and drops to 300 HV1 in the HAZ due to grain growth in that zone. In the processed zone it increases to around 360 HV1 due to the destruction of the biphasic $\alpha + \beta$ microstructure of the base material and the increase in the amount of defects in the crystal structure that occur due to plastic deformation. The hardness and electrical conductivity profiles display an inverse relation in agreement with the behavior observed in a previous study of FPS aluminum alloys.



Figure 5.28 Macrograph of the FSP Ti Grade 5, Sample-O. The dashed lines indicate the depths at which the conductivity measurements were performed (from top to bottom: $Z = 0$ mm; $Z = -1$ mm; $Z = -2$ mm).

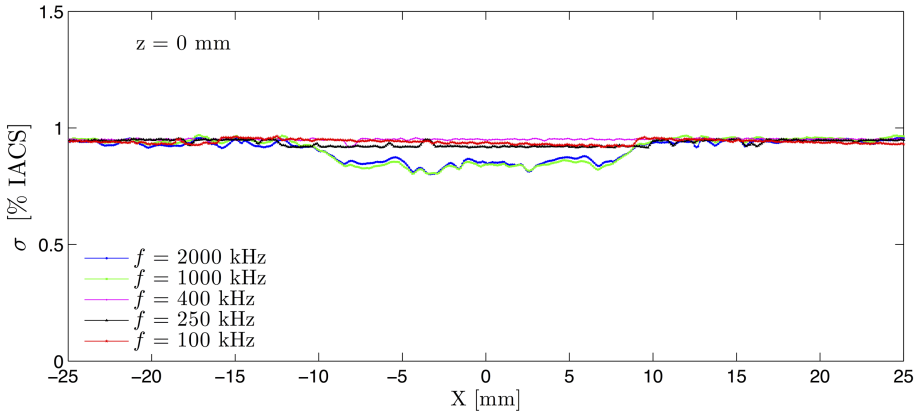

Figure 5.29 Electrical conductivity measurements performed at $Z = 0$ mm on FSP Ti Grade 5, Sample-O. Processing parameters: $\omega = 1120$ rpm; $v = 71$ mm/min; $\omega/v = 15.8$.

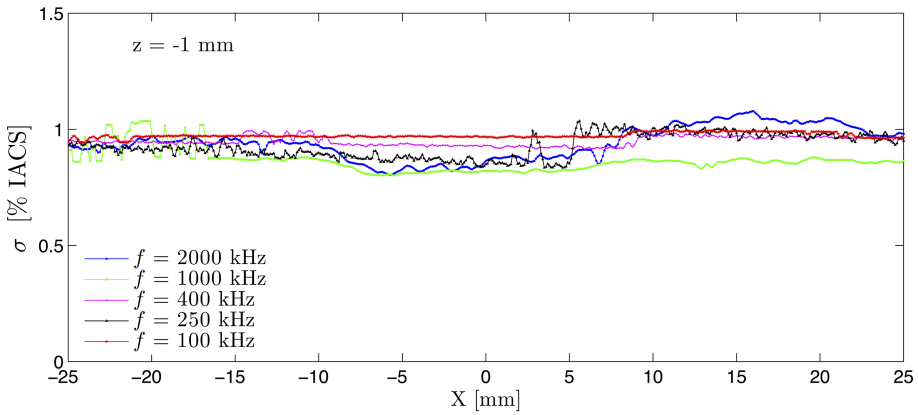

Figure 5.30 Electrical conductivity measurements performed at $Z = -1$ mm on FSP Ti Grade 5, Sample-O. Processing parameters: $\omega = 1120$ rpm; $v = 71$ mm/min; $\omega/v = 15.8$.

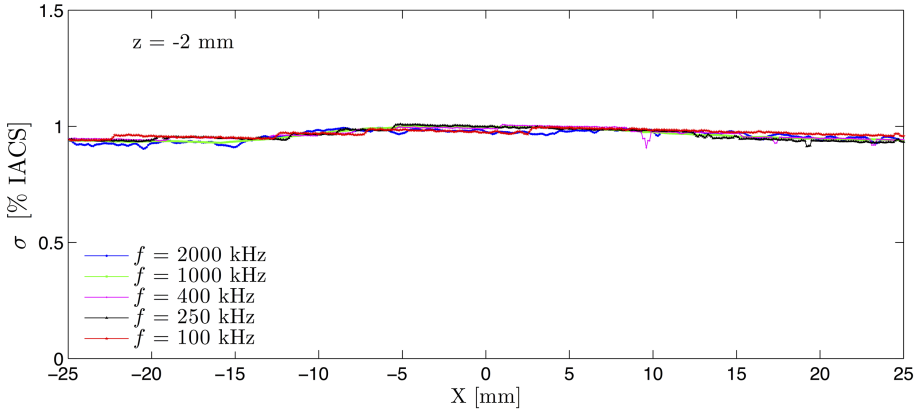

Figure 5.31 Electrical conductivity measurements performed at $Z = -2$ mm on FSP Ti Grade 5, Sample-O. Processing parameters: $\omega = 1120$ rpm; $v = 71$ mm/min; $\omega/v = 15.8$.

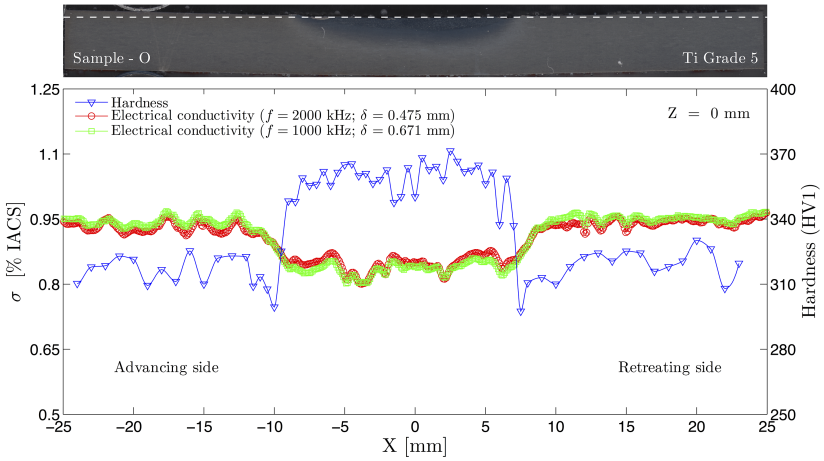

Figure 5.32 Electrical conductivity and hardness profiles, performed at $Z = 0$ mm, superposed with macrograph of sample FSP Ti Grade 5, Sample-O.

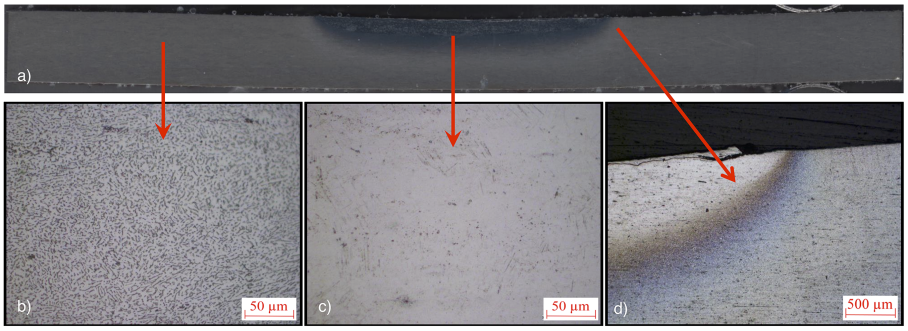

Figure 5.33 a) Macrograph of FSP Ti Grade 5, Sample-O. b) Micrograph of the base material. c) Processed zone with destruction of the original microstructure of the base material. d) Some grain growth in the HAZ.

As in the case of the previous sample, the measurements performed on the Ti Grade 5 welded by TIG, Sample-P, show the variation of electrical conductivity only at 1000 and 2000 kHz. The testing sweeps at these frequencies exhibit a good correlation with the macrograph of the sample (Figure 5.34) for the three depths. For the other frequencies, no variation was detected. In figures 5.35, 5.36 and 5.37 the 1000 and 2000 kHz frequencies show a decrease in conductivity in a position corresponding to that of the weld bead. The extension of that decrease closely matches the width of the bead at that depth. A decrease in conductivity is observed in the HAZ, followed by a slight increase and stabilization in the fusion zone.



Figure 5.34 Macrograph of the Ti Grade 5 Sample-P. The dashed lines indicate the depths at which the conductivity measurements were performed (from top to bottom: $Z = 0$ mm; $Z = -1$ mm; $Z = -2$ mm).

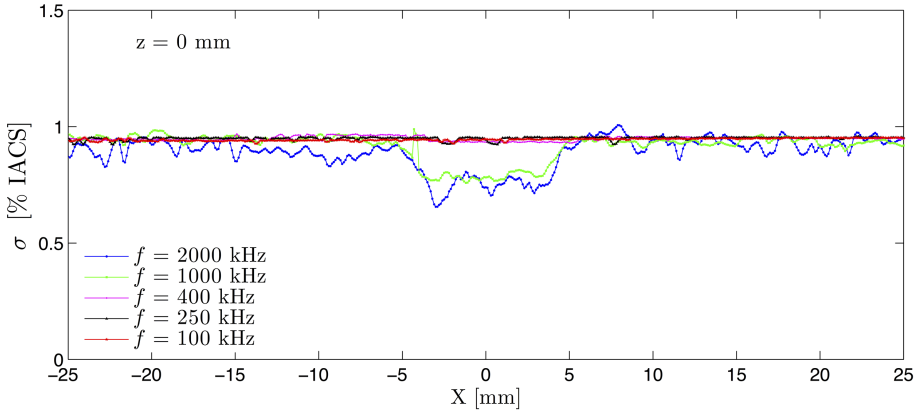

Figure 5.35 Electrical conductivity measurements performed at $Z = 0$ mm on Ti Grade 5, Sample-P, welded by TIG. H = 0.32 kJ.

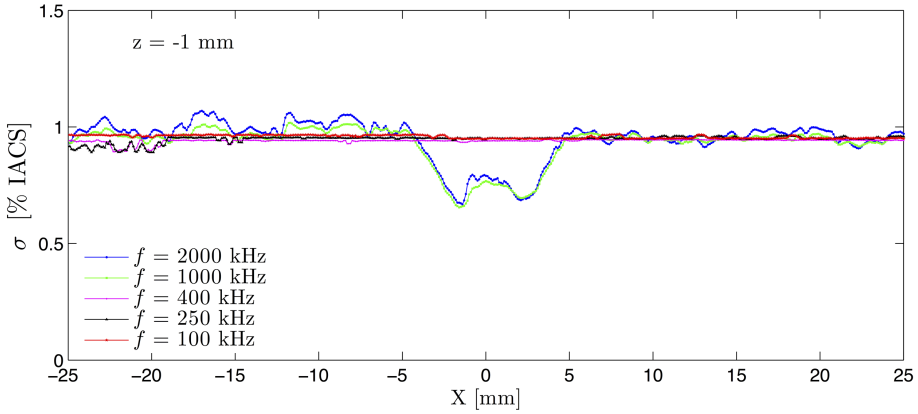

Figure 5.36 Electrical conductivity measurements performed at $Z = -1$ mm on Ti Grade 5, Sample-P, welded by TIG. H = 0.32 kJ.

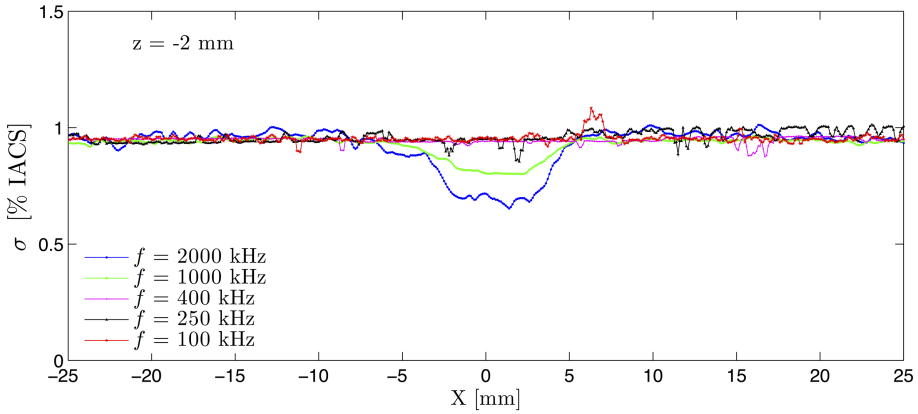

Figure 5.37 Electrical conductivity measurements performed at $Z = -2$ mm on Ti Grade 5, Sample-P, welded by TIG. H = 0.32 kJ.

Figures 5.38 and 5.39 show the electrical conductivity and hardness profiles, obtained at $Z = 0$ mm and $Z = -1$ mm, respectively, superposed with the macrograph of Sample-P. The hardness in the base material ranges from about 330 to 370 HV1, and stabilizes in the weld bead at around 350 HV1. The electrical conductivity displays a steadier behavior in the base material and a more pronounced variation, with a drop in the HAZ due to grain coalescence, followed by a slight increase in the fusion zone.

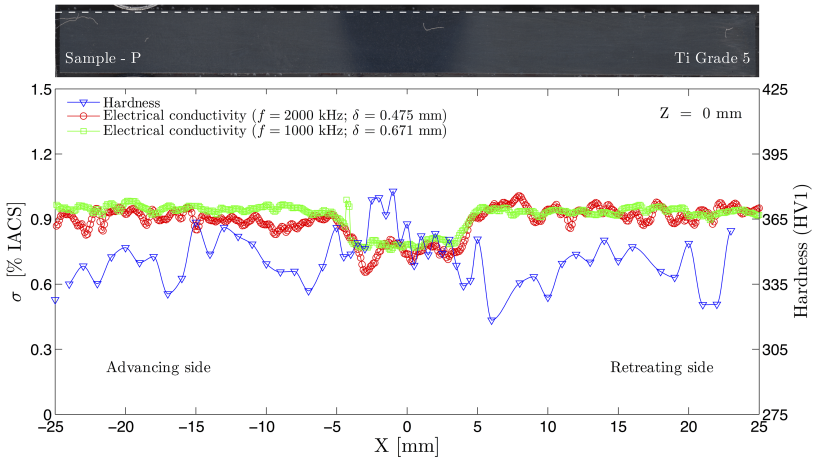

Figure 5.38 Electrical conductivity profile, performed at $Z = 0$ mm,and sub-surface hardness profile superposed with macrograph of Ti Grade 5, Sample-P, welded by TIG. The hardness and conductivity profiles display a direct.

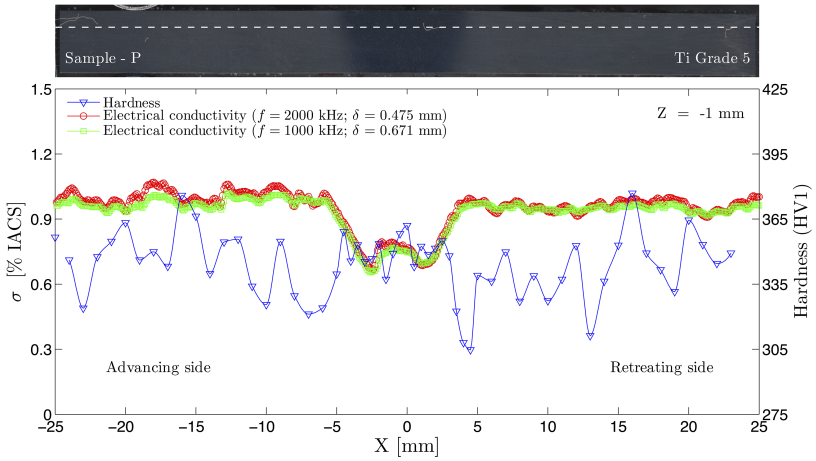

Figure 5.39 Electrical conductivity profile, performed at $Z = -1$ mm,and sub-surface hardness profile superposed with macrograph of Ti Grade 5, Sample-P, welded by TIG. The hardness and conductivity profiles display a direct.

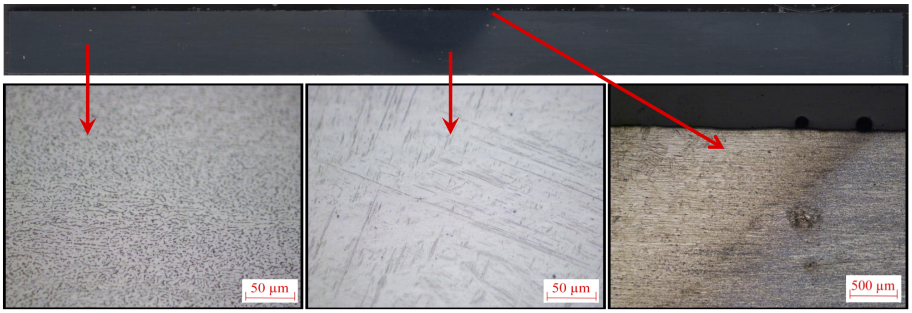

Figure 5.40 a) Macrograph of Ti Grade 5, Sample-P, welded by TIG. b) Micrograph of the base material. c) Microstructure of the fusion zone with an $\alpha + \beta$ solidification structure since cooling was to fast to allow the formation of martensite-like structures. d) Some grain growth and precipitate coalescence in the HAZ.

5.5 Titanium Grade 2

In the case of the Ti grade 2, Sample-R, welded by TIG the electrical conductivity variation with the distance to the weld bead is observed for $Z = 0$ mm but not for the other depths. The conductivity variation is smaller than for the Ti Grade 5 samples but, nevertheless, it replicates the structural features of the sample accurately.

For the $Z = 0$ mm depth (Figure 5.42), a good agreement between the conductivity profiles and the macrograph of the sample (Figure 5.41) can be observed for all the frequencies, except 2000 kHz. For the other frequencies, a good correlation between the weld bead and the behavior of the electrical conductivity curves can be seen. These curves follow each other closely, which indicates that the variations replicate the structural features of the material well.

Measurements performed at $Z = -1$ mm (Figure 5.43) and at $Z = -2$ mm (Figure 5.44) show no variation in conductivity for any of the frequencies tested.

Observing figure 5.46 it can be seen that, although the weld bead is evident, the change in microstructure in the fusion zone is not pronounced. This fact is reflected in the small magnitude of the change in conductivity observed for $Z = 0$ mm it lack of it at the other depths.



Figure 5.41 Macrograph of the TIG welded Ti Grade 2, Sample-R. The dashed lines indicate the depths at which the conductivity measurements were performed (from top to bottom: $Z = 0$ mm; $Z = -1$ mm; $Z = -2$ mm).

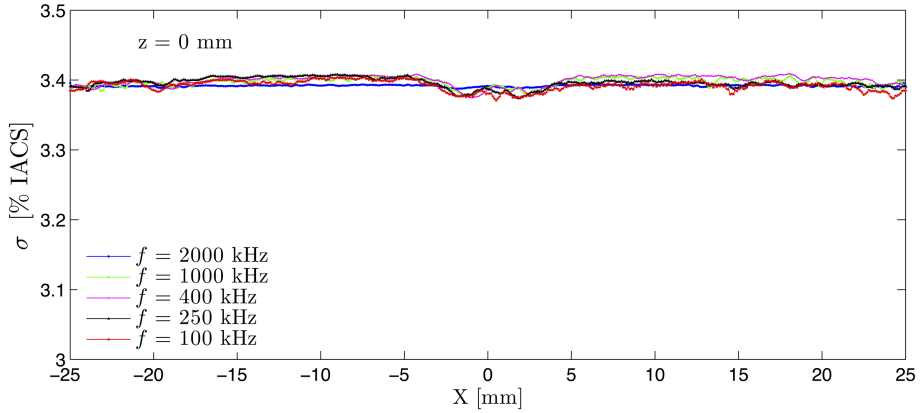

Figure 5.42 Electrical conductivity measurements performed on TIG welded Ti Grade 2, Sample-R at $Z = 0$ mm.

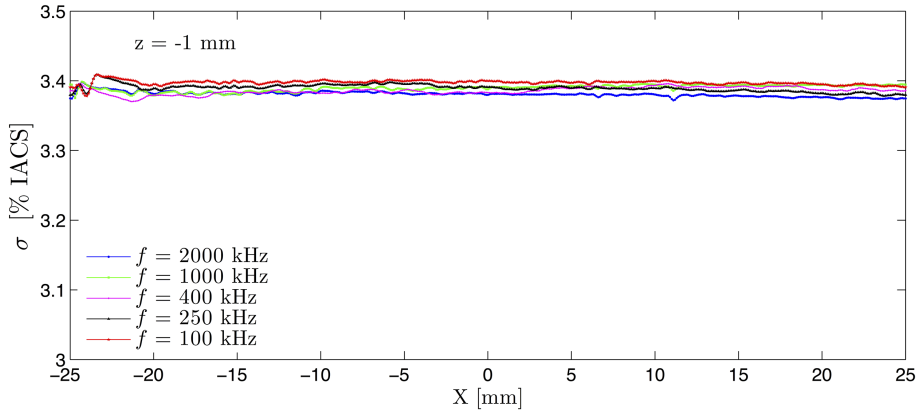

Figure 5.43 Electrical conductivity measurements performed on TIG welded Ti Grade 2, Sample-R at $Z = -1$ mm.

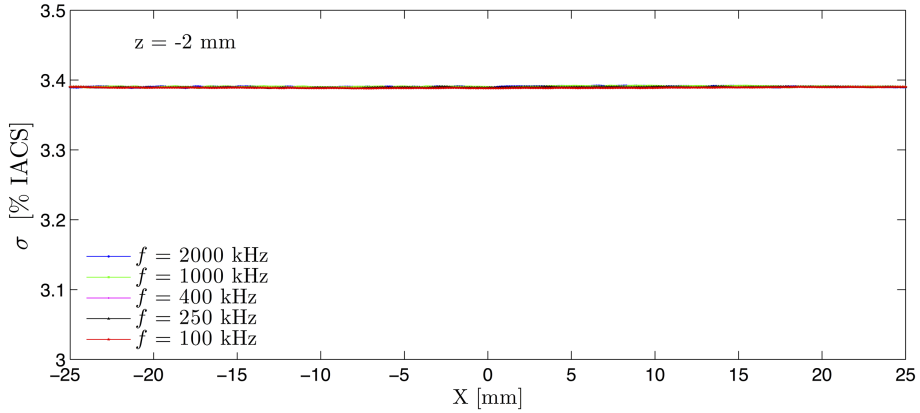

Figure 5.44 Electrical conductivity measurements performed on TIG welded Ti Grade 2, Sample-R at $Z = -2$ mm.

It should be noticed that Ti Grade 2 has a higher σ than Grade 5 since it is an α Ti, while Grade 5 is biphasic. Similarly, Grade 2 has a lower hardness value than Grade 5. The hardness and electrical conductivity profiles show an inverse relation coherent with the findings for Al alloys.

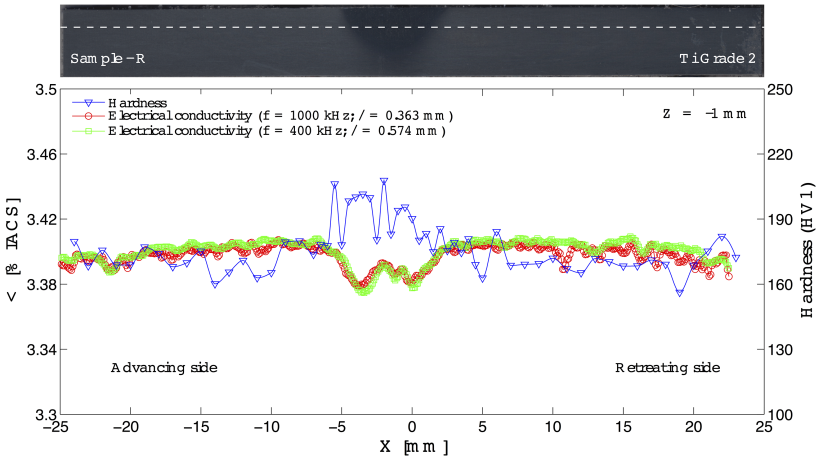

Figure 5.45 Electrical conductivity and hardness profiles, performed at $Z = 0$ mm, superposed with macrograph of sample TIG welded Ti Grade 2, Sample-R.

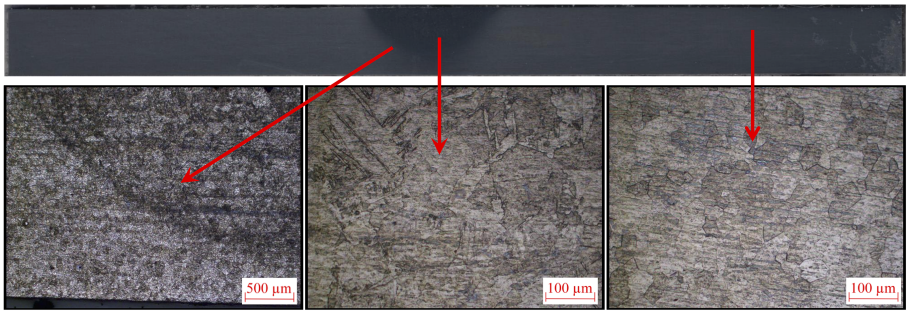

Figure 5.46 a) Macrograph of Ti Grade 2 (Sample-R). b) Detail of the frontier between the base material and the fusion zone. c) Micrograph of the fusion zone. d) Micrograph of the base material.

5.6 AZ31 Magnesium Alloy

For the AZ31 magnesium alloy Sample-J the electrical conductivity measurements show the electrical conductivity variation only for the surface depth ($Z = 0$ mm) test sweeps.

At $Z = -1$ mm (Figure 5.49) and $Z = -2$ mm (Figure 5.50) no relevant variation in conductivity exist for any of the frequencies tested. However, it can be seen that the measurements at all frequencies, except 1000 kHz, match each other closely, which indicates that their variations represent the different zones of the material.

The tests for this material were continued with 400 and 250 kHz frequencies, which produced the best results.



Figure 5.47 Macrograph of the AZ31 Sample-J. The dashed lines indicate the depths at which the conductivity measurements were performed (from top to bottom: $Z = 0$ mm; $Z = -1$ mm; $Z = -2$ mm).

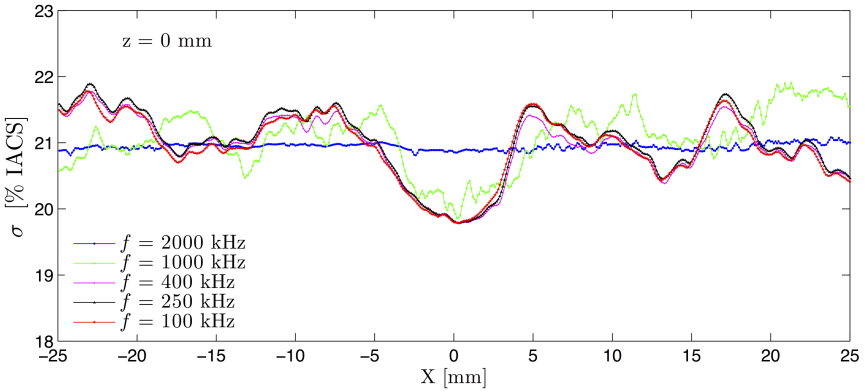

Figure 5.48 Electrical conductivity measurements performed on AZ31, Sample-J, processed in the cold condition at $Z = 0$ mm.

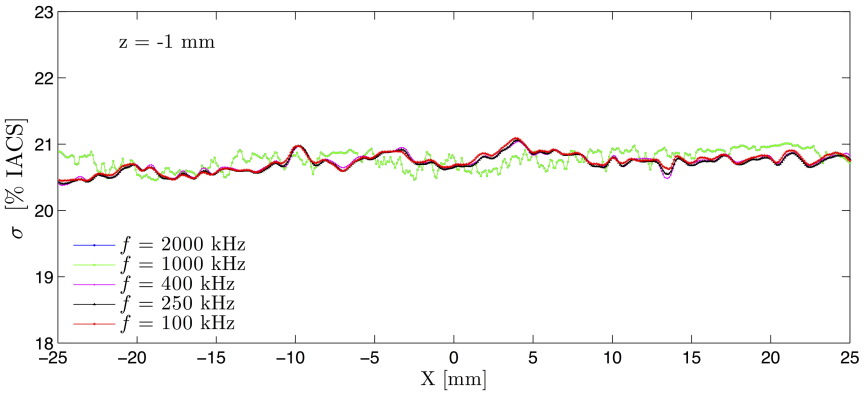

Figure 5.49 Electrical conductivity measurements performed on AZ31, Sample-J, processed in the cold condition at $Z = -1$ mm.

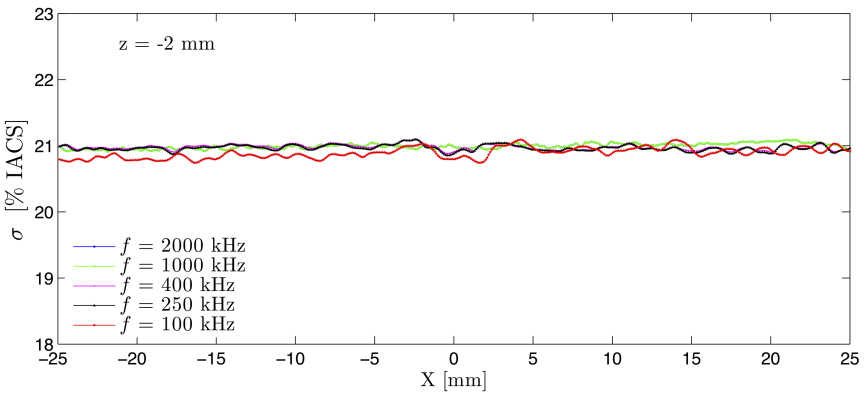

Figure 5.50 Electrical conductivity measurements performed on AZ31, Sample-J, processed in the cold condition at $Z = -2$ mm.

Figure 5.51 displays the hardness and electrical conductivity profiles, produced at $Z = 0$ mm, superposed with the macrograph of the sample. The hardness of the base material varies from about 65 to around 80 HV0.3. In the processed zone a stabilization at close to 70 HV0.3 is caused by the homogenization of the microstructure, as a consequence of processing. The severe plastic deformation also refines the microstructure of the material (Figure 5.52), causing the electrical conductivity to drop from between 21 to 22 %IACS in the base material to a about 19.5 %IACS in the stirred zone. This behavior, like in the case of the AISI 304 stainless steel, is not in agreement with the findings for Al alloys reported in [42, 43] and requires further investigation.

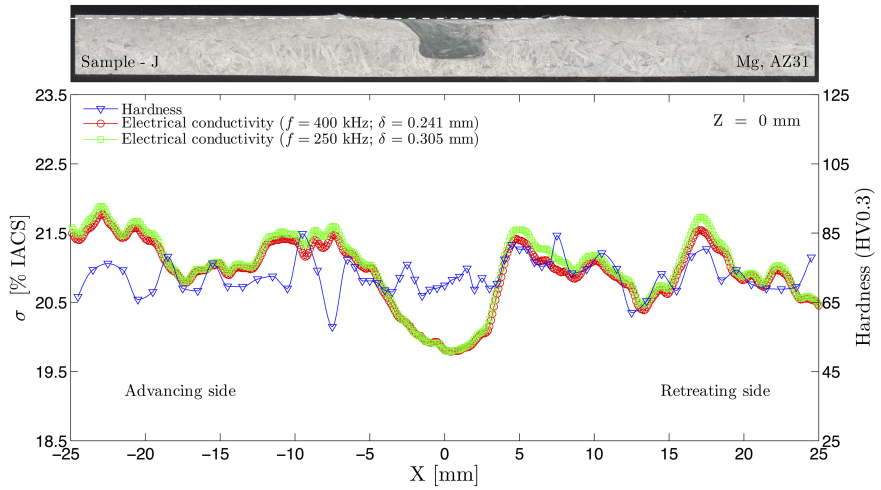

Figure 5.51 Electrical conductivity and hardness profiles, performed at $Z = 0$ mm, superposed with macrograph of the FSP AZ31 processed in the cold condition, Sample-J.

In this particular sample, the electrical conductivity reproduces the processed bead profile more closely than hardness does. The AZ31 plate was in the cast and annealed condition and even in base material there are significant variations in hardness while the σ is smooth.

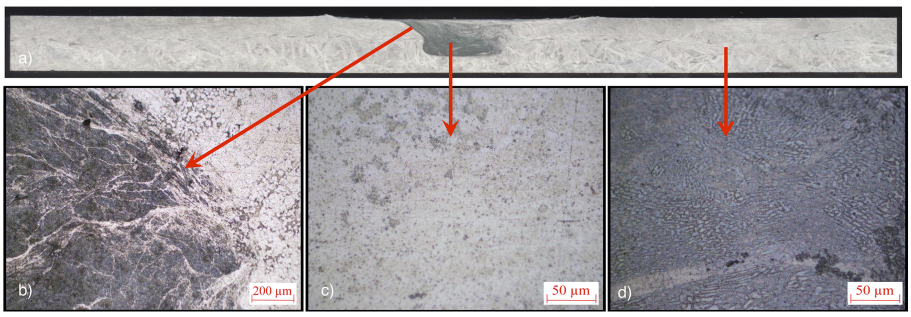

Figure 5.52 a) Macrograph of AZ31 processed in the cold condition, Sample-J. b) Detail of the difference between the microstructures of the base material and the stirred zone. c) Fine-grained stirred zone. d) Base material with a typical solidification structure of a cast AZ31.

The electrical conductivity measurements for AZ31 magnesium alloy processed in

the hot condition, Sample-K, display the variation of electrical conductivity along the distance to the processed bead at all the depths tested. As with Sample-J, the frequencies that represent the microstructural features of the material more accurately are 100, 250 and 400 kHz.

Measurements performed at $Z = 0$ mm depth (Figure 5.54) show almost no variation of electrical conductivity. Only a small decrease was observed around $X = -8$ mm followed by a gradual increase, to the conductivity values of the base material, until about $X = 8$ mm. These positions correspond to those of the processed bead, and, therefore, the variation in σ can be caused by changes in microstructure in the processed zone.

At $Z = -1$ mm (Figure 5.55) the electrical conductivity variation measured with the 100, 250 and 400 kHz displays a good correlation with the macrograph of figure 5.53. The curves at these frequencies show the decrease at about $X = -8$ mm followed by a stabilization until $X = 8$ mm. This behavior is in agreement with the grain refinement and homogenization, typical of FSP.

For $Z = -2$ mm (Figure 5.56) σ also varies with the distance to the bead, for the all frequencies except 2000 kHz. The 100, 250 and 400 kHz curves show a fluctuation in conductivity in the base material and a decrease in the processed zone that correlates well with the features observed in the macrograph.

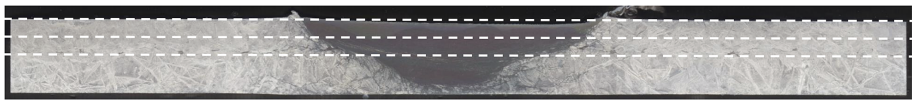

Figure 5.53 Macrograph of the AZ31 processed in the hot condition Sample-K. The dashed lines indicate the depths at which the conductivity measurements were performed (from top to bottom: $Z = 0$ mm; $Z = -1$ mm; $Z = -2$ mm).

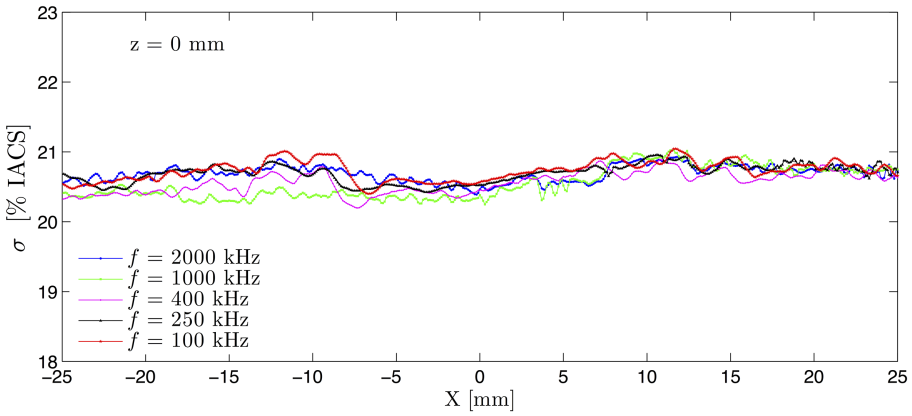

Figure 5.54 Electrical conductivity measurements performed on AZ31, Sample-K, processed in the hot condition at $Z = 0$ mm.

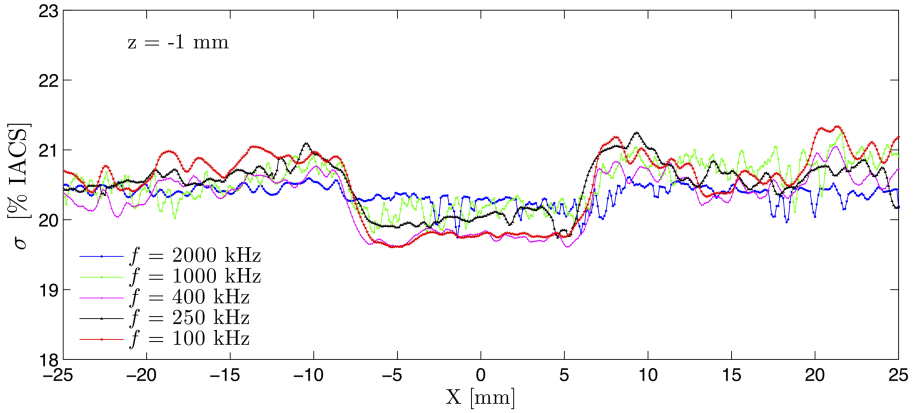

Figure 5.55 Electrical conductivity measurements performed on AZ31, Sample-K, processed in the hot condition at $Z = -1$ mm.

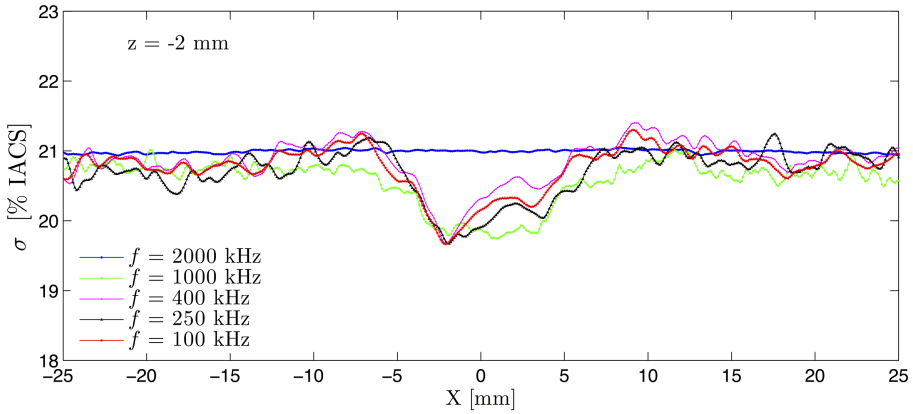

Figure 5.56 Electrical conductivity measurements performed on AZ31, Sample-K, processed in the hot condition at $Z = -2$ mm.

The tests were continued with 250 and 100 kHz.

In figures 5.57 and 5.58, which depicts the hardness and electrical conductivity profiles for $Z = 0$ mm and $Z = -1$ mm, respectively, superposed with the macrograph of the Sample-K, it can be seen that there is a drop in conductivity that correlates nicely with the refined grain structure in the processed zone (Figure 5.59c). Hardness also drops slightly in the same zone, which is in contradiction to the the behavior that was reported in [42, 43] for Al alloys. Since the base material is a cast and annealed AZ31 alloy with a typical solidification structure (5.59b), β-Mg precipitates, which provide precipitation strengthening, might be destroyed and dissolved in the stir zone causing the drop in hardness. However, this hypothesis requires confirmation and further research by advanced characterization techniques should be conducted.

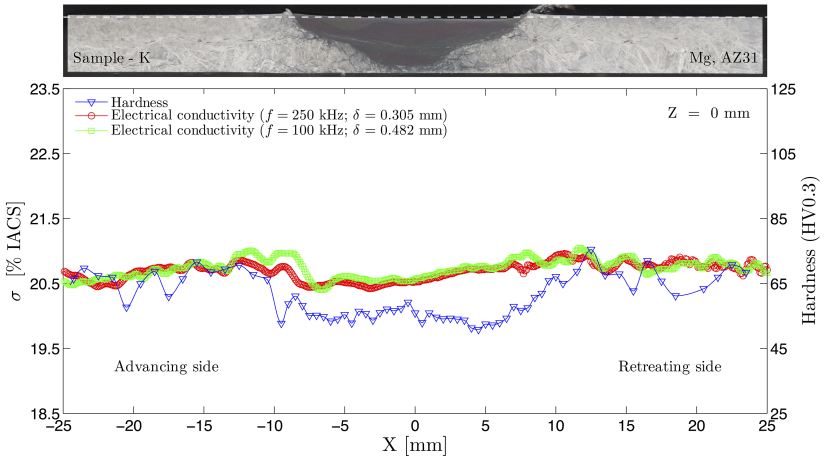

Figure 5.57 Electrical conductivity and hardness profiles, performed at $Z = 0$ mm, superposed with macrograph of the FSP AZ31 processed in the hot condition, Sample-K.

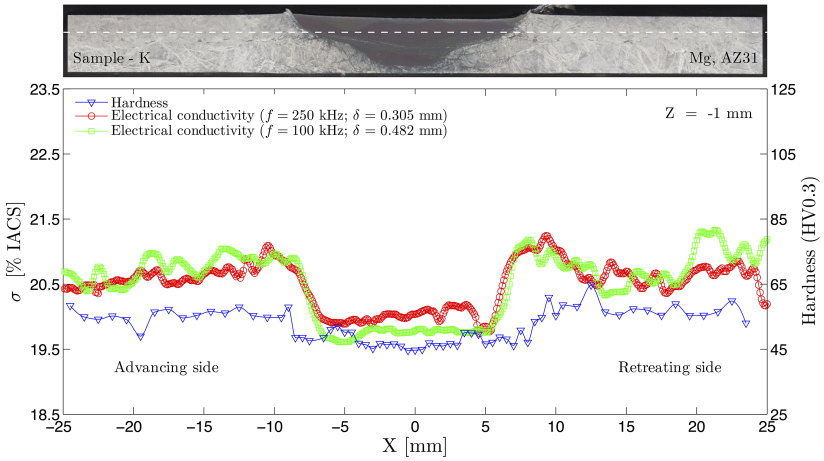

Figure 5.58 Electrical conductivity and hardness profiles, performed at $Z = -1$ mm, superposed with macrograph of the FSP AZ31 processed in the hot condition, Sample-K.

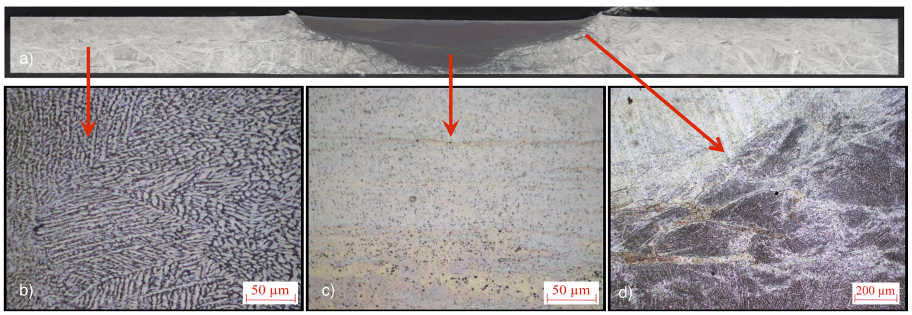

Figure 5.59 a) Macrograph of AZ31 processed in the hot condition, Sample-K. b) Detail of the difference between the microstructures of the base material and the stirred zone. c) Fine-grained stirred zone. d) Base material with a typical solidification structure of a cast AZ31.

5.7 Lead

For the lead processed in the hot condition, the electrical conductivity only varies for the $Z = -1$ mm and $Z = -2$ mm depths.

At $Z = 0$ mm (Figure 5.61) there is no change in the conductivity with the distance to the bead. Since lead is a very soft and ductile material and recrystallizes at room temperature, processing does not produce any effect on grain size that can alter the conductivity. Additionally it has a conductivity where the variations in grain size do not significantly modify the local electrical conductivity. Measurements at $Z = -1$ mm (Figure 5.62) and $Z = -2$ mm (Figure 5.63) show that there is a drop of conductivity in the region of the bead. Observing the macrograph of the sample (Figure 5.60), it can be seen that this behavior coincides with the presence of impurities.

The tests for this material were continued with 400 and 100 kHz frequencies.

In figure 5.64 the hardness and electrical conductivity profiles, produced at $Z = -1$ mm superposed with the macrograph of the sample, are presented. The hardness in the base material is about 5 HV0.025 and increases to about 7 HV0.025 in the processed zone. Although there seems to be no grain refinement due to processing in this zone there is an accumulation of silica and other impurities (Figure 5.65) that can account for the increase in hardness and the decrease in conductivity.



Figure 5.60 Macrograph of the FSP lead, Sample-L, processed in the hot condition. The dashed lines indicate the depths at which the conductivity measurements were performed (from top to bottom: $Z = 0$ mm; $Z = -1$ mm; $Z = -2$ mm).

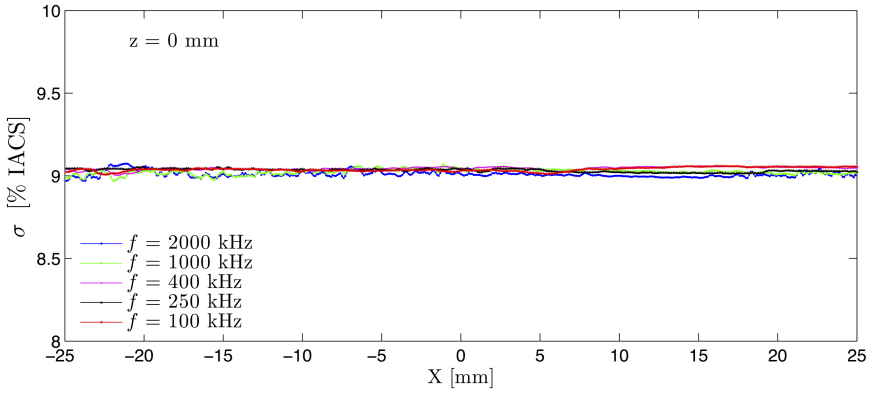

Figure 5.61 Electrical conductivity measurements performed on FSP lead, Sample-L, processed in the hot condition at $Z = 0$ mm.

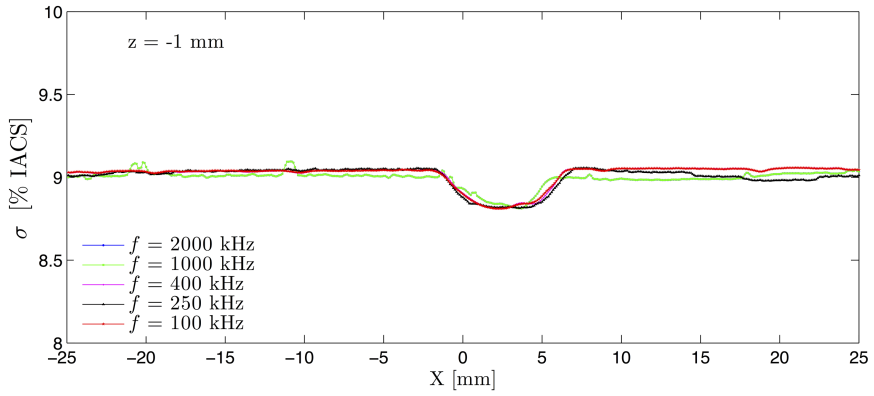

Figure 5.62 Electrical conductivity measurements performed on FSP lead, Sample-L, processed in the hot condition at $Z = -1$ mm.

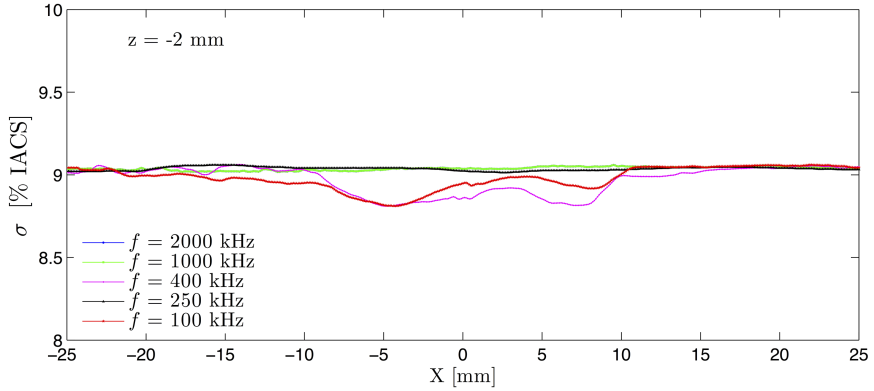

Figure 5.63 Electrical conductivity measurements performed on FSP lead, Sample-L, processed in the hot condition at $Z = -2$ mm.

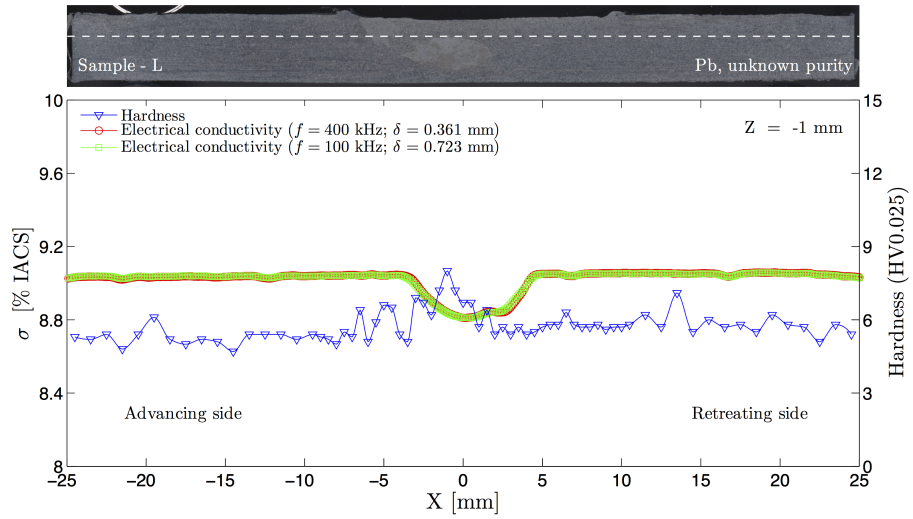

Figure 5.64 Electrical conductivity and hardness profiles, performed at $Z = -1$ mm, superposed with macrograph of FSP lead, Sample-L, processed in the hot condition.

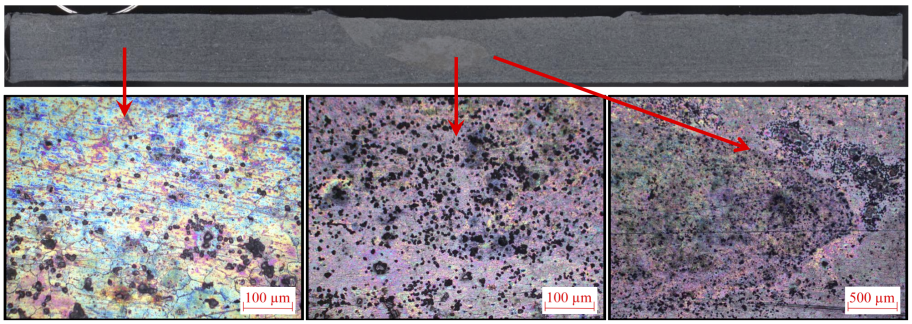

Figure 5.65 a) Macrograph of FSP lead, Sample-L, processed in the hot condition. b) Micrograph of the base material. c) Micrograpah of the stirred zone where an accumulation of impurities can be seen. d) Detail of the accumulation of impurities in the stirred zone.

The lead processed in the cold condition exhibits no variation of electrical conductivity at any depth (Figures 5.67, 5.68 and 5.69). Observing the macrograph of the sample (Figure 5.66) there seems to be no significant alteration in the microstructure of the material, which is in agreement to the lack of change in conductivity.



Figure 5.66 Macrograph of the AZ31 Sample-N. The dashed lines indicate the depths at which the conductivity measurements were performed (from top to bottom: $Z = 0$ mm; $Z = -1$ mm; $Z = -2$ mm).

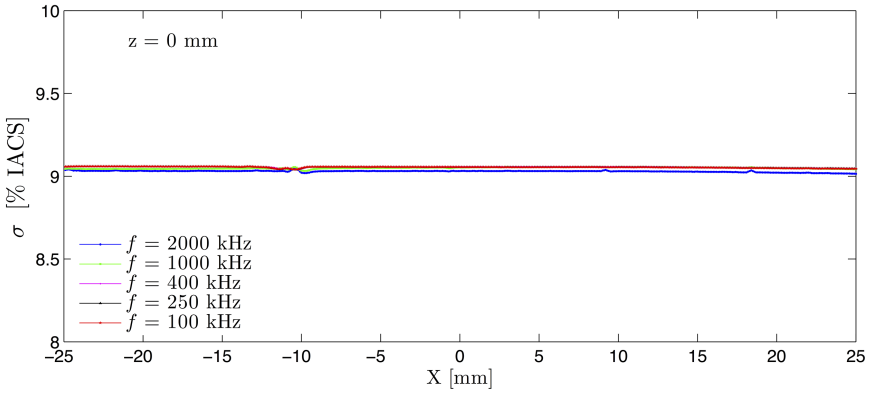

Figure 5.67 Electrical conductivity measurements performed on FSP lead processed in the cold condition, Sample-N, at $Z = 0$ mm.

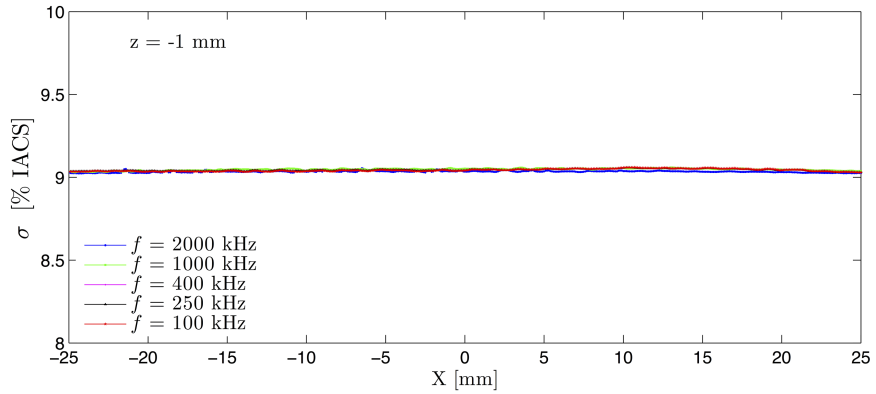

Figure 5.68 Electrical conductivity measurements performed on FSP lead processed in the cold condition, Sample-N, at $Z = -1$ mm.

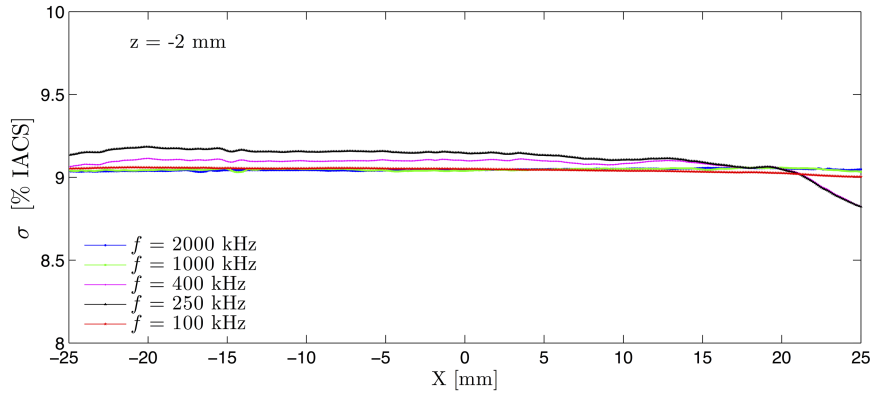

Figure 5.69 Electrical conductivity measurements performed on FSP lead processed in the cold condition, Sample-N, at $Z = -2$ mm.

The tests were continued with 250 and 100 kHz.

In figure 5.70, in which the hardness and electrical conductivity profiles for $Z = -1$ mm superposed with the macrograph of Sample-N, it can be seen that there is no change in hardness with distance to the weld bead, which correlates nicely with the absence of conductivity variation. This is explained since microstrucutre of lead is not sensitive to processing and, so, grain size does not seem to vary in the stirred zone (Figure 5.71).

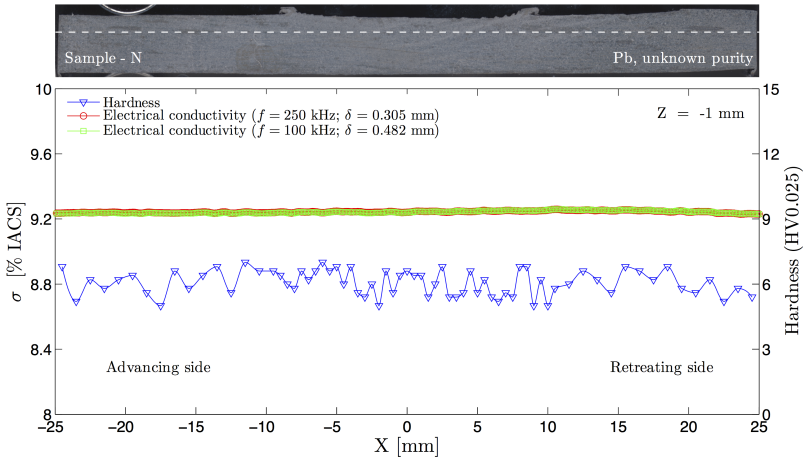

Figure 5.70 Electrical conductivity and hardness profiles, performed at $Z = -1$ mm, superposed with macrograph of sample FSP lead, processed in the cold condition, Sample-N.

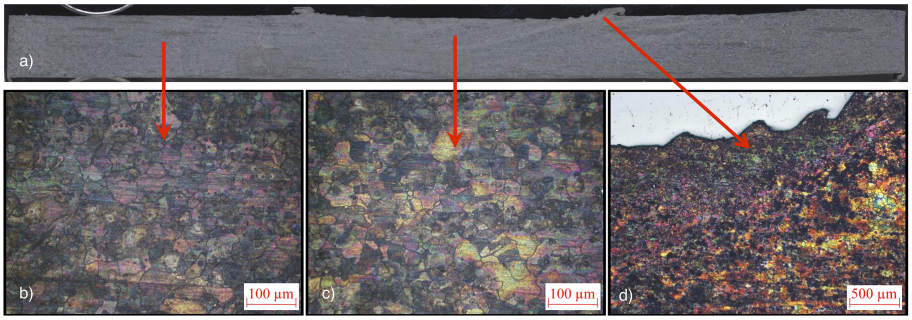

Figure 5.71 a) Macrograph of FSP lead, Sample-N, processed in the cold condition. b) Micrograph of the base material. c) Micrograpah of the stirred with no significant changes in microstructure. d) Detail of the transition between the base material and stirred zone, near the surface of the sample.

5.8 Copper

In the case of the friction stir processed copper, Sample-H, a small increase in the electrical conductivity in the bead is observed for $Z = 0$ mm but not for the other depths.

For the $Z = 0$ mm depth (Figure 5.73), the 400, 250 and 100 kHz frequencies display a slight increase in the region corresponding to the processed bead. Measurements performed at $Z = -1$ mm (Figure 5.74) and at $Z = -2$ mm (Figure 5.75) show no variation in σ for any of the frequencies tested. Since copper is a highly conductive material, the changes in its microstructure due to processing are not relevant enough to affect conductivity.

Observing the conductivity and hardness profiles superposed with the macrograph of the sample in figure 5.77 it can be seen that the hardness decreased in the processed zone, corresponding to the tool shoulder. Inversely, conductivity displays slight increase in a position that corresponds to the tool probe. These behaviors occur despite the grain

refinement caused by processing, which is evident when comparing the microstructure of the base material to that of the stirred zone (Figure 5.77). Copper is so conductive that Friction Stir Processing does not change its conductivity significantly.



Figure 5.72 Macrograph of the FSP copper Sample-H. The dashed lines indicate the depths at which the conductivity measurements were performed (from top to bottom: $Z = 0$ mm; $Z = -1$ mm; $Z = -2$ mm).

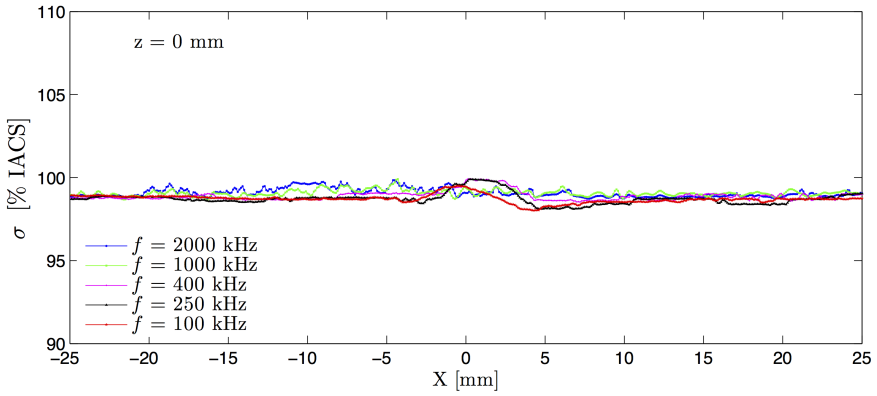

Figure 5.73 Electrical conductivity measurements performed on FSP copper, Sample-H, at $Z = 0$ mm.

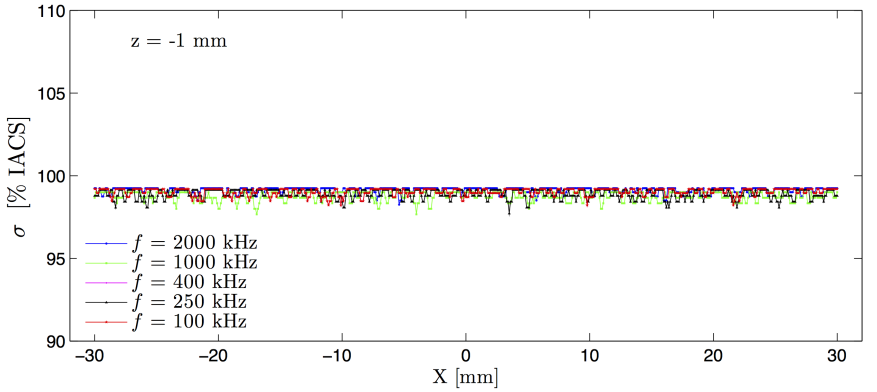

Figure 5.74 Electrical conductivity measurements performed on FSP copper, Sample-H, at $Z = -1$ mm.

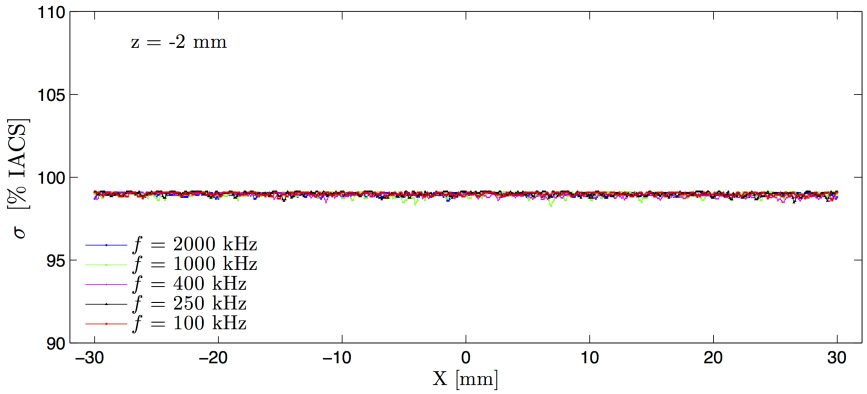

Figure 5.75 Electrical conductivity measurements performed on FSP copper, Sample-H, at $Z = -2$ mm.

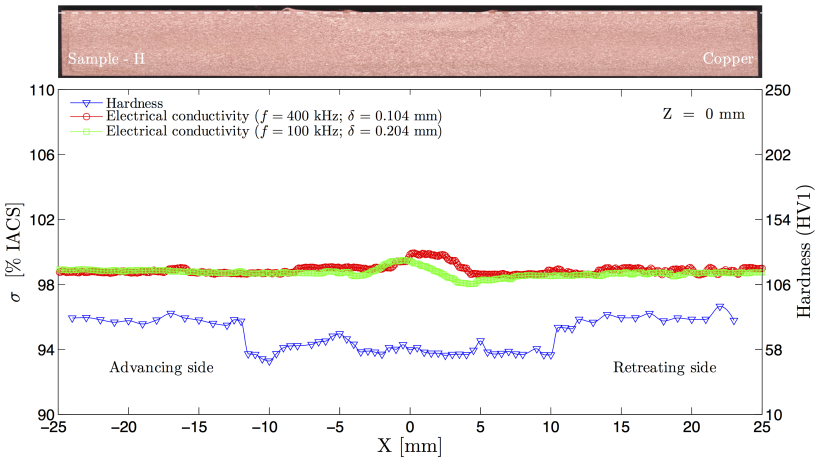

Figure 5.76 Electrical conductivity and hardness profiles, performed at $Z = 0$ mm, superposed with macrograph of sample Sample-H.

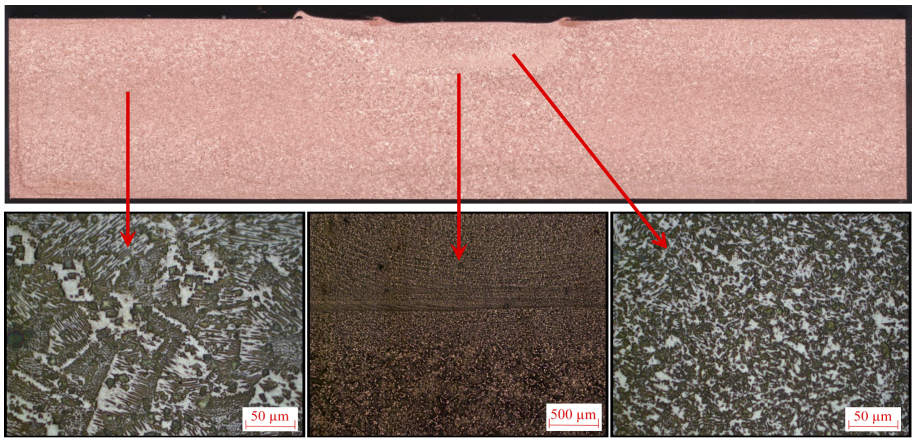

Figure 5.77 a) Macrograph of FSP copper, Sample-H. b) Micrograph of the base material. c) Detail of the difference between the stirred zone and the base material. d) Microstructure of the fine-grained stirred zone.

5.9 Conclusions

The results show that, for the materials under study, welding or processing produces changes in the microstructure of materials that can be detected by measuring the electrical conductivity variation with the distance to the fusion or stirred zone. For the AISI 1020, Ti Grade 5, Ti Grade 2, lead and copper, conductivity displays an inverse relation to hardness, in agreement with the findings of Santos *et al* [42, 43] for aluminum alloys. For the AISI 304 and the cast and annealed AZ31 this relation is direct and should be investigated further using advanced materials characterization techniques.

Comparing the hardness and σ profiles and observing the micrographs of the materials, it can be seen that the information provided by the hardness and conductivity tests is complementary. In fact, the electrical conductivity is more sensitive to changes in grain size, whereas hardness varies mostly due to precipitates.

Figure 5.78 compares the conductivity variation of the materials under study. It can be seen that the greatest variation occurred in the MAG welded AISI 1020, with a variation of almost 4 %IACS while for lead and Ti Grade 2 it is almost unnoticeable since it was only 0.2 %IACS and 0.02 %IACS, respectively.

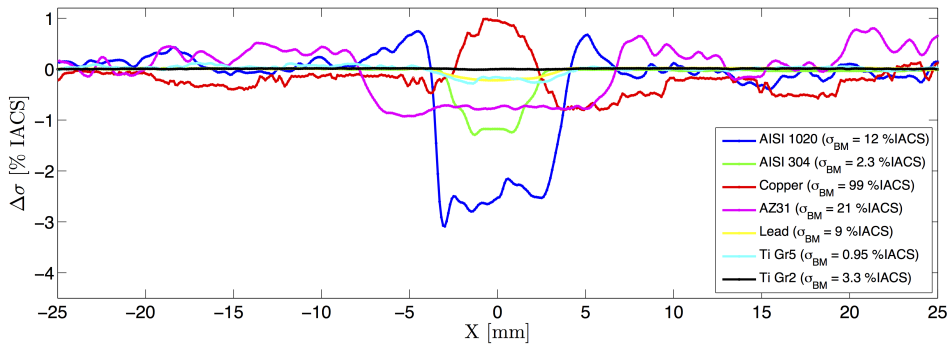

Figure 5.78 Comparison of the variation of electrical conductivity with distance to the weld and processed beads for the materials under study.

Although most of these variations are small (< 1 %IACS), they can be significant, compared to the average conductivity of the base material. 1 %IACS variation is not much for a material as copper, or for the cast and annealed AZ31 which has an average conductivity of 19 %IACS. In fact, the variation of σ in the base material of this magnesium alloy was between 0.5 and 1 %IACS while in the processed zone it was almost 2 %IACS. However, for a material with a low conductivity like the AISI 304, a drop of 1 %IACS in the fusion zone represents a variation of over 40 %, relative to its average conductivity in the base material (Figure 5.79).

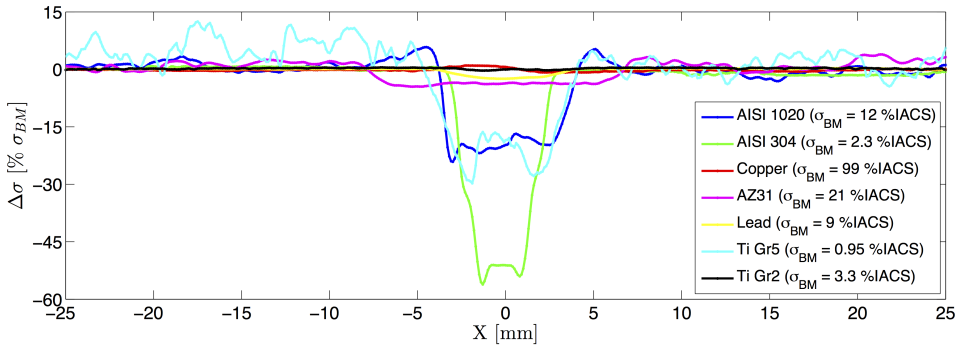

Figure 5.79 Comparison of the percentual variation of the electrical conductivity with the distance to the weld and processed beads for the materials under study.

Compared to the hardness profiles of all the materials under study, except copper, the electrical conductivity profile depicts the different zones of the welded or processed materials more accurately.

6

Final conclusions

This chapter presents the conclusions resulting from the investigation conducted as well as suggestions for future work emerging from this study.

The results of the tests performed on the materials under study (AISI 1020, AISI 304, Ti Grade 5, Ti Grade 2, AZ31, lead and copper) originated the following conclusions:

- A prototype for four-point potential drop testing electrical conductivity measurements was designed, built and successfully tested, providing an alternative to eddy currents for electrical conductivity based materials characterization;
- The variation of the σ with the distance to the welded or processed beads was verified for all the materials except for copper;
- The δ varies with the material and with the test f, the latter being a fundamental parameter for a correct evaluation of the electrical conductivity and interpretation of the results of eddy currents testing. For materials with a high μ_0 and/or high electrical conductivity, δ is small and the currents concentrate near the surface of the material with little influence from the test f. For materials with low μ_0 and σ, the frequency has a important influence;
- For AISI 1020 and copper, the frequency has little influence on the results. For AISI 304, Ti Grade 5 and Ti Grade 2 frequencies of 1000 and 2000 kHz provided the best results whereas for AZ31 and lead these were obtained at 100, 200 and 2000 kHz;
- A variation of 4 %IACS, corresponding to 20% of the average conductivity of the base material, was observed in AISI 1020 welded by MAG;
- For AISI 304 welded by Tungsten Inhert Gas (TIG) $\Delta\sigma$ was about 1.3 %IACS, corresponding to a 57% of the average electrical conductivity of the material;
- In the case of friction stir processed and TIG welded Ti Grade 5, σ variation could not be accurately quantified due to difficulties in the calibration for those materials. However, qualitatively, the electrical conductivity variation represented the processed and welded zones accurately;
- The variation of electrical conductivity in the TIG welded Ti Grade 2 was only 0.04%IACS, corresponding to about 1% of the average conductivity of the base material. Nevertheless, it represented the microstructural features of the different zones accurately, even more than hardness;
- The effects of FSP on the electrical conductivity of lead were small, due to the fact that this material recrystallizes at room temperature, and it was unclear whether they were due to changes in microstructure or presence of impurities. This should be investigated further using advanced materials characterization techniques;
- For copper, processing did not have a significant effect on conductivity since this material is a very good electrical conductor;
- Comparing the hardness and σ profiles and observing the micrographs of the materials, it can be seen that the information provided by the hardness and conductivity tests is complementary. In fact, the electrical conductivity is more sensitive to changes in grain size, whereas hardness varies mostly due to precipitates;
- An inverse relation between hardness and conductivity was observed for AISI 1020, Ti Grade 5, Ti Grade 2, lead and copper in accordance with previous studies [42, 43];

- For AISI 304 and AZ31 hardness and electrical conductivity have a direct relation which needs further material research.

The results show that the electrical conductivity fields of the welded ferrous materials that were studied are very accurate in representing their microstructural features. This presents an opportunity for the development of dedicated, non-destructive, electrical current based characterization techniques that should explored.

6.1 Future work suggestions

This thesis was a first approach to the use of electrical current based materials characterization techniques to the materials that were investigated. Ultimately, it raised more questions which require further research.

The direct relation between the electrical conductivity and hardness profiles exhibited by the AISI 304 and the AZ31 magnesium alloy contradicts the observations of previous studies and should be investigated further, using advanced material characterization techniques.

Bibliography

[1] W. Thomas. "Friction Stir Butt Welding". Pat. 1995.

[2] Andrew L. Biro, Brendan F. Chenelle, and Diana A. Lados. "Processing, Microstructure, and Residual Stress Effects on Strength and Fatigue Crack Growth Properties in Friction Stir Welding: A Review". In: *Metallurgical and Materials Transactions B* 43.6 (Sept. 2012), pp. 1622–1637. ISSN: 1073-5615, 1543-1916.

[3] R Nandan, T Debroy, and H Bhadeshia. "Recent advances in friction-stir welding – Process, weldment structure and properties". In: *Progress in Materials Science* 53.6 (Aug. 2008), pp. 980–1023. ISSN: 00796425.

[4] R. S. Mishra and Z. Y. Ma. "Friction stir welding and processing". In: *Materials Science and Engineering: R: Reports* 50.1 (2005), 1–78.

[5] Z. Y. Ma. "Friction stir processing technology: a review". In: *Metallurgical and Materials Transactions A* 39.3 (2008), 642–658.

[6] L. Karthikeyan et al. "Mechanical property and microstructural changes during friction stir processing of cast aluminum 2285 alloy". In: *Materials & Design* 30.6 (2009), 2237–2242.

[7] F.C. Liu et al. "Investigation of superplasticity in friction stir processed 2219Al alloy". In: *Materials Science and Engineering: A* 527.16-17 (June 2010), pp. 4191–4196. ISSN: 09215093.

[8] F.C. Liu and Z.Y. Ma. "Superplasticity governed by effective grain size and its distribution in fine-grained aluminum alloys". In: *Materials Science and Engineering: A* 530 (Dec. 2011), pp. 548–558. ISSN: 09215093.

[9] Patrick B. Berbon et al. "Friction stir processing: a tool to homogenize nanocomposite aluminum alloys". In: *Scripta Materialia* 44.1 (2001), 61–66.

[10] K. Nakata et al. "Improvement of mechanical properties of aluminum die casting alloy by multi-pass friction stir processing". In: *Materials Science and Engineering: A* 437.2 (2006), 274–280.

[11] S. Jana et al. “Effect of friction stir processing on fatigue behavior of an investment cast Al–7Si–0.6 Mg alloy”. In: *Acta Materialia* 58.3 (2010), 989–1003.

[12] F. Nascimento et al. “Microstructural modification and ductility enhancement of surfaces modified by FSP in aluminium alloys”. In: *Materials Science and Engineering: A* 506.1-2 (Apr. 2009), pp. 16–22. ISSN: 09215093.

[13] Z. Y. Ma, R. S. Mishra, and M. W. Mahoney. “Superplastic deformation behaviour of friction stir processed 7075Al alloy”. In: *Acta materialia* 50.17 (2002), 4419–4430.

[14] Q. Yang et al. “Achieving high strain rate superplasticity in Mg–Zn–Y–Zr alloy produced by friction stir processing”. In: *Scripta Materialia* 65.4 (2011), 335–338.

[15] Q. Yang et al. “Influence of texture on superplastic behavior of friction stir processed ZK60 magnesium alloy”. In: *Materials Science and Engineering: A* (2012).

[16] Datong Zhang et al. “Superplastic tensile behavior of a fine-grained AZ91 magnesium alloy prepared by friction stir processing”. In: *Materials Science and Engineering: A* 556 (Oct. 2012), pp. 100–106. ISSN: 09215093.

[17] W. B. Lee and S. B. Jung. “The joint properties of copper by friction stir welding”. In: *Materials Letters* 58.6 (2004), 1041–1046.

[18] A. Barcellona et al. “On microstructural phenomena occurring in friction stir welding of aluminium alloys”. In: *Journal of Materials Processing Technology* 177.1-3 (July 2006), pp. 340–343. ISSN: 09240136.

[19] S. Mironov, Y.S. Sato, and H. Kokawa. “Development of grain structure during friction stir welding of pure titanium”. In: *Acta Materialia* 57.15 (Sept. 2009), pp. 4519–4528. ISSN: 13596454.

[20] S. Mironov, Y.S. Sato, and H. Kokawa. “Microstructural evolution during friction stir welding of Ti–15V–3Cr–3Al–3Sn alloy”. In: *Materials Science and Engineering: A* 527.29-30 (Nov. 2010), pp. 7498–7504. ISSN: 09215093.

[21] Christian B. Fuller et al. “Evolution of microstructure and mechanical properties in naturally aged 7050 and 7075 Al friction stir welds”. In: *Materials Science and Engineering: A* 527.9 (Apr. 2010), pp. 2233–2240. ISSN: 09215093.

[22] Z. Y. Ma et al. “Microstructural refinement and property enhancement of cast light alloys via friction stir processing”. In: *Scripta Materialia* 58.5 (2008), 361–366.

[23] S. Mironov, Y. S. Sato, and H. Kokawa. “Microstructural evolution during friction stir-processing of pure iron”. In: *Acta Materialia* 56.11 (2008), 2602–2614.

[24] C Rhodes. “Fine-grain evolution in friction-stir processed 7050 aluminum”. In: *Scripta Materialia* 48.10 (May 2003), pp. 1451–1455. ISSN: 13596462.

[25] D. C. Hofmann and K. S. Vecchio. “Submerged friction stir processing (SFSP): An improved method for creating ultra-fine-grained bulk materials”. In: *Materials Science and Engineering: A* 402.1 (2005), 234–241.

[26] C. I. Chang, X. H. Du, and J. C. Huang. "Achieving ultrafine grain size in Mg–Al–Zn alloy by friction stir processing". In: *Scripta materialia* 57.3 (2007), 209–212.

[27] C Chang, X Du, and J Huang. "Producing nanograined microstructure in Mg–Al–Zn alloy by two-step friction stir processing". In: *Scripta Materialia* 59.3 (Aug. 2008), pp. 356–359. ISSN: 13596462.

[28] Hidetoshi Fujii et al. "Investigation of welding parameter dependent microstructure and mechanical properties in friction stir welded pure Ti joints". In: *Materials Science and Engineering: A* 527.15 (June 2010), pp. 3386–3391. ISSN: 09215093.

[29] Y. F. Sun and H. Fujii. "Investigation of the welding parameter dependent microstructure and mechanical properties of friction stir welded pure copper". In: *Materials Science and Engineering: A* 527.26 (2010), 6879–6886.

[30] Q. Yang et al. "Effect of tool geometry and process condition on static strength of a magnesium friction stir lap linear weld". In: *Materials Science and Engineering: A* 528.6 (Mar. 2011), pp. 2463–2478. ISSN: 09215093.

[31] I. Galvão et al. "Influence of tool shoulder geometry on properties of friction stir welds in thin copper sheets". In: *Journal of Materials Processing Technology* 213.2 (Feb. 2013), pp. 129–135. ISSN: 09240136.

[32] A. Tokta\cs and G. Tokta\cs. "Effect of Welding Parameters and Aging Process on the Mechanical Properties of Friction Stir-Welded 6063-T4 Al Alloy". In: *Journal of materials engineering and performance* 21.6 (2012), 936–945.

[33] P. Xue et al. "Achieving friction stir welded pure copper joints with nearly equal strength to the parent metal via additional rapid cooling". In: *Scripta Materialia* 64.11 (2011), 1051–1054.

[34] Yutaka S. Sato et al. "Microstructural evolution of 6063 aluminum during friction-stir welding". In: *Metallurgical and Materials Transactions A* 30.9 (1999), 2429–2437.

[35] Cécile Genevois et al. "On the coupling between precipitation and plastic deformation in relation with friction stir welding of AA2024 T3 aluminium alloy". In: *Materials Science and Engineering: A* 441.1-2 (Dec. 2006), pp. 39–48. ISSN: 09215093.

[36] Juan Chen et al. "Effect of grain size on the microstructure and mechanical properties of friction stir welded non-combustive magnesium alloys". In: *Materials Science and Engineering: A* 549 (July 2012), pp. 176–184. ISSN: 09215093.

[37] Xu-he Liu et al. "Microstructure and mechanical properties of Mg-Li alloy after TIG welding". In: *Transactions of Nonferrous Metals Society of China* 21.3 (Mar. 2011), pp. 477–481. ISSN: 10036326.

[38] Dongxia Yang et al. "Study on microstructure and mechanical properties of Al–Mg–Mn–Er alloy joints welded by TIG and laser beam". In: *Materials & Design* 40 (Sept. 2012), pp. 117–123. ISSN: 02613069.

[39] Zhen-bo He et al. "Comparison of FSW and TIG welded joints in Al-Mg-Mn-Sc-Zr alloy plates". In: *Transactions of Nonferrous Metals Society of China* 21.8 (Aug. 2011), pp. 1685–1691. ISSN: 10036326.

[40] *ASM Handbook: Materials Characterization*. 9th. Vol. 10. ASM International, 1986.

[41] R. A. Smith. "The potential for friction stir weld inspection using transient eddy currents". In: *Insight-Non-Destructive Testing and Condition Monitoring* 47.3 (2005), 133–143.

[42] T. G. Santos, P. Vila\cca, and R. M. Miranda. "Electrical conductivity field analysis for evaluation of FSW joints in AA6013 and AA7075 alloys". In: *Journal of Materials Processing Technology* 211.2 (2011), 174–180.

[43] T G Santos et al. "Microstructural mapping of friction stir welded AA 7075-T6 and AlMgSc alloys using electrical conductivity". In: *Science and Technology of Welding & Joining* 16.7 (Oct. 2011), pp. 630–635. ISSN: 13621718, 17432936.

[44] T. G. Santos et al. "Modification of electrical conductivity by friction stir processing of aluminum alloys". In: *The International Journal of Advanced Manufacturing Technology* 57.5 (2011), 511–519.

[45] *ASM Handbook: Nondestructive evaluation and quality control*. 9th. Vol. 17. ASM International, 1989.

[46] L. S. Rosado et al. "Advanced technique for non-destructive testing of friction stir welding of metals". In: *Measurement* 43.8 (2010), 1021–1030.

[47] David C. Jiles. *Introduction to the Principles of Materials Evaluation*. CRC Press. ISBN: 0-8493-7392-1.

[48] Luis S. Rosado et al. "Geometric optimization of a differential planar eddy currents probe for non-destructive testing". In: *Sensors and Actuators A: Physical* 197 (Aug. 2013), pp. 96–105. ISSN: 09244247.

[49] B. Raj, C. K. Mukhopadhyay, and T. Jayakumar. "Frontiers in NDE research nearing maturity for exploitation to ensure structural integrity of pressure retaining components". In: *International journal of pressure vessels and piping* 83.5 (2006), 322–335.

[50] J. Shao et al. "Automatic weld defect detection based on potential defect tracking in real-time radiographic image sequence". In: *NDT & E International* (2011).

[51] S. Sambath, P. Nagaraj, and N. Selvakumar. "Automatic defect classification in ultrasonic NDT using artificial intelligence". In: *Journal of Nondestructive Evaluation* 30.1 (2011), 20–28.

[52] U. Sreedhar et al. "Automatic defect identification using thermal image analysis for online weld quality monitoring". In: *Journal of Materials Processing Technology* (2012).

[53] Y. Sato et al. "Automated visualization of surface morphology of cracks by means of induced current potential drop technique". In: *NDT & E International* (2012).

[54] B. Shakibi et al. "Resolution enhancement of ultrasonic defect signals for crack sizing". In: *NDT & E International* 52 (Nov. 2012), pp. 37–50. ISSN: 09638695.

[55] Enkhsaikhan Boldsaikhan et al. "The use of neural network and discrete Fourier transform for real-time evaluation of friction stir welding". In: *Applied Soft Computing* 11.8 (Dec. 2011), pp. 4839–4846. ISSN: 15684946.

[56] A. Lopes Ribeiro et al. "Eddy current inspection of a duralumin plate". In: *Instrumentation and Measurement Technology Conference, 2009. I2MTC'09. IEEE*. 2009, 1367–1371.

[57] Giuseppe Sposito, Peter Cawley, and Peter B. Nagy. "Potential drop mapping for the monitoring of corrosion or erosion". In: *Ndt & E International* 43.5 (2010), 394–402.

[58] Giuseppe Sposito, Peter Cawley, and Peter B. Nagy. "An approximate model for three-dimensional alternating current potential drop analyses using a commercial finite element code". In: *NDT & E International* 43.2 (Mar. 2010), pp. 134–140. ISSN: 09638695.

[59] T. G. Santos. "Ensaios Não Destrutivos por Correntes Induzidas: Desenvolvimento e Aplicação à Soldadura por Fricção Linear". PhD thesis. 2009.

[60] L. S. Rosado et al. "A differential planar eddy currents probe: Fundamentals, modeling and experimental evaluation". In: *NDT & E International* (2012).

[61] S. Konoplyuk et al. "Characterization of ductile cast iron by eddy current method". In: *NDT & E International* 38.8 (Dec. 2005), pp. 623–626. ISSN: 09638695.

[62] Thanh Long Cung, Pierre Yves Joubert, and Eric Vourch. "Eddy current evaluation of air–gaps in aeronautical multilayered assemblies using a multi-frequency behavioral model". In: *Measurement* 44.6 (July 2011), pp. 1108–1116. ISSN: 02632241.

[63] V Zilberstein. "MWM eddy-current arrays for crack initiation and growth monitoring". In: *International Journal of Fatigue* 25.9-11 (Sept. 2003), pp. 1147–1155. ISSN: 01421123.

[64] K.V. Rajkumar et al. "Characterization of aging behaviour in M250 grade maraging steel using eddy current non-destructive methodology". In: *Materials Science and Engineering: A* 464.1-2 (Aug. 2007), pp. 233–240. ISSN: 09215093.

[65] D. Mercier et al. "Eddy currents and hardness testing for evaluation of steel decarburizing". In: *NDT & E International* 39.8 (Dec. 2006), pp. 652–660. ISSN: 09638695.

[66] B. Li, Y. Shen, and W. Hu. "The study on defects in aluminum 2219-T6 thick butt friction stir welds with the application of multiple non-destructive testing methods". In: *Materials & Design* 32.4 (2011), 2073–2084.

[67] Chuck Hellier. *Handbook of Nondestructive Evaluation*. en. McGraw Hill Professional, Mar. 2001. ISBN: 9780070281219.

[68] Nicola Bowler. "Theory of four-point alternating current potential drop measurements on a metal half-space". In: *Journal of Physics D: Applied Physics* 39.3 (Feb. 2006), pp. 584–589. ISSN: 0022-3727, 1361-6463.

[69] Nicola Bowler. "Theory of Four-Point Direct-Current Potential Drop Measurements on a Metal Plate". In: *Research in Nondestructive Evaluation* 17.1 (2006), pp. 29–48.

[70] Matweb. *AISI 1020 Steel, cold rolled*.

[71] Matweb. *304 Stainless Steel*.

[72] Matweb. *Titanium Ti-6Al-4V (Grade 5), Annealed*.

[73] Matweb. *Titanium Grade 2*.

[74] Matweb. *Magnesium AZ31B, Forgings*.

[75] Matweb. *Lead, Pb*.

[76] Matweb. *Copper, Cu; Annealed*.